Carbonate deposition in the Palaeoproterozoic Onega basin from Fennoscandia: a spotlight on the transition from the Lomagundi-Jatuli to Shunga events

Victor A. Melezhik[a], Anthony E. Fallick[b], Alexander T. Brasier[c], Aivo Lepland[a]

[a] Geological Survey of Norway, Postboks 6315 Slupen, NO-7491 Trondheim, Norway

[b] Scottish Universities Environmental Research Centre, Rankine Avenue, East Kilbride, Scotland. G75 0QF

[c] University of Aberdeen, Department of Geology and Petroleum Geology, Meston Building, University of Aberdeen, AB24 3UE, Scotland.

Corresponding author's contact information: phone - +47 73 90 40 00, email - victor.melezhik@ngu.no

Carbonate deposition in the Palaeoproterozoic Onega basin from Fennoscandia: a spotlight on the transition from the Lomagundi-Jatuli to Shunga events

Victor A. Melezhik[a], Anthony E. Fallick[b], Alexander T. Brasier[c], Aivo Lepland[a]

[a] Geological Survey of Norway, Postboks 6315 Slupen, NO-7491 Trondheim, Norway

[b] Scottish Universities Environmental Research Centre, Rankine Avenue, East Kilbride, Scotland. G75 0QF

[c] University of Aberdeen, Department of Geology and Petroleum Geology, Meston Building, University of Aberdeen, AB24 3UE, Scotland.

Abstract

Several deep drillholes were made in the Onega palaeobasin by the Fennoscandian Arctic Russia–Drilling Early Earth Project (FAR-DEEP) of the International Continental Scientific Drilling Program (ICDP). These provided fresh core material documenting the Lomagundi-Jatuli Isotopic Event (LJIE), its termination, and the start of the Shunga Event (SHE) of an enhanced accumulation of organic matter. The cored section represents the most complete known record of the end of the LJIE.

The late phase of the LJIE, recorded in FAR-DEEP Core 11A, is represented by the upper part of the Tulomozero Formation (TF), a 300-m-thick unit composed of variegated dolostones, siltstones and shales. Accumulated under oxic conditions on a shallow-water carbonate platform, the TF hosts the earliest known thick formations of halite and massive anhydrite. Low-temperature greenschist facies metamorphism caused partial recrystallisation of the rocks; however, a primary carbonate phase, the dolomite, exhibits a negligible degree of post-depositional alteration of the carbon isotope system. The dataset of 46 bulk-carbonate analyses of carbon and oxygen isotopes yielded $\delta^{13}C_{carb}$ ranging between +6.8 and +11.8‰, and revealed a positive excursion from +8 to +11.8‰ followed by a decline to +8‰ towards the top of the 300-m-thick succession.

The cored part of the overlying Zaonega Formation (ZF) recovered in holes 12AB and 13A is an 800-m-thick unit composed of mixed siliciclastic–carbonate facies with numerous mafic lava flows and tuff beds intruded by gabbro sills. The formation represents an unprecedented episode of enhanced accumulation of organic-rich rocks and preserves the earliest known supergiant, petrified oilfield, all typifying the SHE. The sedimentological, petrographic, geochemical and C- and O-isotopic study of over 800 m of core throughout the ZF suggests that the initial carbonate deposition occurred in a lacustrine environment, then rapidly proceeding through a lagoonal setting to a rifted deepwater shelf, and finally to a carbonate platform. Both the deepwater shelf and the platformal settings are marked by organic-rich environments. The primary dolomite was potentially exposed to syn- and post-depositional hydrothermal/metasomatic alterations, organic matter diagenesis, metamorphic mineral reactions, CO_2 degassing, and finally a low-temperature, post-metamorphic calcitisation resulting in overall large fluctuations of $\delta^{13}C_{carb}$ between -22 and +8‰. The dataset of over 413 bulk-carbonate analyses of carbon and oxygen isotopes, screened petrographically and geochemically against post-depositional alteration, revealed 28 least-altered samples within three stratigraphic intervals, suggesting multiple positive and negative $\delta^{13}C_{carb}$ excursions throughout over 1000 m of stratigraphy. A shift from +5 to +9‰ followed by a drop to near zero values marks the lower part of the ZF. A $\delta^{13}C_{carb}$ decline from +8‰ to below zero in the middle and upper part of the ZF defines the end of the LJIE. A subsequent prominent negative excursion down to -6‰ does not show convincing isotopic evidence for influence of methanogenesis, and hence appears to be of primary depositional origin. An erratic positive excursion in the uppermost part of the drilled section indicates return of $\delta^{13}C_{carb}$ to a near normal marine value.

Keywords: Palaeoproterozoic, dolomite, pyrobitumen, carbon isotopes, Fennoscandia

1. Introduction

The Onega palaeobasin located in southeastern Fennoscandia (Fig. 1) contains a Palaeoproterozoic sedimentary-volcanic succession which has been drilled by the recently completed FAR-DEEP ICDP project (http://far-deep.icdp-online.org). The succession has the world's most complete known geological record that covers the transition from the Lomagundi-Jatuli Isotopic Event (LJIE) to the Shunga Event (SHE) (Melezhik, 2012). The LJIE, recorded in the Tulomozero Formation (TF) represents an unprecedented perturbation of the global carbon cycle resulting in a positive excursion of $\delta^{13}C$ in sedimentary carbonates (e.g., Baker and Fallick, 1989a, b), whereas the SHE, recorded in the Zaonega Formation (ZF), is known for an intensive accumulation of organic matter and formation of the earliest known supergiant petroleum oil field (Mossman et al., 2005; Melezhik et al., 2009).

These two global-scale palaeoenvironmental events (Fig. 2) are among several revolutions associated with an advanced stage of the progressive oxidation of Earth's environments (reviewed in Melezhik et al., 2005a). This stage was an environmental drama that affected the entire biosphere (which comprises lithosphere, hydrosphere and atmosphere) on an unprecedented scale (reviewed in Kump et al., 2013). There is compelling evidence that the LJIE and SHE time interval represents a dynamic period in the history of the Earth (Kump et al., 2011; Planavsky et al., 2012; Asael et al., 2013; Canfield et al., 2013), yet many details of the global-scale geochemical cycles remain understudied. This is particularly the case for the carbon cycle, recently provoking a series of controversial and conflicting interpretations (e.g., Kump et al. (2011) and Canfield et al. (2013) versus Qu et al. (2012) and Farquhar et al. (2014)). In this contribution we address the upper part of the TF and the lower and middle parts of the ZF whose deposition represents the time window for the transition from the LJIE to the SHE (Fig. 3), and whose carbonate rocks recorded invaluable information for deciphering the operation of global cycling of carbon.

Brasier et al. (2011) published detailed petrographic and geochemical characteristics of the ZF carbonate rocks in FAR-DEEP Core 10B, and reported $\delta^{13}C_{carb}$ values ranging in the middle part of the TF from +7.7 to +15.7‰. Črne et al. (2014) recently published a rather comprehensive account of the petrographic and geochemical characteristics of the ZF carbonate rocks in FAR-DEEP Core 12AB and reported a pervasive calcitisation of primary dolomite, associated with overprinting of depositional C-isotopic values.

The main goals of this article are: (i) to provide a review of already published as well as a discussion of new FAR-DEEP material on the carbonate carbon isotopic excursion through the transition from the LJIE to the SHE; (ii) to employ a large database for screening against post-depositional alteration of $\delta^{13}C_{carb}$; (iii) to consider the deposition of the ZF carbonates in the context of basin evolution; (iv) and finally to provide a better understanding of the global carbon cycle through one of the most intriguing episodes of Earth's evolution in Deep Time.

2. Material studied

The FAR-DEEP project cored 15 drillholes and provided 3650 m of core material from the eastern Fennoscandian Shield (Melezhik, 2012). This includes 6 drillholes that intersected 1900 m of sedimentary-volcanic succession which records the LJIE and SHE in a single basin, the Onega palaeobasin (Fig. 1). The current research is based on sedimentological, petrographic and geochemical studies of carefully logged FAR-DEEP Cores 11A, 12A, 12B and 13A.

Hole 11A (436 m) drilled in the northern part of the Onega palaeobasin intersected the middle and upper part of the TF and the base of the ZF (Figs 1 and 3A). Holes 12A (99.57 m) and 12B (411.46 m) sampled overlapping sections of the volcano-sedimentary succession of the ZF. Hole 13A (240 m) was drilled 25 km north-west of 12A and 12B (hereafter 12AB), and intersected the ZF section which partially overlaps with that intersected by Holes 12AB (Figs 1 and 3A). The base of the uppermost dolostone unit in Cores 13A (76.6 m) and 12AB (9.3 m, Fig. 10) was used as the lithostratigraphic marker boundary (Črne et al., 2013a, b; 2014). In addition, a lithological interval with several thin beds containing specific black and pale brown clay balls (Fig. 4) was suggested as another marker unit for the correlation of Cores 13A (183–159 m) and 12AB (180–160 m).

Comprehensive core description and photodocumentation is combined with 896 XRF analyses of major elements, 627 ICP-AES analyses of trace elements, and 413 bulk-carbonate analyses of carbon and oxygen stable isotopes (Appendices A–C).

3. Analytical methods

Fifteen grams of rock powder were used to analyse major and trace elements at the Geological Survey of Norway (NGU) by X-ray fluorescence spectrometry using a PANalytical Axios at 4 kW. Elemental concentrations in whole-rock samples were determined on acidified extracts (cold 10% HCl) by inductively coupled plasma-atomic emission spectrometry (ICP-AES) using a Thermo Jarell Ash ICP 61. Total organic carbon (TOC), and total carbon (TC) were determined at NGU and at the University of Münster. At NGU sealed tube combustion using a Leco SC-444 had a total analytical uncertainty of 15%. For measurements of TOC, the samples were reacted with 10% HCl before the combustion and inorganic carbon (IC) was calculated as the difference between TOC and TC. At the University of Münster the IC was determined by reaction with 10% HCl acid and TC by combustion of the sample; TOC was calculated from TC and IC. Stable carbon and oxygen isotope analyses were performed at the Scottish Universities Environmental Research Centre (SUERC). Approximately 1 mg powder was reacted overnight with phosphoric acid at 70˚C. Isotopic ratios were measured on PRISM II or AP2003 mass spectrometers. Repeat analyses of NBS-18 and internal calcite standards are generally better than ±0.2‰ for carbon and ±0.3‰ for oxygen. Carbon and oxygen isotopic values are reported and discussed in the conventional delta notation relative to V-PDB and V-SMOW, respectively.

4. The Onega palaeobasin

The Onega palaeobasin represents a fragment of continental margin preserved on the Archaean Karelian craton in the eastern part of the Fennoscandian Shield. The basin accommodated over 5000 m of sedimentary and volcanic rocks over the c. 2440–1890 Ma time interval (Fig. 3), which is radiometrically poorly constrained (reviewed in Glushanin et al., 2011; Melezhik et al., 2012b). Basin filling was interrupted by numerous non-depositional breaks and several episodes of erosion of unknown duration.

Initial deposition in the Onega palaeobasin was associated with an incipient rifting which began in northeastern Fennoscandia prior to 2505 Ma (e.g., Melezhik and Hanski, 2012). The rifting became widespread following the emplacement of plume-related, layered gabbro-norite intrusions and dyke swarms at 2505-2440 Ma (Hanski and Melezhik, 2012), leading to the establishment of an active continental margin. The mantle-plume-driven continental uplifts led to the emplacement of voluminous continental flood basalts, which at c. 2440 Ma were uplifted, dissected by repeated rifting and affected by erosion and deep weathering within the entire shield area, then followed by the onset of the global-scale Huronian-age glaciation (Marmo and Ojakangas, 1984; Melezhik, 2006; Melezhik et al., 2013c).

No or very little igneous activity is documented between 2400 and 2200 Ma in the Fennoscandian Shield (reviewed in Hanski and Melezhik, 2012) reflecting world-wide magmatic slowdown (Condie et al., 2009). The advanced rifting at c. 2200-2060 Ma was followed by formation of a vast epeiric sea and large shallow-water carbonate platforms (Melezhik and Hanski, 2012). This period was marked by subaerial eruptions of highly-oxidised lavas (Hanski, 2012), deposition of chemically-mature sandstones, and ^{13}C-rich dolostones representing the LJIE. Red beds became abundant in both subaerial and subaqueous conditions, and the earliest-known thick halite and massive anhydrite formations were recorded (Morozov et al., 2010).

At approximately 2100 Ma, the late Archaean craton was eventually affected by advanced separation and formation of the Kola Ocean and Svecofennian Sea (e.g., Daly et al., 2006). During this tectonic development the Onega palaeobasin formed a rifted active continental margin bordering the Svecofennian Sea (Lahtinen et al., 2008). This was the time when the volcano-sedimentary succession of the ZF was deposited, followed by voluminous subaqueous mafic magmatism. This was accompanied by an unprecedented accumulation of C_{org}-rich rocks and formation of the earliest known petrified giant oilfield (Melezhik et al., 2009; Melezhik et al., 2012b) representing the worldwide SHE (e.g., Melezhik et al., 2005a).

The overlying clastic sediments were deposited in lacustrine and shallow-water shelf environments after a non-depositional break and erosion episode of unknown duration. The lacustrine greywacke-shale succession records an event of surface oil seeps derived from tectonically compromised ZF oil reservoirs (Melezhik et al., 2009).

Between 1890 and 1790 Ma, the early Palaeoproterozoic volcano-sedimentary succession underwent deformation and greenschist-facies metamorphism of the Svecofennian orogeny. The rocks were deformed into a system of roughly parallel, northwest-southeast trending folds that overall form a synclinorium (Kharitonov, 1966).

The Onega palaeobasin hosts six V-U-Mo-precious-rare metal deposits and numerous shows (Fig. 1B). Their position has both lithological and structural control. The deposits are situated along contacts between ZF black shales and underlying red beds, and located within northwest-southeast trending antiforms affected by vertical faults (e.g., Golubev and Novikov, 2005). Ore processes are associated with a three-phase, low-temperature metasomatic alteration, not linked to any igneous activity, and dated to 1760 ± 60 Ma (U-Pb, Golubev and Novikov, 2005), hence postdating the Svecofennian metamorphism and deformation.

5. The Tulomozero Formation

5.1. Depositional age and lithostratigraphy

Since the work of Galimov et al. (1968) and Schidlowski et al. (1975), the TF has been central to a number of studies investigating the global carbon cycle during the Palaeoproterozoic (Yudovich et al., 1991; Akhmedov et al., 1993; Karhu, 1993; Tikhomirova and Makarikhin, 1993; Melezhik and Fallick, 1996; Heiskanen and Rychanchik, 1999; Melezhik et al., 1999a, 2005b; Brasier et al., 2011). Despite the intensive sedimentological and C-, O- and Sr-isotopic studies, the precise depositional time of the TF remains poorly constrained (Fig. 3). The only currently published age is 2090 ± 70 Ma obtained by a Pb-Pb technique on dolomite (Ovchinnikova et al., 2007).

In the Onega palaeobasin the TF is composed of diverse evaporite-carbonate-siliciclastic lithofacies showing frequent vertical (e.g., Fig. 5) as well as lateral variations (Melezhik et al., 2012b). In the south-western part of the Onega palaeobasin, the TF succession starts with a c. 194-m-thick halite bed apparently accumulated within a lagoonal setting developed directly on an Archaean granite basement (Morozov et al., 2010). The halite is brown, pink and grey in colour and contains minor sylvinite and numerous clasts of magnesite (Fig. 6).

In the southeast, the correlative section is composed of red sandstone-dolarenite-mudstone cycles deposited in a braided fluvial system passing into a peritidal coastal plain (Melezhik et al., 2000), whereas in the north, it comprises fining-upward dolarenite-siltstone cycles accreted on the slope of a carbonate platform (Melezhik et al., 2013a).

In the southwest, the above rock succession is followed by a c. 290-m-thick unit of nodular shales interbedded with thick and massive anhydrite-magnesite beds (Fig. 7; Krupenik et al., 2011a), all accumulated in a sabkha environment. Elsewhere in the basin, the time-equivalent succession comprises lithofacies associated with the growth of a shallowmarine carbonate platform. This includes supratidal-intertidal and carbonate-clastic-evaporite cycles, sabkha mudstones, slope dolarenites and reefal stromatolitic dolostones. Several episodes of repeated carbonate-evaporite cycles, sabkha and playa evaporites, dissolution-collapse breccias, surface and subaqueous karstification events record frequent fluctuations in sea level, numerous phases of exposure in oxic environments, and overall accumulation in a shallow-water epeiric sea (Melezhik et al., 2013a).

All terrestrial and marine sedimentary rocks and halite beds are predominantly red, brown, pink or variegated in colour (Figs 3B, C, D and 6) implying oxygen availability in depositional systems. Epigenetic bleaching and discolouration advancing through joints and porous beds is widespread and results in the formation of hundreds of meters of clastic and carbonate rocks with patchy appearance.

The bulk lithology of the TF as documented in Core 11A is as diverse as in many other studied sections (e.g., Melezhik et al., 2012b). Carbonate rocks are the dominant lithology and include massive, bedded, crystalline and stromatolitic dolostones, dolarenites, dolorudites, dolomarls, *in situ* and redeposited dissolution breccias. Shale, siltstone and sandstone have been documented among non-carbonate rocks (Melezhik et al., 2013a). Soft-sediment deformation, dissolution cavities and microkarst are abundant throughout the drilled section. A thick, basin-wide, mafic lava flow occurs in the middle part of the drilled section. Figure 8 provides photodocumentation of the main rocks types exemplifying the major lithofacies and their sedimentological features. The TF intersected by Core 11A has been subdivided into seven distinct lithological units (Fig. 5). These are, starting from the base: member 1 (Dolostone-Siltstone-Shale); member 2 (Sandstone-Siltstone-Shale-Dissolution Breccia); member 3 (Lower Dolostone); member 4 (Siltstone-Shale-Basalt); member 5 (Dolostone-Dissolution Breccia); member 6 (Conglomerate); and member 7 (Upper Dolostone) (Melezhik et al., 2013a).

5.2. Sedimentological features of carbonate rocks

The carbonate rocks of the TF cored by FAR-DEEP Hole 11A recorded invaluable information on the Proterozoic global carbon cycle towards the termination of the LJIE. Petrography, geochemistry and sedimentological characteristics of the TF as a whole, and of the carbonate lithofacies in particular, have been comprehensively studied (e.g., Melezhik et al., 1999a; 2000, 2001; Brasier et al., 2011; Reuschel et al., 2012). A detailed lithological description of Core 11A can be found in Melezhik et al. (2013a). Hence, below we provide only petrographic and geochemical information that is essential for deciphering the depositional trend of $\delta^{13}C_{carb}$.

In Core 11A the carbonate rocks occur throughout stratigraphy, comprising either thick discrete units (member 7; Fig. 5) or intercalations with minor beds of sandstones, shales and conglomerates in members 1, 3 and 5. In other intervals (member 2 and 4) they occur as thin beds in sandstone-siltstone-shale successions.

In the lower part of the drilled succession, which includes members 1 and 2 at 436–374 m, the carbonate rocks comprise 0.2- to 2.5-m-thick dolostone-dolomarl/shale cycles, and more rarely dolostone-evaporite cycles, accumulated in a peritidal carbonate flat setting (Melezhik et al., 2013a). All rocks have variegated colour and irregular bedding (Fig. 8A, B). *In situ* brecciation and soft-sediment deformation, due to post-depositional growth of sulphates as well as dissolution of evaporitic minerals, are common.

In the overlying succession (member 3 at 374–327.4 m) carbonate rocks are the dominant lithology. These are mainly thick beds of light-coloured and variegated dolarenite and dolorudite with massive, crude bedding, irregular lamination and *in situ* brecciation (Fig. 8C, D). Thinner sandstone-siltstone-shale-marl interbeds exhibit lensoidal (sand ripples), lenticular and flaser bedding. The succession is marked by numerous thick dolostone-dolomarl/shale shallowing-up cycles with limited evidence for subaerial exposure, and is interpreted as representing deposition along the lower part of intertidal flats (Melezhik et al., 2013a).

The following member 4 (327.4–282 m) contains only one thin dolorenite interval embedded in intertidal siltstone-shale lithofacies with a variegated colour, lensoidal and wavy lamination which was partially modified by dissolution and cementation, and growth of pseudomorphs after Ca-sulphates. The sedimentation was interrupted by the emplacement of a c. 20-m-thick body of mafic lava with a large areal extent (e.g., Satzuk et al., 1988; Krupenik et al., 2011a). In Core 11A the upper contact of the flow shows signs of subaerial or submarine weathering and erosion and incorporation of the weathered material into the overlying shales (Melezhik et al., 2013a).

Member 5 (282–203 m) is dominated by carbonate rocks and dissolution-collapse breccias. Most of the carbonate rocks are redeposited and composed of poorly-sorted and angular intraformational clasts with abundant rip-ups of black, haematite-rich mudstone (Fig. 8E). Throughout the section, rocks contain abundant mm-sized quartz-pseudomorphed sulphate nodules, discoidal and twinned crystals after gypsum, and dolomite-replaced halite-bearing beds. Rare dolomarl beds show dissolution surfaces and enterolithic structures of former anhydrite beds (Fig. 8F). Large solution holes filled with debris of collapsed overlying beds are abundant. The overall member 5 succession is defined by numerous 0.5- to 10-m-thick dolostone-breccia cycles interpreted as a stack of shallowing-up carbonate-evaporite cycles deposited in a sabkha environment (Melezhik et al., 2013a).

The overlying member 6 (203–179 m) includes only one thin interval of carbonate rock, and is composed mainly of polymict clast-supported carbonate conglomerates with a talc-rich matrix (Fig. 8G) resembling terra rossa soil (Fig. 8H). These lithofacies have not been documented previously in the TF and represent a unique, local occurrence. The conglomerates show neither bedding nor stratification and bear no signs of reworking by currents or wave action, yet the rounded morphology of clasts suggests either weathering or freshwater dissolution and physical reworking. Melezhik et al. (2013a) have interpreted these rocks as partially-reworked karstic collapse breccias originated after dissolution of evaporites.

The uppermost part of the TF (Member 7, 179–106.3 m) is represented in Core 11A by three different lithofacies, all chiefly composed of carbonate rocks (Fig. 5). The lower lithofacies (179–c. 160 m) is the only one in Core 11A containing oncolithic/oolitic dolostones (Fig. 8I) accumulated in a subtidal–intertidal flat setting (Melezhik et al., 2013a). The other lithology in this interval is a c. 1-m-thick slumped shale-dolomarl (Fig. 8J) capped by dissolution-collapse breccia.

The following succession (160–120 m) is composed of a buff, parallel-laminated, microcrystalline, relatively pure dolostone (Fig. 8K) with layers of brown, laminated dolomarl. The lowermost 20-m-thick interval is typified by abundant solution-enlarged cracks and large cavities filled with red, clay-rich, intraformational breccia resembling terra rossa (Fig. 8L). The observed sedimentological features have been interpreted as karst *per se* or perhaps karren (e.g., Bogli, 1980) developed on a carbonate platform (Melezhik et al., 2013a). The karstified interval is followed by massive to laminated pure dolostones, overlain by two deepening-upward cycles of flat-laminated and columnar stromatolites (Fig. 8M), apparently forming a large biostrome or bioherm formed on a carbonate platform under subtidal conditions.

5.3. Petrographic and geochemical characteristics of carbonate rocks

The carbonate rocks studied in Core 11A were variably recrystallised under low-temperature greenschist facies conditions identified by the incipient reaction of dolomite and quartz forming talc. The recrystallisation processes partially obliterated primary depositional textures and structures, but all the rocks retain readily identifiable bedding and lamination (Fig. 8). Micritic dolomite is rarely preserved and most of the carbonate microfabrics are defined by granular, crystalline and micro-sparitic dolomite. Late carbonate phases, which fill voids, veins and cement breccias, are sparitic dolomite.

The carbonate rocks are predominantly impure with the major non-carbonate phase being silica. The abundance of SiO_2 ranges from <0.5 to over 40 wt.%, whereas the content of Al_2O_3 is commonly below 2 wt.% (Appendix A; Fig. 5A, B). The silica is either chemically precipitated quartz, formed as the result of post-depositional silicification, or clastic quartz grains. The abundance of SiO_2 is lowest in member 7 where the content of total inorganic carbon is the highest of all, approaching 12 wt.% (Fig. 5C). Most of the carbonate rocks are devoid of, or low in, Na_2O and K_2O (Fig. 5D, E). The organic carbon (TOC) content in all rocks is below the detection limit of 0.1 wt.%.

All carbonate samples studied in Core 11A, with two exceptions, are dolomitic in composition (Fig. 5F) with Mg/Ca_{carb} ratios ranging between 0.60 and 0.66 (Appendix A) and averaging at 0.64 (n = 42), hence close to the ratio of stoichiometric dolomite (0.62). Corresponding MgO/CaO_{wr} (whole-rock) ratios fluctuate between 0.77 and 3.15, averaging at 0.83 (Fig. 5G), thus higher than the ratio of stoichiometric dolomite (0.71). Both Mg/Ca_{carb} and MgO/CaO_{wr} ratios suggest intensive calcitisation of one sample at depth 246.36 m, and the presence of a variable amount of magnesite at depths 411.33, 202.93 and 195.95 m. All other intervals, which have MgO/CaO_{wr} >0.71 combined with $Mg/Ca_{carb} \approx 0.62$, contain talc (Fig. 5F, G).

The abundance of Sr_{carb} in the dolostones shows a large range (11–252 $\mu g \cdot g^{-1}$) with the lowest values in intensely silicified dolostones (e.g., SiO_2 = 76 wt.%, Sr = 11 $\mu g \cdot g^{-1}$, depth 336.7 m, Fig. 5H). The calcitised dolostone has Sr_{carb} = 130 $\mu g \cdot g^{-1}$, whereas Sr content in the magnesite-bearing intervals ranges between 42 and 65 $\mu g \cdot g^{-1}$. The abundance of Mn_{carb} varies greatly (46–1700 $\mu g \cdot g^{-1}$), with the highest values associated with thin dolostone intervals located close to siliciclastic beds or hosted by siltstone-shale units (e.g., 1700 $\mu g \cdot g^{-1}$ at depth 283.3 m, Fig. 5I). The calcitised dolostone has Mn_{carb} = 220 $\mu g \cdot g^{-1}$. The magnesite-bearing intervals show a relatively low Mn content (22–104 $\mu g \cdot g^{-1}$).

The stratigraphic distribution and large range of the Fe_{carb} abundances (20–3610 $\mu g \cdot g^{-1}$) somewhat mimic those of Mn_{carb} (Fig. 5J). Similarly, the highest values commonly mark dolostone intervals located close to siliciclastic rock, or thin beds hosted by siltstone-shale units. Carbonate phases from member 6 also show elevated content of Mn_{carb} (160–560 $\mu g \cdot g^{-1}$). In addition, there is a well-pronounced enrichment from 100 to 3610 $\mu g \cdot g^{-1}$ in the uppermost part of the section, towards the contact with the ZF within the 123–106.6 m interval (Fig. 5J).

The dolostones studied in Core 11A are characterised by low Mn/Sr_{carb} ratios, averaging at 2.9 ± 2 and ranging between 0.63 and 7.6 (n = 37). The exceptions with elevated ratios are: (*i*) thin intervals of dolostone sandwiched in siltstone-shale units (12. 5 and 33 m; see Fig. 5K); (*ii*) dolostones located in close proximity to contacts with the mafic lava (12.3 m); (*iii*) some carbonate intervals associated with member 6 conglomerates (17.0 m) and dissolution-collapse breccias (12.3 m).

All drilled and studied carbonate rocks in Core 11A show a significant enrichment in ^{13}C relative to VPDB. Carbon isotopic values vary between 5.8 and 11.8‰, thus ranging over 6‰ (Fig. 5L). $\delta^{18}O_{carb}$ values are relatively low (+18.6 ± 0.7 VSMOW, n = 46) and show a large fluctuation (+11.4 to +19.9‰, Fig. 5M).

5.4. Screening for post-depositional alteration of the carbon-isotopic composition of the TF carbonates

Several studies have specifically targeted the issue of post-depositional alteration of the TF $\delta^{13}C_{carb}$, and these have demonstrated that diagenetic and greenschist-grade metamorphic processes resulted in only insignificant modification of depositional $\delta^{13}C$ values (Melezhik et al., 1999a, 2000, 2001). In general, there is no evidence that dolomite precipitation, calcitisation of calcium sulphates and originally high $\delta^{13}C$ values were influenced by bacterial sulphate reduction or methane generation (Brasier et al., 2011). However, the oxygen isotope system might have experienced a significant depletion in ^{18}O with respect to marine carbonates. This was associated with diagenetic recrystallisation and metamorphic mineral reactions.

The dolomite + quartz + sericite ± calcite ± talc metamorphic mineral paragenesis can be observed in Core 11A, likely indicating that the dolomite reacted with silicates to produce calcite and talc (Winkler, 1979) with CO_2 enriched in ^{13}C:

$$6[Ca, Mg(CO_3)_2] + 8SiO_2 + 2H_2O \rightarrow Mg_6[Si_8O_{20}](OH)_4 + 6CaCO_3 + 6CO_2 \quad (1)$$

Discrimination diagrams presented in Fig. 9 compare/contrast Core 11A data with several previously reported datasets. These include other FAR-DEEP cores (e.g., 10A, 10B) as well as those obtained previously (7, 9, 4699 and 5177) in different parts of the Onega palaeobasin (Fig. 1B). The Core 11A dataset, similar to those of other cores, suggests that throughout the formation $\delta^{13}C_{carb}$ does not correlate with SiO_2 content, $\delta^{18}O_{carb}$, Mn/Sr or Mg/Ca (Fig. 9). Moreover, various lithofacies ranging from impure and pure dolostones to limestones and even magnesites share rather similar $\delta^{13}C$ values (Fig. 9A, D). All this is indicative of a high preservation of depositional $\delta^{13}C_{carb}$.

Diagenetic, metamorphic and hydrothermal alterations affect carbonate material in similar ways (e.g., Nabelek, 1991). These processes usually lower depositional $\delta^{13}C$ and $\delta^{18}O$ values, introduce Mn and remove Sr. In general, during post-depositional open system recrystallisation, the $\delta^{13}C$ of calcite and dolomite would be buffered by the dissolving precursor, while the $\delta^{18}O$, Mn and Sr contents would be partially shifted towards equilibrium with the ambient diagenetic fluids. Consequently, the common geochemical assessment of post-depositional alteration of marine carbonates is largely based on the relative abundances of Mn and Sr (e.g., Brand and Veizer, 1980). The Mn/Sr_{carb} ratio is used routinely and commonly as the parameter for discrimination between altered (Mn/Sr_{carb} >10) and least altered (Mn/Sr_{carb} <10) dolostones in Precambrian time (e.g., Kaufman and Knoll, 1995).

All except 5 samples have Mn/Sr_{carb} <10, compatible with a negligible involvement of freshwater fluids during carbonate recrystallisation. However, if samples having Mn/Sr_{carb} >10 or even Mn/Sr_{carb} >5 are excluded, the general stratigraphic $\delta^{13}C_{carb}$ trend remains largely unchanged (Fig. 5L). Moreover, samples with Mn/Sr_{carb} >5 or >10 are characterised by similar or even higher $\delta^{13}C_{carb}$ and $\delta^{18}O_{carb}$ than others in the succession. Consequently, all measured $\delta^{13}C_{carb}$ in Core 11A are accepted as relatively unaltered and hence representing a robust proxy for the carbon isotopic composition of seawater towards the end of the LJIE.

5.5. The $\delta^{13}C_{carb}$ temporal trend through the TF

The Core 11A dataset representing the middle and upper parts of the TF shows high $\delta^{13}C_{carb}$ values in its lowermost part (up to +10.4‰), followed by a sharp decline to +8‰ over c. 30

m, then by an erratic increase to +12‰ within a c. 130-m-thick succession, and finally by a continuous drop to +7.5‰ in the uppermost 110 m (Fig. 5L). Such a stratigraphic trend recorded in Core 11A through the middle and upper parts of the TF corroborates the fluctuations of $\delta^{13}C_{carb}$ reported previously from the composite section of the TF, including a pronounced drop towards the upper contact with the ZF (e.g., Melezhik et al., 2013a).

6. The Zaonega Formation

6.1. Depositional age, lithostratigraphy, igneous activity, and oil generation

A maximum age for the ZF has been imprecisely constrained at 2090 ± 70 Ma by a Pb-Pb technique on dolomite of the underlying TF (Ovchinnikova et al., 2007). Hannah et al. (2008) reported a preliminary Re–Os age of c. 2050 Ma obtained on organic matter from the upper part of the ZF. A minimum age for the ZF of c. 1980 Ma has been constrained by several whole-rock and mineral Sm–Nd and Pb–Pb isochrons on the Konchozero mafic-ultramafic unit which was emplaced in the upper part of the ZF but is considered to be co-magmatic with the overlying volcanic formation (Puchtel et al., 1992; Puchtel et al., 1998).

The ZF has the greatest areal distribution of all formations in the Onega palaeobasin (Fig. 1B). Its lower contact was documented in various places followed by controversial interpretations (e.g., Negrutsa, 1984; Galdobina, 1987). Based on FAR-DEEP data the basal contact of the ZF is sharp and defined by an angular unconformity between underlying, steeply-dipping, stromatolitic dolostones and flat-lying ZF variegated, parallel-laminated and cross-bedded sandstones. The above-described contact relationship may imply a period of uplift and erosion that preceded the deposition of the ZF (Melezhik et al., 2013a).

The ZF sampled in Core 12AB has been subdivided by Črne et al. (2013a, b; 2014) into several informal lithostratigraphic units (members). These are from the bottom upwards: the Greywacke member (498–250m) which includes the significant basin-wide gabbroic Magmatic Unit B (484–414 m), the Dolostone-Greywacke member (250–179.7m), the Mudstone-Limestone member (179.7–9.3 m) and the topmost Dolostone-Chert member. In this contribution, a parallel subdivision is suggested by recognising an additional unit termed the Lowermost Dolostone (LMD, 258–233 m, Fig. 10).

The bulk lithology of the ZF as documented in Core 12AB (99.57 and 411.46 m) and 13A (240 m) is represented by organic-matter-rich, greywacke-siltstone-shale rhythmites (Fig. 11A, B) deposited from turbidity currents (Črne et al., 2013 a, b). The turbiditic clastic sedimentation was accompanied by voluminous, tholeiitic, mafic, extrusive and intrusive magmatism with crustal geochemical signatures (Puchtel et al., 1998). Soft-sediment deformation, slumped beds, sedimentary/diagenetic boudinage, sedimentary dykes, intraformational conglomerates, and explosion-expulsion breccias (Fig. 11C–E) are common general features of the ZF (Melezhik et al., 2012b; Črne et al., 2013a, b). Disseminated pyrite, diagenetic pyrite concretions, and later metamorphic pyrrhotite are abundant throughout the formation. Chert and calcite nodules are also present (Fig. 11F–H). The abundance of carbonate nodules and concretionary beds cannot be reliably established because they are not always distinguishable in core from thin sedimentary carbonate beds (Črne et al., 2014).

Carbonate rocks occurring in the basal part of the ZF were studied in the top 106 m of Core 11A. Here, they appear as thin beds within a succession composed of several dm- to m-scale, fining-upward sandstone-siltstone/dolomarl cycles that pass up-section into clayey siltstones with minor dolostone and dolomarl. The rocks show parallel and small- to large-scale cross-bedding, rhythmic bedding and graded bedding (Melezhik et al., 2013). The 3500-m-deep Onega Parametric Hole drilled in the central part of the Onega basin (Fig. 1) suggests that the carbonate rocks are rare in the lower part of the section (Krupenik et al., 2011a). They become abundant starting from 406 m in Core 12AB.

The stratigraphic distribution of total inorganic carbon (TIC) content in all rocks from Cores 12AB and 13A suggests that carbonate is a common component of the middle and upper parts of the ZF (Fig. 10A). However, its highly variable content reflects the great abundance of mixed carbonate-siliciclastic lithologies. Nevertheless, in several intervals TIC content exceeds 10 wt.% and indicates the presence of relatively pure carbonate rocks. Thickness and abundance of carbonate beds with TIC >10 wt.% increase significantly in the uppermost part of the drilled section (Fig. 10B). In the lower part of Core 12AB, there are few carbonate beds and they are only several centimetres to several decimetres thick. The carbonate rocks are either layered or massive (Fig. 12A, B) and form parts of carbonate/marl-mudstone cycles which, in turn, are associated with thicker units of greywacke-siltstone-shale rhythmites (Črne et al., 2014). In contrast, in the middle part of Core 12AB carbonate beds form thicker units which may be composed of several mudstone-draped beds (Fig. 12C). In the uppermost part of the formation, carbonate rocks are most abundant and up to 4.5 m thick (Črne et al., 2013 a, b). They are massive and indistinctly bedded (Fig. 12D–F). In Core 13A carbonate rocks are syn-depositionally brecciated. The uppermost dolostones in both Core 12AB and Core 13A contain several spherule beds of possible impact origin (Huber et al., 2014).

Igneous rocks constitute 30–35% of the length of the drilled succession (Fig. 10) and are represented by pillowed and amygdaloidal-textured mafic lava flows and gabbro sills. The gabbro sill occurring in the lower part of the formation is over 50 m thick, was intersected by several drillholes across the Onega palaeobasin and appears to be a prominent basin-scale intrusion. Hornfels rocks are absent at contacts of magmatic rocks; instead, both sills and lavas have interacted with water-bearing, unconsolidated sediments forming peperites (Biske et al., 2004; Poleshchuk, 2011) and associated explosion-expulsion breccias (Fig. 11E, I; Melezhik et al., 2013b).

Voluminous mafic magmatism punctuating sedimentation in a rift setting has been considered to provide enhanced heat flow, the high thermal gradient resulting in the establishment of a shallow-depth oil window (Melezhik et al., 2013b). Evidence of liquid hydrocarbon generation and migration is plentiful throughout the ZF. Former oil migration pathways appear as varied-scale pyrobitumen-filled veinlets and veins cutting different lithologies. The most voluminous fossil oil trap in the drilled sections is located within brecciated dolostones and cherts in the upper part of Core 13A (Fig. 10). No information exists on the scale of oil traps in the Onega palaeobasin prior to Svecofennian deformation and metamorphism. However, many examples demonstrate that some or all Zaonega oil reservoir seals were breached several times and oil was spilled both onto the seafloor and subaerially (Melezhik et al., 2004, 2013b; Qu et al., 2012).

6.2. Petrography and geochemistry of carbonate rocks

The carbonate rocks of the ZF archive invaluable information on the Proterozoic global carbon cycle in general (e.g., Kump et al., 2011) and on the termination of the Lomagundi-Jatuli isotopic event in particular. However, the rocks experienced a set of multiple and complex post-depositional alterations (e.g., Črne et al., 2014, Fallick et al., submitted) that make deciphering of primary signatures a challenging task. Hence, below we present and discuss major petrographic, sedimentological and geochemical features of the ZF carbonate rocks and aim at providing some additional insights into their primary nature and post-depositional history.

Carbonates occurring in the lowermost part of the ZF and studied in Core 11A represent a succession of thinly-bedded, variegated rocks locally termed krivoserite (e.g., Melezhik et al., 2012b). The carbonate rocks are impure, variably calcitised dolostones and dolomarls (Melezhik et al., 2013a). In the middle and upper parts of the section represented by Cores 12AB and 13A, four main carbonate phases were recognised (Črne et al., 2014): *i*) Fe-Mn-poor dolomite; *ii*) Fe-Mn-rich dolomite; *iii*) calcite relatively rich in Sr; and iv) Sr-poor calcite. Both types of dolomite were suggested to represent the early, most likely primary, sedimentary carbonate phase whereas the calcite was considered as a later phase formed during progressive burial and metamorphism accompanied by metamorphic carbonate-silicate reactions and possibly by hydrothermal alteration (Črne et al., 2014).

Mg/Ca_{carb} ratios measured in the ZF carbonates (Fig. 10D) range from calcite to almost stoichiometric dolomite (0.62). The first appearance of high Mg/Ca_{carb} (dolomitic) rocks is associated with a carbonate-shale bed at 258–233 m in Core 12AB. Therefore, in the following discussion this bed is termed the Lowermost Dolostone (LMD, Fig. 10). Most of the low Mg/Ca_{carb} rocks are documented in the interval located below the LMD, whereas high Mg/Ca_{carb} rocks (dolomitic) occur within the LMD and above it (Fig. 10D).

6.2.1. Core 11A, carbonate rocks at the base of the ZF

The top 106 m of Core 11A represents the krivoserite succession composed of a thick interval of red and variegated sandstone-siltstones with several 0.5–10 cm thick beds of carbonate rocks. These are considered the lowermost carbonate rocks of the ZF (Melezhik et al., 2013a). They occur either as upper parts of fining-upward sandstone-shale-carbonate cycles, or as thin beds in laminated siltstones (Melezhik et al., 2013a). Most of the carbonate beds are composed of fine-grained dolomite and contain tremolite needles and a significant amount of clastic quartz and sericite. Some beds contain scattered pyrite cubes. The carbonate rocks and their hosts are devoid of measurable organic carbon (Appendix A). Six carbonate beds, each a few cm thick, documented through the 104.39–31.55 m interval are characterised by whole-rock MgO/CaO ratios of 0.66 to 0.99. The Mg/Ca_{carb} (acid-soluble) ratio ranges between 0.38 and 0.58 suggesting dolomitic and mixed dolomite-calcite mineralogies. Whole-rock Al_2O_3 and SiO_2 abundances are high (2–10 wt.%, and 8–38 wt.%, respectively). All rocks show an enrichment in ^{13}C ($\delta^{13}C_{carb}$ = +4.9 to +8.2‰), whereas some samples exhibit a depletion in ^{18}O ($\delta^{18}O_{carb}$ = +15.9 to +20.3‰; Appendix A) with respect to normal marine carbonates. These isotopic ratios show a positive but statistically insignificant correlation (r =+0.70, n = 6, <90%). The abundances of Mn_{carb} range between 367 and 1670 $\mu g \cdot g^{-1}$, whereas the Sr content fluctuates between 23 and 176 $\mu g \cdot g^{-1}$, n = 85, respectively) resulting in a variable Mn/Sr ratio (3.2–30).

6.2.2. Core 12AB, carbonate rocks below the LMD (406.6–258 m)

Below the LMD, carbonate rocks occur as relatively thin, layered or massive beds (Fig. 12A, B). They are composed of calcite intergrown into xenomorphic masses and contain chamosite, albite, K-feldspar, quartz, mica and minor tremolite. Beds commonly show a well-pronounced lamination including graded units and internal erosional surfaces (Fig. 13A–D). Some intervals preserve primary clastic texture (Fig. 13E, F).

On various discrimination diagrams these carbonate rocks plot in distinct fields and along distinct dolomite-calcite alteration trends (Fig. 14). The rocks are distinct from other ZF carbonates by combination of low Sr abundances and low Mg/Ca_{carb} and $\delta^{18}O_{carb}$ values, with high Na_2O contents and high Mn/Sr_{carb} (Fig. 14D, E, G, H, I, L, M–U; Appendix B). Both $\delta^{18}O_{carb}$ and $\delta^{13}C_{carb}$ correlate negatively with the sodium abundances (Fig. 14P, Q). Although $\delta^{18}O_{carb}$ and $\delta^{13}C_{carb}$ correlate positively (r = +0.55, n = 148, >99.9%), the rocks are markedly depleted in ^{18}O ($\delta^{18}O_{carb}$ = +11.5 to +15.4‰), whereas $\delta^{13}C_{carb}$ exhibits a large fluctuation between -13.5 and +2‰ (Fig. 14L). This type of carbonate has variable contents of SiO_2, TIC, total organic carbon (TOC), and total sulphur (TS). The abundances of Mn_{carb} and Fe_{carb} are high (1983 ± 1146 $\mu g \cdot g^{-1}$, and 8840 ± 7631 $\mu g \cdot g^{-1}$, n = 85, respectively). There are no or minimal through-bed geochemical and/or isotopic variations (Fig. 15A).

The highest MgO/CaO_{wr} (whole-rock) ratios measured in these carbonates correspond to near stoichiometric dolomite (0.71), though in six cases it ranges between 0.82 and 0.97 (Figs 10C and 14A–I, O, R). In contrast, the highest measured Mg/Ca_{carb} (acid-soluble) ratio is <0.1 (Figs 10D and 14D–G, T, U). In the intervals where high MgO/CaO_{wr} ratios and MgO_{wr} abundances correspond to low Mg/Ca_{carb} ratios and Mg_{carb} content (Fig. 10D, E), whole-rock Al_2O_3 and Fe_2O_3 abundances are relatively high (Figs 10G, H and 14O, R), whereas Fe_{carb} is similar to other carbonate rocks (Figs 10I and 14U). Consequently, in such intervals the abundances of Al_2O_3, Fe_2O_3 and MgO are linked to presence of an Al-Fe-Mg silicate, namely chamosite.

6.2.3. Core 12AB, carbonate rocks within the LMD (258–233 m)

The LMD comprises several discrete carbonate units separated by thin greywacke interlayers. Some carbonate units are massive and texturally homogeneous (Figs 16A and 17A), whereas others show distinct bedding and are composed of several mudstone-draped beds (Fig. 12C). The LMD includes carbonate rocks with variable mineralogy ranging from pure dolomitic, through mixed dolomitic-calcitic, to calcitic. Consequently, the overall MgO/CaO_{wr} ratio ranges between 0.02 and 1.2, whereas Mg/Ca_{carb} fluctuates between 0.01 and 0.63 (Fig. 10C, D). Carbonate beds of various compositions are either interlayered or occur as discrete, chemically and isotopically zoned units, where the core is commonly more dolomitic with respect to the margins (Črne et al., 2014). Most of the calcitic and mixed dolomitic-calcitic rocks contain abundant talc (Figs 16–17).

The LMD dolostones with insignificant degree of calcitisation, when both MgO/CaO_{wr} and Mg/Ca_{carb} ratios are close to that of stoichiometric dolomite, are often hosted by organic-rich greywackes (Fig. 10N) or occur as thin interbeds within thicker units of variably calcitised dolostones, or in the core of beds with calcitised margins (Fig. 15C, D; for details, see Črne et al., 2014). The dolostones commonly show bedded texture (Fig. 16A) and frequently are composed of tightly intergrown euhedral or xenomorphic crystals of dolomite separated by thin films of organic matter (Fig. 16B).

Variably calcitised dolostones of the LMD are characterised by granular, massive and/or bedded/layered textures (Figs 16A and, 17A). Some intervals display primary clastic microstructure and preserved intraclasts, hence indicating redeposition of carbonate material (Figs 17B–D). The rocks are commonly composed of intergrown euhedral or xenomorphic crystals of dolomite partially or entirely replaced by calcite and talc (Figs 16C–E and 17E, G), and separated by thin films of organic matter (Figs 16F and 17F). Some intervals contain abundant extensional cracks filled with white calcite (Fig. 17A).

On various discrimination diagrams the LMD carbonate rocks plot mainly together with the carbonate rocks occurring above the LMD in Core 12AB and 13A (Fig. 14A–K, O, P, R, T–U), or only in Core 12AB (Fig. 14L–N, Q, S). However, on several plots the LMD carbonates partially overlap with rocks located below the LMD (Fig. 14A–G, L, O–Q, S–U). Perhaps, acting as an alteration shield or seal, the LMD carbonates recorded the geochemical characteristics and alteration history of all phases. The LMD carbonate rocks have highly variable SiO_2, K_2O, TIC, TOC, TS, Fe_2O_{3wr}, Sr_{carb} and Fe_{carb}, contents, and highly variable Mn/Sr_{carb}, $\delta^{18}O_{carb}$, $\delta^{13}C_{carb}$ values (Figs 10, 14 and 15). Although $\delta^{18}O_{carb}$ and $\delta^{13}C_{carb}$ correlate positively (r = +0.85, n = 56, >99.9), the correlation is driven by the presence of two separate subsets each showing no correlation between the two parameters. One subset, low $\delta^{18}O_{carb}$ (+13.7 to +16.0‰) and $\delta^{13}C_{carb}$ (-11.3 to -0.9‰), plots in the field of the underlying carbonates, whereas the other subset of higher $\delta^{18}O_{carb}$ (+15.4 to +19.3‰) and $\delta^{13}C_{carb}$ (+0.1 to +8.2‰) overlaps with the rocks overlying the LMD (Fig. 14L). Črne et al. (2014) reported $\delta^{18}O_{carb}$-$\delta^{13}C_{carb}$ correlation on the scale of a single bed. The correlation is driven by pervasive calcitisation of primary dolostone where the late calcite phase is depleted in ^{13}C and ^{18}O.

Considering further the entire LMD interval, Fe_2O_{3wr}, Fe_{carb} content, Mn/Sr_{carb} values and Sr_{carb} abundances show well-pronounced stratigraphic trends starting from 255.5 m (Fig. 10H, I, L, M). The Sr_{carb} exhibits an erratic decrease from 300 to 30 $\mu g \cdot g^{-1}$. In contrast, Fe_2O_{3wr}, Fe_{carb} contents and the Mn/Sr_{carb} ratio shows an irregular increase with the stratigraphy (from 2 to 8 wt.%, from 400 to 55000 $\mu g \cdot g^{-1}$, and from 2 to 100, respectively). Individual beds commonly show well-pronounced through-bed compositional, geochemical and isotopic variations (Fig. 15A). In such cases, the margins are composed of variable or completely calcitised dolomite which is depleted in both ^{13}C and ^{18}O, whereas the cores have dolomitic compositions and significantly higher $\delta^{13}C_{carb}$ (by up to 17‰) and $\delta^{18}O_{carb}$ (by up to 8‰) (for details, see Črne et al., 2014). In fact, all calcitised dolostones, regardless of dolomite/calcite ratio, have lower $\delta^{18}O_{carb}$ and $\delta^{13}C_{carb}$ values with respect to the stratigraphically corresponding dolostones. $\delta^{13}C_{carb}$ ranges between -11 and -2‰ (+2 to +8‰ in corresponding dolostones) with the lowest values in pure calcitic rocks where both MgO/CaO_{wr} and Mg/Ca_{carb} ratios are low. $\delta^{18}O_{carb}$ is invariably low, fluctuating around +14‰ (Fig. 15B–E).

6.2.4. Cores 12AB and 13A, carbonate rocks above the LMD

Carbonate rocks occurring above the LMD (upper carbonates hereafter) include rocks with variable mineralogy ranging from pure dolomitic, through mixed dolomitic-calcitic, to calcitic. Consequently, the overall MgO/CaO_{wr} ratio ranges between 0.03 and 1.5, whereas Mg/Ca_{carb} fluctuates between 0.01 and 0.65 (Fig. 10C, D). Carbonate beds of various composition are either interlayered or occur as discrete, chemically and isotopically zoned units where the core is commonly more dolomitic with respect to margins (Fig. 15E). The calcitic and mixed dolomitic-calcitic rocks contain abundant talc. Similar to other carbonates of Core 12AB, calcite and talc formed through silicate-dolomite reaction (Črne et al., 2014). The dolostones with insignificant degree of calcitisation, when both MgO/CaO_{wr} and Mg/Ca_{carb} ratios are close to that of stoichiometric dolomite, are most abundant in the uppermost part of Core 13A (Fig. 10C, D). Here they form several meter-thick, coherent units (e.g., Fig. 15F).

Overall, upper carbonates are characterised by diverse texture microfabrics (Figs 18–19). They are either massive or bedded (Figs 18A and 19A). The two examples of the latter are syn-depositionally brecciated in the upper part of Core 13A (see lithological columns in Figs 10 and 18, Core 13A). The carbonate rocks are commonly composed of intergrown euhedral crystals of dolomite separated by thin films of organic matter (Fig. 20A, I–K), and in some intervals are partially replaced by calcite and talc. Preserved intraclasts indicate redeposition of carbonate material (Figs 18B and 20D).

Variably calcitised dolostones occurring in the 172 to 173 m interval in Core 12AB are rather massive but show thin, curly laminae of organic-rich dolomicrite embedded into sparry dolomite matrices with clotted microfabrics (Fig. 19); the overall pattern resembles a microbial microstructure (e.g., Harwood and Sumner, 2012). In some intervals, these probable microbial carbonates include several mm-thick bands composed of tightly-packed, randomly-oriented, 1-mm-long, rod-shaped crystals of dolomite, in places partially replaced by pyrite (Fig. 19D).

Insignificantly calcitised dolostones are a characteristic feature of the upper part of Core 13A. They occur as thick coherent units. The rocks are commonly layered and contain thick intervals of massive and laminated cherts (Fig. 15F). Several thick intervals show *in situ* brecciation and cementation by pyrobitumen-rich material (Črne et al., 2013b). Both bedded and brecciated dolostone rocks contain insignificant volumes of siliciclastic material (Figs 10B, G and 15E), and are characterised by variable microstructures (Fig. 20). Some intervals are composed of tightly-packed, large, euhedral dolomite crystals separated by thin films of organic-rich material. Such a lithology contains spherical clots of organic-rich, fine-grained dolomite (Fig. 20A) or areas enriched in pyrobitumen (Fig. 20B). There are beds showing primary parallel bedding and clastic microstructure (Fig. 20C–E). The clasts are rounded and composed of either microsparitic dolomite or euhedral dolomite crystals embedded into organic-rich matrix (Fig. 20D, E). Some beds exhibit diffuse bedding. The latter is expressed by irregular alternation of white, organic-poor and black organic-rich layers with patchy distribution of pyrobitumen (Fig. 20F–H). The most dominant microstructural pattern of the uppermost dolostone is characterised by the presence of tightly packed, small (0.1 mm), euhedral, dolomite crystals separated by thin films of organic-rich material (Fig. 20I). Re-crystallisation leads to the formation of larger dolomite crystals accompanied by segregation of pyrobitumen (Fig. 20J–L).

On various discrimination diagrams the upper carbonate rocks of Core 12AB and 13A show complete (Fig. 14A–K, P, R–U) or partial (Fig. 14L–N, O, Q) overlap and they plot mainly together with the carbonate rocks of the LMD (Fig. 14A–K, O, P, R, T–U). Although the upper carbonates of Core 12AB and Core 13A show considerable overlap, some cross-plots also display differences. For instance, the upper carbonates of Core 13A (n = 102) are characterised by strong, significant (>99.9%), negative $\delta^{13}C_{carb}$-SiO_2 (-0.42), $\delta^{18}O_{carb}$-SiO_2 (-0.67) and $\delta^{18}O_{carb}$-Sr (-0.47) correlations, and positive correlation between $\delta^{13}C_{carb}$ and $\delta^{18}O_{carb}$ (+0.66). In contrast, in Core 12AB (n = 238) the correlation between all these parameters, except $\delta^{13}C_{carb}$-$\delta^{18}O_{carb}$, is insignificant. Carbonates in both cores show a significant negative $\delta^{13}C_{carb}$-Sr and SiO_2-Mg/Ca correlation; however, the correlation in Core

13A (-0.70 and -0.63, respectively) is again stronger than in Core 12AB (-0.54 and -0.52, respectively). In the overall dataset the negative correlation between $\delta^{13}C_{carb}$ and Sr is driven by mineralogical composition: ^{13}C-depleted calcite has higher Sr content with respect to ^{13}C-richer dolomite (see Fig. 14D, F).

The upper carbonate rocks have variable SiO_2, K_2O, TIC, TOC, TS, Fe_2O_{3wr}, Sr_{carb} and Fe_{carb} contents, and variable Mn/Sr_{carb}, $\delta^{18}O_{carb}$, $\delta^{13}C_{carb}$ values (Figs 10, 14 and 15E, F). Most of the carbonates are devoid of Na_2O. Considering the upper carbonates in their entirety, the Mg/Ca_{carb} ratios show a stepwise stratigraphic change. The lower rapid change from predominantly dolomitic to calcite-talc rocks occurs in Core 12AB at c.162 m, just above the upper clay-ball interval (Fig. 10D and lithological column). The upper rapid switch from predominantly calcite-talc rocks to dolostones occurs in both cores above the upper volcanic units. The uppermost dolostones of Core 13A alone show erratic stratigraphic increase of Fe_2O_{3wr} (0.1→8 wt.%), Fe_{carb} (500→50000 $\mu g \cdot g^{-1}$) and K_2O (0.01→4 wt.%) contents and Mn/Sr_{carb} ratio (3→46) (Fig. 10H, I, K, M).

Individual beds commonly show well-pronounced through-bed compositional, geochemical and isotopic variations (Fig. 15E). In such cases, margins are composed of variable or completely calcitised dolomite which is depleted in both ^{13}C and ^{18}O, whereas the core has dolomitic composition and significantly higher $\delta^{13}C_{carb}$ (for details, see Črne et al., 2014).

6.3. Identified post-depositional processes affecting mineralogical and C-isotopic composition of the ZF carbonate rocks.

The post-depositional history of the ZF section was governed by diverse geological processes starting from organic diagenesis, hydrothermal/metasomatic alteration and seafloor bitumen seeps triggered by semi-contemporaneous emplacement of the basin-scale gabbro sill, followed by oil generation, its migration and thermal maturation, regional metamorphism, and finally by post-metamorphic alterations (Melezhik et al., 1999b; Črne et al., 2014; see also Fallick et al., submitted).

6.3.1. Alteration associated with regional metamorphism

The dolomite + quartz + sericite ± K-feldspar +calcite + talc metamorphic mineral paragenesis is widespread in Cores 12AB and 13A within and above the LMD (Figs 14, 16 and 17). This is a common mineral association developed in impure dolomitic rocks that have undergone low-temperature, greenschist-facies metamorphic alteration, and represents robust evidence that the dolomite reacted with silicates to produce calcite and talc (See equation 1)

Tremolite is rare. It was observed in dolostones and dolomarls from the lowermost part of the ZF in Core 11A and in one sample located above the gabbro sill in Core 12AB. Similarly to talc, it forms through dolomite-quartz reaction but under high-temperature greenschist facies metamorphism (Winkler, 1979):

$$5CaMg(CO_3)_2 + 8SiO_2 + H_2O \rightarrow Ca_2Mg_5Si_8O_{22}(OH)_2 + 3CaCO_3 + 7CO_2 \quad (2)$$

The alteration of depositional $\delta^{13}C_{carb}$ values of primary dolomite phase in the ZF through metamorphic reaction (1) was already reported by Črne et al. (2014). A larger database (n = 613) demonstrates that intervals with high MgO/CaO_{wr} ratios correspond to low Mg/Ca_{carb} ratios, low TIC content, associated with depletion in ^{13}C and formation of calcite and talc (Figs 10B, C, D, O and 15B–E). This is also supported by a significant, positive correlation of $\delta^{13}C_{carb}$ with Mg/Ca_{carb} ratios (r = +0.60, n = 456, >99.9%; Fig. 14F), and negative correlation with SiO_2 (r = -0.26, n = 456, >99%; Fig. 14S) suggesting that alteration was largely associated with reaction (1). Such reaction is accompanied by degassing of ^{13}C- and ^{18}O-enriched CO_2 with concomitant depletion of newly formed carbonates in both isotopes by a few per mil (Nabelek et al., 1984; Valley, 1986). Consequently, the calcitisation and depletion of primary C- and O-isotopic values by a few per mil in carbonates containing talc and tremolite represents an impact of the regional greenschist metamorphism on the ZF dolostones.

Although the dolomitic MgO/CaO_{wr} and low Mg/Ca_{carb} ratios observed in numerous intervals (Figs 10C, D and 15B–E) can be explained by the calcitisation of dolostones and the formation of calcite + talc ± dolomite metamorphic paragenesis (Figs 16C–F and 17G), in some intervals, MgO/CaO_{wr} exceeds the ratio of stoichiometric dolomite (0.71) (Fig. 10C). Consequently, magnesium was partially mobile during the alteration.

6.3.2. Organic diagenesis

Carbonate and siliciclastic rocks comprising the lower part of the ZF (e.g., Core 11A) are devoid of organic matter, and hence were unlikely to have been affected by organic diagenesis. However, such an effect is likely for all carbonate rocks containing significant amounts of organic matter and/or hosted by organic-rich siliciclastic rocks. The presence of carbonate rocks with low $\delta^{13}C_{carb}$ (values down to -22.5‰; Črne et al., 2014) significantly below those commonly produced through dolomite-silicate reaction associated with greenschist-facies metamorphic conditions, and a large magnitude of $\delta^{13}C_{carb}$ depletion of calcite relative to stratigraphically corresponding dolomite (up to 17‰; Črne et al., 2014) cannot be explained by metamorphic volatilisation alone (e.g., Valley, 1986) and require an external source of ^{13}C-depleted fluids involving oxidation of organic matter. Hence, in organic-matter-rich locations, mineral reactions associated with chemical reduction-oxidation processes during diagenesis are suggested as the earliest apparent process affecting mineralogical, geochemical and isotopic composition of primary carbonate precipitates.

Fe- and Mn-oxides are largely available in greywacke-siltstone-shale turbidites of the Zaonega formation. Sulphides are abundant and their isotopic composition suggests bacterial sulphate reduction (Shatsky, 1990; Melezhik et al., 1999b). Consequently, the recycling of organic matter involving thermal and bacterial reduction of sulphates and Fe- and Mn-oxides is the most probable early diagenetic source for ^{13}C-depleted CO_2; this can explain the entire measured $\delta^{13}C_{carb}$ range of the ZF carbonates significantly depleted in ^{13}C. The absence of ^{13}C-rich diagenetic carbonates indicates no biogenic CO_2 reservoirs related to active biological methanogenesis (cf. Irwin et al., 1977).

Involvement of local or global methanotrophy was suggested to explain a prominent negative shift of $\delta^{13}C$ documented in the organic matter of the ZF (Qu et al., 2012). However, methanotrophy is typically associated with formation of ^{13}C-depleted authigenic carbonates with $\delta^{13}C_{carb}$ values less than -25‰ (Irwin et al., 1977; Kauffman et al., 1966; Schoell 1980, 1988; Cavagna et al., 1999; Stakes et al., 1999; Peckmann et al., 2002). However, with the presence of abundant organic matter having low $\delta^{13}C_{org}$ (Filippov and Golubev, 1994; Kump et al., 2011; Qu et al., 2012) there are only two carbonate samples with $\delta^{13}C_{carb}$ < -20‰. Carbonates depleted in ^{13}C below such a value are absent in the ZF even in the interval containing the lowest $\delta^{13}C_{org}$ of -42‰. The latter has been interpreted either to reflect intense oxidative weathering of rocks on a global scale (Kump et al., 2011) or to be influenced by methane cycling on a basinal scale (Qu et al., 2012; Lepland et al., 2014).

Finally, whilst thermal and biogenic methane were likely components of the depositional and diagenetic environments, their isotopic imprint is not explicit in the existing

$\delta^{13}C_{carb}$ database and there is no obvious demand for the involvement of ^{12}C from CH_4 in the formation of ZF carbonates.

6.3.3. Pre-metamorphic alteration associated with emplacement of the basin-scale gabbro sill

Calcitic rocks occurring in Core 12AB below the LMD contain chamosite rather than talc. Considering that the highest MgO/CaO_{wr} ratios mostly remain close to stoichiometric dolomite (Fig. 10C), we suggest that low Mg/Ca_{carb} ratios combined with dolomitic MgO/CaO_{wr} ratios are likely associated with calcitisation of a dolomite precursor with the leached Mg bound into chamosite. Here, the carbonates are also enriched in Na_2O (Fig. 10J), but a considerable number of samples above 250 m show Na_2O content below the detection limit of 0.1 wt.% (the sodium distribution is discussed further in Fallick et al., submitted).

The severe calcitisation and considerable enrichment of all rocks in Na_2O near the gabbro indicate that sodium and calcium alterations were very likely coupled with the emplacement of the basin-scale gabbro body. Such emplacement might have compromised seals of the Tulomozero halite and sulphate deposits, and caused their partial dissolution and remobilisation of Na and Ca that were eventually involved in the alteration processes of the ZF rocks. This is supported by the presence of halite and sylvinite micro-inclusions in the ZF organic-rich rocks reported by Kulikova (2013). Magnesium liberated from the decomposed dolomite, and externally supplied Fe, could have replaced sericite to form chamosite resulting in the calcite-chamosite metasomatic paragenesis. Hence, strictly speaking, the chamosite-bearing calcitic rocks below the LMD are not sedimentary limestones *per se*, but rocks formed through metasomatic alteration of dolostones.

However, in some intervals below the LMD, the MgO/CaO_{wr} ratio is <0.1 (Figs 10C and 15A). Such ratios allow the primary phase to be calcite and not dolomite. This is also supported by various cross-plots in which these calcitic rocks plot separately from the rest of the ZF carbonates (Fig. 14). Low-MgO/CaO_{wr} carbonate rocks may represent either primary carbonate precipitates or diagenetically formed calcite concretions. Given only 52 mm width of core, differentiation between thin carbonate beds/layers and lenticular and large lensoidal concretions is challenging. However, small, lensoidal, calcite concretions are readily recognisable in Core 12AB and are abundant below the LMD (Fig. 11H; for more information, see Črne et al., 2013a), hence some analysed calcitic intervals may represent originally calcitic carbonate nodules. On the other hand, the petrographic features of some carbonate intervals also suggest that they were originally redeposited carbonate rocks (Fig. 13E, F), perhaps calcitic in composition.

6.3.4. Post-metamorphic calcitisation

Throughout Cores 12AB and 13A, in all types of rocks, calcite occurs as porphyroblasts superimposed on metamorphic fabrics. In shales, calcite appears as replacive, lathlike or pancake-like shapes (Fig. 21A, B). In sandstones, it forms irregular porphyroblasts superimposed on granoblastic and meta-psammitic texture (Fig. 21C). In interbedded gritstone-sandstone-siltstone rocks, porphyroblastic calcite develops preferentially in coarser lithologies, partially or completely replacing feldspar and quartz, whereas fine-grained, organic-rich siltstone remains largely unaffected.

6.4. Screening for post-depositional alteration of the carbon-isotopic composition of the ZF carbonates

The brief overview of carbonate petrology and geochemistry provided above demonstrates a complex and multiphase alteration of the ZF carbonates within an organic-matter-rich environment. The carbonate rocks of the ZF show a large variation of $\delta^{13}C_{carb}$ ranging between -22.4 and +9‰, which is in itself consistent with post-depositional alteration. The alteration of depositional $\delta^{13}C_{carb}$ values of primary dolomite phases by calcitisation was already demonstrated by Črne et al. (2014) through comparison of dolomitic, mixed calcitic-dolomitic and calcitic rocks within geochemically zoned carbonate beds (see also Fig. 15).

Črne et al. (2014) employed (Mg/Ca)*IC (being the Mg/Ca ratio multiplied by inorganic carbon content) as a screening parameter to identify the best-preserved samples, and conservatively suggested that all carbonates with (Mg/Ca)*IC < 6 are significantly altered. Consequently, only four dolostone samples were considered as the least altered: with $\delta^{13}C_{carb}$ of +8, +4 and -4‰ (at 250, 239 and 2 m in Core 12AB) and -2 ‰ (at 58 m in 13A). Here, using a larger database (n = 413), and employing the $Mn/Sr_{carb} \leq 10$ in dolomite samples (Mg/Ca ≥ 0.55) we obtained similar but not identical results from Cores 12Ab and 13A to those reported by Črne et al. (2014).

Six samples of impure dolostones and dolomarls representing the krivoserite succession in the lowermost part of the ZF (Core 11A, 104.9–31.55 m) have $\delta^{13}C_{carb}$ ranging between +4.9 and +8.2‰ and Mn/Sr ratios fluctuating between 3.2 and 30. Two dolostone samples at the base of the ZF (104.39 and 97.03) with $\delta^{13}C_{carb}$ of +4.9 and +5.3‰ have corresponding Mn/Sr of 4.1 and 3.2, and hence both can be considered as belonging to the least altered group. Similarly, one dolomarl sample at 31.55 m depth, having Mn/Sr close to 10, is apparently only slightly altered. Finally, two other samples with $\delta^{13}C_{carb}$ of +8.3 and +7.3‰ at depths 82.14 and 75.79 m, marked by Mn/Sr of 26 and 30, are apparently altered, hence their original values could be only higher. However, lack of organic matter indicates the carbonate rocks recovered by Core 11A were not affected by organic diagenesis. Their depletion in ^{13}C

was associated with the dolomite-quartz reaction in greenschist-facies metamorphic conditions, hence the expected lowering is limited to ~1 to 3 ‰, e.g., Melezhik et al. (2003).

In Core 12AB, the $\delta^{13}C_{carb}$ value of +8‰ at 249.2 m reported previously by Črne et al. (2014) as the least altered is accepted as having Mn/Sr_{carb} <10. Six new dolostone samples are added from 246.9–246.7 ($\delta^{13}C_{carb}$ = +2.6 to +4.0‰) and 243.2–243.1 m ($\delta^{13}C_{carb}$ = +3.0 to +3.3‰) intervals within the LMD. The value of +4‰ at 239 m reported by Črne et al. (2014) as belonging to the least altered group is rejected as having Mn/Sr_{carb} of 20. In the upper part of the drilled section, the Mn/Sr_{carb} ratio suggests 25 least altered samples in Cores 12AB and 13A ranging between -8.4 to -1.6‰.

Črne et al. (2014) have also utilised $\delta^{18}O_{carb}$ as an additional parameter for screening samples against postdepositional alteration. A $\delta^{13}C_{carb}$-$\delta^{18}O_{carb}$ cross plot for the 25 least-altered dolostone samples from the upper part of the ZF exhibits a significant positive correlation (r = 0.62, >99.9), which suggests that some of the least-altered samples might have been altered more strongly than others. In fact, the observed negative correlation is driven by a separate subset of four samples, all having $\delta^{13}C_{carb}$ below -6.5‰ (Fig. 22). Taking a conservative stand, these samples are considered as altered more strongly than the others and they are consequently excluded from the following reconstruction of the $\delta^{13}C_{carb}$ temporal trend.

6.5. The carbon-isotopic composition of the ZF carbonates recorded in the Onega Parametric Hole (OPH).

OPH was drilled in the southern part of the Onega palaeobasin, 70 km to the southwest of Holes 12AB and 13A (Fig. 1). The published $\delta^{13}C_{carb}$ data obtained from ZF carbonate rocks in OPH core show a large variation between -19.9 and +9.5‰ (Fig. 23). The range and a stratigraphic pattern are identical to those observed in FAR-DEEP core (Fig. 10P versus Fig. 23). The published material (Krupenik et al., 2011b) provides neither major nor trace element concentrations in samples measured for $\delta^{13}C_{carb}$, consequently the isotopic data cannot here be screened geochemically against post-depositional alteration.

The OPH $\delta^{13}C_{carb}$ data characterise two lithologically different intervals. The first represents the base of the ZF where bedded carbonate-siliciclastic rocks, locally termed the krivoserites, are devoid of organic matter. Here, several $\delta^{13}C_{carb}$ measurements define two isotopic shifts starting from the base of the ZF. They are expressed as a positive shift from +5 to +9‰ through a c. 120 m interval followed by a decline to 0‰ in a 50-m-thick succeeding succession (Fig. 23). As discussed above, the FAR-DEEP core data suggest that the alteration of primary $\delta^{13}C_{carb}$ ratios in the krivoserite succession is associated with dolomite+quartz reaction in greenschist-facies metamorphic conditions as much as 1–3‰ (e.g., Melezhik et al., 2003). It is yet to be assessed if the upper part of the krivoserite succession has been affected by ^{13}C-depleted fluids, derived from the overlying organic-rich rocks that have caused formation of carbonates with $\delta^{13}C_{carb}$ of -19‰ above krivoserites.

The second interval characterised by $\delta^{13}C_{carb}$ data represents the section where all sedimentary rocks are rich in organic matter (Fig. 23). This interval starts with a sharp $\delta^{13}C_{carb}$ drop from 0 to -19‰ which is associated with the first appearance of organic matter-rich rocks; $\delta^{13}C_{carb}$ of -19‰ was obtained from carbonate material hosted by a bed of massive organic matter-rich rock (Fig. 23). The rest of the section is characterised by $\delta^{13}C_{carb}$ ranging between -19.5 and -1‰ with one remarkable outlier at +9.5‰. As reported by Črne et al. (2014) and has been discussed above, the corresponding interval cored by FAR-DEEP holes shows a complex, severe alteration of primary $\delta^{13}C_{carb}$ ratios through organic diagenesis, metamorphic reactions and hydrothermal calcitisation. Consequently, the unscreened OPH

$\delta^{13}C_{carb}$ data from this interval cannot securely be used for deciphering primary carbon isotopic trends.

6.6. The $\delta^{13}C_{carb}$ temporal trend through the ZF

Six $\delta^{13}C_{carb}$ measurements from Core 11A define an apparent excursion in the lowermost part of the ZF. The excursion is expressed by a 3‰ positive shift from +5 to +8‰ through a 25 m interval followed by a return to +5‰ in a 50-m-thick succeeding section (Fig. 24). As Mn/Sr_{carb} ratios suggest that the two isotopically heaviest values could originally have been even higher, the positive excursion might have been somewhat larger than the trend on Figure 24 suggests.

The data published from OPH (Krupenik et al., 2011b; Fig. 23) define a similar excursion in the lowermost part of the ZF. The excursion is expressed as a 4‰ positive shift followed by a decline to 0‰ in a 170-m-thick succession (Fig. 23). Although these data were not screened for potential post-depositional alteration of the carbon isotope system caused by metamorphic reaction (very likely to be depleted in ^{13}C by 1–3 ‰; Melezhik et al., 2003), the similarity of the excursions depicted from two sites located 70 km apart likely represents a basin-wide feature and speaks for their apparent primary depositional nature. In this case, Core 11A appears to represent a condensed section with respect to that cored by the Onega Parametric Hole (Fig. 24).

The overlying 900 m of organic-rich rocks largely lack sedimentary carbonates which retain primary depositional $\delta^{13}C_{carb}$ values. However, there are three exceptional intervals, two in the middle and the other on top of the ZF. The first (246.9–246.7 m) and the second (243.2–243.1 m) are within the LMD where six least-altered values suggest a possible rapid negative shift from +8 to +3‰ over 3.8 m of stratigraphy (Fig. 25). Although very few high values at around +8‰ at 243.2 m depth have been measured (e.g., Črne et al., 2014) and they are not corroborated in neighbouring intervals in the FAR-DEEP database, a very similar value of +9.5‰ has been reported from a carbonate material hosted by an organic matter-rich schist in the middle part of the ZF in the OPH core (Krupenik et al., 2011b; see Fig. 23). Although the OPH high value is apparently located at a higher stratigraphic position than the high values seen in 13A, they are collectively taken as a hint that the high $\delta^{13}C_{carb}$ in the middle part of the ZF possibly persisted basin-wide.

Within the LMD, there are two dolostone samples in the 239.8–239.4 m interval with $\delta^{13}C_{carb}$ of +4.4 and +4.7‰. Although not recognised as being in the least-altered group based on their high Mn/Sr ratios, they can still provide insight into the global carbon cycle. Being affected/altered by organic diagenesis, their depositional $\delta^{13}C_{carb}$ values were likely higher, hence the LJIE extends to this level of stratigraphy. Similarly, another altered dolostone sample at depth 204.6 m with $\delta^{13}C_{carb}$ of +4.5 and Mn/Sr = 30 suggests that the end of the LJIE can be placed somewhat above 204 m.

Finally, 21 least-altered samples from the third interval located in the uppermost part of Cores 12AB and 13A track another apparent positive shift from -6 to -2‰ within a 57.5 m interval. This excursion appears to be rather erratic, which may suggest that some of the least-altered samples may still be significantly depleted in ^{13}C; hence the shift may require additional study.

These multiple $\delta^{13}C_{carb}$ shifts or excursions documented in Cores 11A, 12AB and 13A (with some corroboration from the Onega Parametric Drillhole) suggest that the deposition of ^{13}C-rich sedimentary carbonates extends from red beds of the underlying TF, which typifies the LJIE *per se*, to organic-rich environments signifying the SHE. Moreover, the FAR-DEEP $\delta^{13}C_{carb}$ data on the transition from the LJIE to the SHE, by far the most complete known in the world, also suggest that the overall temporal structure of the $\delta^{13}C_{carb}$ curve for the

Lomagundi-Jatuli time differs significantly from a single smooth loop (Karhu and Holland, 1996; Bekker et al., 2006; Planavsky et al., 2012). The FAR-DEEP data suggest that at the end of the excursion there are several apparent positive and negative shifts within c. 1000 m of stratigraphy. Although being the most complete record to date of the end of the event, the data do not cover the entire 900 m of stratigraphy, and hence the internal structure of the $\delta^{13}C_{carb}$ temporal trend could be even more complex.

7. Carbonate deposition during the termination of the LJIE

During Zaonega time and the termination of the LJIE, the Onega palaeobasin area was part of the rifted flank of the Karelian craton and formed its continental margin to the Svecofennian Ocean. The Zaonega basin itself was originally assigned to a rift-bound lagoon (Melezhik et al., 1999b; Lahtinen et al., 2008; Melezhik and Hanski, 2012).

The carbonate rocks occurring in the lowermost part of the ZF unconformably overlie steeply dipping Tulomozero stromatolitic dolostones. The sedimentological data available from field observations and FAR-DEEP core logging suggest that at least the initial phase of sedimentation likely represents fluvial accumulation followed by deposition in a relatively low-energy, siliciclastic-dominated, deep lacustrine setting (Melezhik et al., 2013) apparently associated with an incipient rifting of the continental margin (Fig. 26A).

Up-section, a combination of dominant, immature, turbiditic, greywacke-siltstone-shale rhythmites and subordinate, massive and bedded carbonate rocks represents a mixed siliciclastic-carbonate depositional system (Črne et al., 2013a). It was suggested that carbonate components were eroded/shed from a contemporaneous, environmentally-decoupled, carbonate platform/shelf and transported into the siliciclastic, organic-rich Zaonega basin. While some sedimentological features (such as illustrated in Figs 14F–H, 16B–D, 19B and 21D) indicate the resedimented nature of carbonate material and thus support such inference, others (Fig. 20) do not.

In order to explain the source of redeposited carbonate material in the Zaonega siliciclastic-carbonate depositional system, carbonate shedding from a nearby platform is invoked. This might have occurred during intervals of sea-level highstand as is common with Quaternary and extant rimmed carbonate platforms (e.g., Schlager et al., 1994). Because the Zaonega depositional system was prograding southward (e.g., Melezhik and Hanski, 2012), a carbonate platform is inferred to have been located somewhat to the south with respect to the study area (Fig. 26B).

A plausible abrupt switch in carbonate composition from predominantly calcitic to dolomitic at c. 258 m (Fig. 10D–F), if primary, would require involvement of different or temporally-evolving carbonate source(s). Among the calcitic allochems, there are fragments of laminated limestones (Fig. 13F) and recrystallised ooids (Črne et al.,2014), hence they were apparently resedimented to the Zaonega siliciclastic basin from an inferred, short-lived, oolitic shoal (Fig. 26B).

From c. 258 m and up-section, the primary carbonate phase in the ZF carbonate rocks is dolomite and some beds contain dolostone intraclasts (Figs 17B–D and 19C, 20A, D, E). Intervals of carbonate rocks are interbedded with greywacke-siltstone-shale rhythmites and represent a minor component of the turbiditic succession; carbonate rocks are rather impure (Figs 10A, B and 15B–D). Consequently, carbonate components were very likely shed or eroded into the siliciclastic, organic-rich Zaonega basin from a single source, namely a contemporaneous, environmentally-decoupled, carbonate platform (Fig. 26B) as suggested by Črne et al. (2014).

In the middle part of Core 12AB, below the seafloor pyrobitumen spill (SFPS), some dolostone beds show distinctly different microfabrics. These include thin, curly laminae of organic-rich dolomicrite embedded in clotted, sparry dolomite matrix (Fig. 20). Such features are best interpreted as microbially-influenced precipitation of carbonates, hence the carbonate material was unlikely shed or re-deposited from a nearby carbonate platform, and thus likely accumulated *in situ*.

In the upper parts of Cores 12AB and 13A, several significant changes in petrography and geochemistry of carbonate rocks occur. Here, the dolostones form thick coherent beds, contain insignificant amount of siliciclastic material (Figs 10A, B and 15F), and often exhibit *in situ* brecciation and cementation by petroleum or bitumen (now pyrobitumen) (e.g., Črne et al., 2013b).

The dolostones are interbedded with thick intervals of massive and laminated chert. Although dolostone beds contain carbonate sand-size clasts, many of them are composed of pyrobitumen-supported, euhedral dolomite crystals (Fig. 20D). The latter observation implies original deposition in an organic-rich environment. Consequently, geochemical, petrographic and sedimentological characteristics of the dolostones from the upper part of the drilled section can best be reconciled with *in situ* carbonate accumulation in organic-rich environments with limited siliciclastic supply. We tentatively suggest that the carbonate accumulation occurred within the northward-prograding carbonate platform (Fig. 26C). *In situ* brecciated dolostone beds are interpreted as a collapsed edge of the rapidly prograding platform with later cementation of cracks by migrated petroleum to form a prominent oil trap (Melezhik et al., 2013b). An alternative explanation for the *in situ* brecciation is a seismic event induced by impact of an extraterrestrial object (Huber et al., 2014).

In the uppermost part of Core 13A, the dolostones are overlain by a thick succession dominated by thinly-bedded and laminated greywacke-siltstone deposited from turbidity currents. This suggests that the carbonate platform was drowned due to either tectonic subsidence or sea-level rise. Shortly after, it was buried beneath a several-hundred-meter-thick pile of sub-aqueously extruded tholeiitic basalts (Fig. 26D).

8. Conclusions

1. Dolostones of the Tulomozero Formation were deposited in oxic conditions on a shallow-water carbonate platform marked by a frequent switch from peritidal to tidal environment with intervening episodes of subaerial karstification, followed by a final phase of emergence and partial erosion.
2. The primary carbonate phase, the dolomite, underwent metamorphic alteration under a low-temperature greenschist facies, and exhibits only a modest degree of post-depositional alteration of $\delta^{13}C_{carb}$, which ranges between +6.8 and +11.8‰ and thus records the late phase of the Lomagundi-Jatuli Isotopic Event.
3. The measured Tulomozero dolostones reveal a positive $\delta^{13}C_{carb}$ excursion from +8 to +11.8‰ followed by gradual decline to +8‰ throughout over 300 m of stratigraphy.
4. Carbonate rocks of the overlying Zaonega Formation were originally laid down in depositional settings that evolved from a rift-bound lacustrine system through a rift-bound lagoon to a rifted, deepwater clastic shelf and to a carbonate platform.
5. The main phase of the carbonate deposition was associated with organic-rich environments typifying the Shunga Event, and evolved from shedding onto the volcanically-active, deepwater, clastic shelf to *in situ* accumulation on the carbonate platform.

6. Voluminous mafic magmatism synchronous with sedimentation in a rift setting provided enhanced heat flow, a high thermal gradient and shallow-depth oil generation and migration.
7. Pyrobitumen-rich, brecciated, platformal dolostones and cherts represent the most voluminous known fossil oil reservoir in the Onega basin.
8. Some oil traps were partially breached resulting in the seafloor oil spills. The consequences of such hydrocarbon debouchement on seafloor and water-column microbial life and water geochemistry remain to be studied.
9. The primary carbonate phase, the dolomite, underwent syn- and post-depositional hydrothermal/metasomatic alterations, organic carbon-related diagenesis, metamorphic mineral reactions, and finally a low-temperature, post-metamorphic calcitisation.
10. The multiple alterations resulted in a considerable overall variation of $\delta^{13}C_{carb}$ measured in bulk carbonate samples ranging between -22 and +8‰.
11. The least altered dolomite samples show multiple positive and negative $\delta^{13}C_{carb}$ excursions throughout over 1000 m of stratigraphy with a $\delta^{13}C_{carb}$ decline from +8‰ to below zero defining the termination of the Lomagundi-Jatuli Isotopic Event in the upper part of the Zaonega Formation.
12. The termination is followed by a prominent negative shift followed by erratic return to a near normal marine $\delta^{13}C_{carb}$ value of -2‰.
13. The existing database suggests that neither positive nor negative excursions of the least altered samples, nor the overall $\delta^{13}C_{carb}$ range, were greatly influenced by methanogenesis.

FAR-DEEP cores provide by far the most complete known $\delta^{13}C_{carb}$, geochemical and sedimentological record through the Precambrian Lomagundi-Jatuli Isotopic Event and demonstrate that only the latest phase of the event is locally associated with an enhanced accumulation of ^{12}C-rich organic matter, allowing occurrences of high $\delta^{13}C$ marine carbonates. In contrast, for the main part of the event such an association is not documented.

Acknowledgements

Elemental and isotopic data, thin and polished sections used in this contribution were obtained through two large umbrella-projects with grants provided by the Norwegian Research Council grant 191530/V30 to VAM and NERC grant NE/G00398X/1 to AEF. We thank A. Črne, the editor A. Strasser as well as one anonymous reviewer and D. Papineau for providing their valuable criticism and suggestions.

References

Akhmedov, A.M., Krupenik, V.A., Makarikhin, V.V., Medvedev, P.V., 1993. Carbon isotope composition of carbonates in Early Proterozoic sedimentary basins, Published report of the Institute of Geology. Institute of Geology, Karelian Research Centre of RAS, Petrozavodsk, Russia, 56 pp. (in Russian).

Asael, D., Tissot, F.L.H., Reinhard Ch.T., Rouxel, O., Dauphas, N., Lyons, T.W., Ponzevera, E., Liorzou, C., Chéron, S., 2013. Coupled molybdenum, iron and uranium stable isotopes as oceanic paleoredox proxies during the Paleoproterozoic Shunga Event. Chemical Geology 362, 193–210.

Baker, A.J., Fallick, A.E., 1989a. Evidence from Lewisian limestones for isotopically heavy carbon in two thousand million year old sea water. Nature 337, 352–354.

Baker, A.J., Fallick, A.E., 1989b. Heavy carbon in two-billion-year-old marbles from Lofoten-Vesterålen, Norway: Implications for the Precambrian carbon cycle. Geochimica et Cosmochimica Acta, 53, 1111–1115.

Bekker, A., Karhu, J.A., Kaufman, A.J., 2006. Carbon isotope record for the onset of the Lomagundi carbon isotope excursion in the Great Lakes area, North America. Precambrian Research 148, 145–180.

Biske, N.C., Romashkin, A.E., Rychanchik, D.V., 2004. Proterozoic peperite-structures of Lebestchina, In: Geology and Mineral Deposits. Proceedings of the Institute of Geology, Karelian Research Centre 7, 193–199 (in Russian).

Bogli, J., 1980. Karst Hydrology and Physical Speleology. Springer-Verlag, Berlin, 285 pp.

Brand, U., Veizer, J., 1980. Chemical diagenesis of a multicomponent carbonate system – 1: Trace elements. Journal of Sedimentary Petrology 50, 1219–1236.

Brasier, A.T., Fallick, A.E., Prave, A.R., Melezhik, V.A., Lepland, A., and FAR-DEEP Scientists, 2011. Coastal sabkha dolomites and calcitised sulphates preserving the Lomagundi-Jatuli carbon isotope signal. Precambrian Research. 189, 193–211.

Canfield, D.E., Ngombi-Pemba, L., Hammarlund, E.U., Bengtson, S., Chaussidon, M., Gauthier-Lafaye, F., Meunier, A., Riboulleau, A., Rollion-Bard, C., Rouxel, O., Asael, D., Pierson-Wickmannh, A-C., El Albani, A., 2013. Oxygen dynamics in the aftermath of the Great Oxidation of Earth's atmosphere. Proceedings of the National Academy of Sciences 110, 16736–16741.

Cavagna, S., Clari, P., Martire, L., 1999. The role of bacteria in the formation of cold seep carbonates: geological evidence from Monferrato (Tertiary, NW Italy). Sedimentary Geology 126, 253–270.

Condie, K.C., O'Neill, C., Aster, R.C., 2009. Evidence and implications for a widespread magmatic shutdown for 250 My on Earth. Earth and Planetary Science Letters 282, 294–298.

Črne, A.E., Melezhik, V.A., Prave, A.R., Lepland, A., Romashkin, A.E., Rychanchik, D.V. Hanski, E.J., Luo, Zh-Yu. 2013a. Zaonega Formation: FAR-DEEP Holes 12A and 12B, and neighbouring quarries, in: Melezhik, V.A., Prave, A.R., Fallick, A.E., Hanski, E.J., Lepland, A., Kump, L.R., Strauss, H. (Eds.), 2013. Reading the Archive of Earth's Oxygenation. Volume 2: The Core Archive of the Fennoscandian Arctic Russia - Drilling Early Earth Project. Series: Frontiers in Earth Sciences. Springer, Heidelberg, p. 946–1007.

Črne, A.E., Melezhik, V.A., Prave, A.R., Lepland, A., Romashkin, A.E., Rychanchik, D.V. Hanski, E.J., Luo, Zh-Yu. 2013b. Zaonega Formation: FAR-DEEP Hole 13A., in: Melezhik, V.A., Prave, A.R., Fallick, A.E., Hanski, E.J., Lepland, A., Kump, L.R., Strauss, H. (Eds.), Reading the Archive of

Earth's Oxygenation. Volume 2: The Core Archive of the Fennoscandian Arctic Russia - Drilling Early Earth Project. Springer, Heidelberg, p. 1008–1046.

Črne, A.E., Melezhik, V.A., Lepland, A., Fallick, A.E., Prave, A.R., Brasier, A.T., 2014. Petrography and geochemistry of carbonate rocks of the Paleoproterozoic Zaonega Formation, Russia: Documentation of ^{13}C-depleted non-primary calcite. Precambrian Research 240, 79–93.

Daly, J.S., Balagansky, V.V., Timmerman, M.J., Whitehouse, M.J., 2006. The Lapland-Kola orogen: Palaeoproterozoic collision and accretion of the northern lithosphere, in: Gee, D.G., Stephenson, R.A. (Eds.), European Lithosphere Dynamics. Geological Society of London Memoirs 32, 561–578.

Fallick, A.E., Melezhik, V.A., Brasier, A.T., Črne, A.E., Lepland, A., Prave, A.R. Unusual, basin scale, fluid-rock interaction in the Palaeoproterozoic Onega Basin from Fennoscandia: Preservation in calcite δ^{18}O of an ancient high geothermal gradient. Precambrian Research (submitted).

Farquhar, J., Zerkle, A.L., Bekker, A., 2014. Geologic and geochemical constraints on Earth's early atmosphere, in: Holland, H., Turekian K. (Eds.-in-Chief), Treatise on Geochemistry, 2nd Edition, Volume 6: The Atmosphere – History. Elsevier, p. 91–138.

Filippov, M.M., Golubev, A.I., 1994. Carbon isotope composition of shungite rocks, in: Filippov, M.M. (Ed.), The Organic Matter of Karelian Shungite Rocks (Genesis, Evolution and the Methods of Study). Karelian Research Centre, Petrozavodsk, pp. 32–43 (in Russian).

Galdobina, L.P., 1987. The Ludicovian Super-Horizon, in: Sokolov, V.A. (Ed.), Geology of Karelia. Nauka (Science), Leningrad, p. 59–67 (in Russian).

Galimov, I.M., Kuznetsova, N.G., Prokhorov, V.S., 1968. The problem of the composition of the Earth's ancient atmosphere in connection with results of isotopic analyses of carbon from Precambrian carbonates. Geochemistry 11, 1376–1381 (in Russian).

Glushanin, L.V., Sharov, N.V., Shchiptsov, V.V. (Eds.), 2011. The Onega Palaeoproterozoic Structure (Geology, Tectonics, Deep Structure and Minerageny). Institute of Geology, Karelian Research Centre of RAS, Petrozavodsk, 431 pp. (in Russian).

Golubev, A.I., Novikov, Y.N., 2005. Geology of uranium-vanadium deposits of the Transonega region. In: Ieshko, E.P. (Ed.), Environmental problems associated with exploitation of the Srednaja Padma deposit. Karelian Research Centre, Petrozavodsk, p. 4–13 (in Russian).

Hannah, J.L., Stein, H.J., Zimmerman, A., Yang, G., Melezhik, V.A., Filippov, M.M., Turgeon, S.C., Creaser, R.A., 2008. Re-Os geochronology of a 2.05 Ga fossil oil field near Shunga, Karelia, NW Russia. Abstract, the 33rd International Geological Congress, Oslo.

Hanski, E. J., Melezhik, V. A., 2012. Litho- and chronostratigraphy of the Palaeoproterozoic Karelian formations, in: Melezhik, V.A., Prave, A.R., Hanski, E.J., Fallick, A.E., Lepland, A., Kump, L.R., Strauss, H. (Eds.), Reading the Archive of Earth's Oxygenation. Volume 1: The Palaeoproterozoic of Fennoscandia as Context for the Fennoscandian Arctic Russia - Drilling Early Earth Project. Series: Frontiers in Earth Sciences. Springer, Heidelberg, p. 39–110.

Hanski, E.J., 2012. Evolution of the Palaeoproterozoic (2.50–1.95 Ga) non-orogenic magmatism in the eastern part of the Fennoscandian Shield, in: Melezhik, V.A., Prave, A.R., Hanski, E.J., Fallick, A.E., Lepland, A., Kump, L.R., Strauss, H. (Eds.), Reading the Archive of Earth's Oxygenation. Volume 1: The Palaeoproterozoic of Fennoscandia as Context for the Fennoscandian Arctic Russia - Drilling Early Earth Project. Series: Frontiers in Earth Sciences. Springer, Heidelberg, p. 179–245.

Harwood, C.H., Sumner, D.Y., 2012. Origins of microbial microstructures in the Neoproterozoic Beck Spring Dolomite: variations in microbial community and timing of lithification. Journal of Sedimentary Research 82, 709–722.

Heiskanen, K.I., Rychanchik, D.V., 1999. The Jatulian, Early Proterozoic, carbonates with anomalously heavy carbon of the Baltic Shield. Stratigraphy and Geological Correlation 7(6), 14–19 (in Russian).

Huber, M.S., Črne, A.E., McDonald, I., Hecht, L., Melezhik, V.A., Koeberl, Ch., 2014. Impact spherules from Karelia, Russia: Possible ejecta from the 2.02 Ga Vredefort impact event. Geology 42, 375–378.

Irwin, H., Curtis, C., Coleman, M., 1977. Isotopic evidence for source of diagenetic carbonates formed during burial of organic-rich sediments. Nature 260, 209–213.

Karhu, J.A., 1993. Palaeoproterozoic evolution of the carbon isotope ratios of sedimentary carbonates in the Fennoscandian Shield. Geological Survey of Finland Bulletin 371, 1–87.

Karhu, J.A., Holland, H.D., 1996. Carbon isotopes and the rise of atmospheric oxygen. Geology 24, 867–870.

Kauffman, E. G., Arthur, M. A., Howe, B., Scholle, P. A., 1996. Widespread venting of methane-rich fluids in Late Cretaceous (Campanian) submarine springs (Tepee Buttes), Western Interior seaway, U.S.A. Geology 24, 799–802.

Kaufman, A.J., Knoll, A.H., 1995. Neoproterozoic variations in the C-isotopic composition of seawater: stratigraphic and biogeochemical implications. Precambrian Research 73, 27–49.

Kharitonov, L.Ya., 1966. Structure and Stratigraphy of the Karelides of the Eastern Part of the Baltic Shield. Nedra, Moscow, 360 pp. (in Russian)

Koistinen, T., Stephens, M.B., Bogatchev, V., Nordgulen, Ø., Wenneström, M., and Korhonen, J., (Comps.), 2001. Geological Map of the Fennoscandian Shield, Scale 1:2 000 000, Espoo, Trondheim, Uppsala, Moscow.

Krupenik, V.A., Akhmedov, A.M., Sveshnikova, K.Yu., 2011a. Section of the Onega structure based on data from OPH (Onega parametric hole), in: Glushanin, L.V., Sharov, N.V., Shchiptsov, V.V. (Eds.), The Onega Palaeoproterozoic Structure (Geology, Tectonics, Deep Structure and Minerageny), Karelian Science Centre, Petrozavodsk, p. 172–189 (in Russian).

Krupenik, V.A., Akhmedov, A.M., Sveshnikova, K.Yu., 2011b. Carbon, oxygen and sulphur isotopic composition of rocks from Ludicovian and Jatulian Super-Horizons, in: Glushanin, L.V., Sharov, N.V., Shchiptsov, V.V. (Eds.), The Onega Palaeoproterozoic Structure (Geology, Tectonics, Deep Structure and Minerageny), Karelian Science Centre, Petrozavodsk, p. 250–255 (in Russian).

Kulikova, V.V., 2013. Halite and sylvinite as chemical indicators of different-age basins (an example from the C_{org}-bearing sediments – shungites from SE Fennoscandia), in: Vakulenko, L.G., Jan, P.A. (Eds.), Sedimentary Basins, Sedimentary and Post-Sedimentary Processes in Geological History. Proceedings of the VII All-Russia Lithological Meeting, Novosibirsk, 28–31 October, 2013, p. 138–142.

Kump, L.R., Junium, Ch., Arthur, M.A., Brasier, A., Fallick, A.E., Melezhik, V.A., Lepland, A., Črne, A.E., Luo, G. 2011. Isotopic evidence for massive oxidation of organic matter following the Great Oxidation Event. Science 334, 1694–1696.

Kump, L.R., Fallick, A.E., Melezhik, V.A., Strauss, H., Lepland, A., 2013. The Great Oxidation Event, in: Melezhik, V.A., Kump, L.R., Fallick, A.E., Strauss, H., Hanski, E.J., Prave, A.R., Lepland, A. (Eds.), Reading the Archive of Earth’s Oxygenation. Volume 3: Global Events and the Fennoscandian Arctic Russia - Drilling Early Earth Project. Series: Frontiers in Earth Sciences. Springer, Heidelberg, p. 1517–1533.

Lahtinen, R., Garde, A.A., Melezhik, V.A., 2008. Paleoproterozoic evolution of Fennoscandia and Greenland. Episodes, 31 20–28.

Lepland, A., Joosu, L., Kirsimäe, K., Prave, A.R., Romashkin, A.E.,Črne, A.E., Martin, A.P., Fallick, A.E., Somelar, P., Üpraus, K., Mänd, K., Roberts, N.M.W., van Zuilen, M.A., Wirth, R., Schreiber, A., 2014. Potential influence of sulphur bacteria on Palaeoproterozoic phosphogenesis. Nature Geoscience 7, 20–24.

Marmo, J.S., Ojakangas, R.W., 1984. Lower Proterozoic glaciogenic deposits, eastern Finland. Geological Society of America Bulletin 98, 1055–1062.

Melezhik, V.A., 2006. Multiple causes of Earth's earliest global glaciation. Terra Nova 18, 130–137.

Melezhik, V. A., 2012. The International Continental Scientific Drilling Program, in: Melezhik, V.A., Prave, A.R., Hanski, E.J., Fallick, A.E., Lepland, A., Kump, L.R., Strauss, H. (Eds.), Reading the Archive of Earth’s Oxygenation. Volume 1: The Palaeoproterozoic of Fennoscandia as Context for the Fennoscandian Arctic Russia - Drilling Early Earth Project. Series: Frontiers in Earth Sciences. Springer, Heidelberg, p. 25–30.

Melezhik, V.A., Fallick, A.E., 1996. A widespread positive $\delta^{13}C_{carb}$ anomaly at around 2.33-2.06 Ga on the Fennoscandian Shield: a paradox? Terra Nova 8, 141–157.

Melezhik, V. A., Hanski, E. J., 2012. Palaeotectonic and palaeogeographic evolution of Fennoscandia in the Early Palaeoproterozoic, in: Melezhik, V.A., Prave, A.R., Hanski, E.J., Fallick, A.E., Lepland, A., Kump, L.R., Strauss, H. (Eds.), Reading the Archive of Earth's Oxygenation. Volume 1: The Palaeoproterozoic of Fennoscandia as Context for the Fennoscandian Arctic Russia - Drilling Early Earth Project. Series: Frontiers in Earth Sciences. Springer, Heidelberg, p. 111–178.

Melezhik, V.A., Fallick, A.E., Medvedev, P.V., Makarikhin, V.V., 1999a. Extreme $^{13}C_{carb}$ enrichment in ca. 2.0 Ga magnesite-stromatolite-dolomite-'red beds' association in a global context: a case for the world-wide signal enhanced by a local environment. Earth-Science Reviews 48, 71–120.

Melezhik, V.A., Fallick, A.E., Filippov, M.M., Larsen, O. 1999b. Karelian shungite an indication of 2000 Ma-year-old metamorphosed oil-shale and generation of petroleum: geology, lithology and geochemistry. Earth-Science Reviews 47, 11–40.

Melezhik, V.A., Fallick, A.E., Medvedev, P.V., Makarikhin, V.V., 2000. Palaeoproterozoic magnesite–stromatolite–dolostone–'red bed' association, Russian Karelia: palaeoenvironmental constraints on the 2.0 Ga positive carbon isotope shift. Norsk Geologisk Tidsskrift 80, 163–186.

Melezhik, V.A., Fallick, A.E., Medvedev, P.V., Makarikhin, V., 2001. Palaeoproterozoic magnesite: lithological and isotopic evidence for playa/sabkha environments. Sedimentology 48, 379–397.

Melezhik, V.A., Filippov, M.M., Romashkin, A.E., 2004. A giant Palaeoproterozoic deposit of shungite in NW Russia: genesis and practical applications. Ore Geology Reviews 24, 135–154.

Melezhik, V.A., Fallick, A.E., Smirnov, Y.P., Yakovlev, Y.N., 2003. Fractionation of carbon and oxygen isotopes in ^{13}C-rich Palaeoproterozoic dolostones in the transition from medium-grade to high-grade greenschist facies: a case study from the Kola Superdeep Drillhole. Journal of the Geological Society 160, 71–82.

Melezhik, V.A., Fallick, A.E., Hanski, E. Kump, L., Lepland, A., Prave, A., Strauss, H., 2005a. Emergence of the aerobic biosphere during the Archean-Proterozoic transition: Challenges for future research. Geological Society of America Today 15, 4–11.

Melezhik, V.A., Fallick, A.E., Rychanchik, D.V., Kuznetsov A.B., 2005b. Palaeoproterozoic evaporites in Fennoscandia: implications for seawater sulphate, $\delta^{13}C$ excursions and the rise of atmospheric oxygen. Terra Nova 17, 141–148.

Melezhik, V.A., Fallick, A.E., Filippov, M.M., Lepland, A., Rychanchik, D.V, Deines, J.E., Medvedev, P.V., Romashkin, A.E., Strauss, H. 2009. Petroleum surface oil seeps from Palaeoproterozoic petrified giant oilfield. Terra Nova, 21, 119–126.

Melezhik, V.A., Kump, L.R., Hanski, E.J., Fallick, A.E., Prave, A.R., 2012a. Tectonic evolution and major global Earth-surface palaeoenvironmental events in the Palaeoproterozoic, in: Melezhik, V.A., Prave, A.R., Hanski, E.J., Fallick, A.E., Lepland, A., Kump, L.R., Strauss, H. (Eds.), Reading the Archive of Earth's Oxygenation. Volume 1: The Palaeoproterozoic of Fennoscandia as Context for the Fennoscandian Arctic Russia - Drilling Early Earth Project. Series: Frontiers in Earth Sciences. Springer, Heidelberg, pp. 3–21.

Melezhik, V. A., Medvedev, P.V., Svetov, S.A., 2012b. The Onega Basin, in: Melezhik, V.A., Prave, A.R., Hanski, E.J., Fallick, A.E., Lepland, A., Kump, L.R., Strauss, H. (Eds.), Reading the Archive of Earth's Oxygenation. Volume 1: The Palaeoproterozoic of Fennoscandia as Context for the Fennoscandian Arctic Russia - Drilling Early Earth Project. Series: Frontiers in Earth Sciences. Springer, Heidelberg, p. 387–490.

Melezhik, V.A., Prave, A.R., Lepland, A., Romashkin, A.E., Rychanchik, D.V., Hanski, E.J., 2013a. Tulomozero Formation: FAR-DEEP Hole 11A, in: Melezhik, V.A., Prave, A.R., Fallick, A.E., Hanski, E.J., Lepland, A., Kump, L.R., Strauss, H. (Eds.), 2013. Reading the Archive of Earth's Oxygenation. Volume 2: The Core Archive of the Fennoscandian Arctic Russia - Drilling Early Earth Project. Series: Frontiers in Earth Sciences. Springer, Heidelberg, p. 889-945.

Melezhik, V.A., Fallick, A.E., Filippov, M.M., Deines, Y.E., Črne, A.E., Lepland, A., Brasier, A.T., Strauss, H., 2013b. Giant Palaeoproterozoic petrified oil field in the Onega Basin, in*:* Melezhik, V.A., Kump, L.R., Fallick, A.E., Strauss, H., Hanski, E.J., Prave, A.R., Lepland, A. (Eds.), Reading the Archive of Earth's Oxygenation. Volume 3: Global Events and the Fennoscandian Arctic Russia - Drilling Early Earth Project. Series: Frontiers in Earth Sciences. Springer, Heidelberg, p. 1202–1212.

Melezhik, V.A., Young, G.M., Eriksson, P.G., Altermann, W., Kump, L.R., Lepland, A., 2013c. Huronian-age glaciations, in: Melezhik, V.A., Kump, L.R., Fallick, A.E., Strauss, H., Hanski, E.J., Prave, A.R., Lepland, A. (Eds.), Reading the Archive of Earth's Oxygenation. Volume 3: Global Events and the Fennoscandian Arctic Russia - Drilling Early Earth Project. Series: Frontiers in Earth Sciences. Springer, Heidelberg, p. 1059-1109.

Morozov, A.F., Hakhaev, B.N., Petrov, O.V., Gorbachev, V.I., Tarkhanov, G.B., Tsvetkov, L.D., Erinchek, Yu.M., Akhmedov, A.M., Krupenik, V.A., Sveshnikova, K.Yu., 2010. Rock-salts in Palaeoproterozoic strata of the Onega depression of Karelia (based on data from the Onega parametric drillhole). Transactions of the Russian Academy of Sciences 435(2), 230–233 (in Russian).

Mossman, D.J., Gauthier-Lafaye, Jackson, S.E., 2005. Black shales, organic matter, ore genesis and hydrocarbon generation in the Paleoproterozoic Franceville Series, Gabon. Precambrian Research 137, 253–272.

Nabelek, P.I., 1991. Stable isotope monitors, in: Kerrick, D.M. (Ed.), Contact Metamorphism, Reviews in Mineralogy 26, Mineralogical Society of America, p. 395–435.

Negrutsa, V.Z., 1984. Early Proterozoic Stages of Evolution of the Eastern Baltic Shield. Nedra, Leningrad, 270 pp. (in Russian).

Ovchinnikova, G.V., Kusnetzov, A.B., Melezhik, V.A., Gorokhov, I.M., Vasil'eva, I.M., Gorokhovsky, B.M., 2007. Pb-Pb age of Jatulian carbonate rocks: the Tulomozero Formation in south-eastern Karelia. Stratigraphy and Geological Correlation 4, 20–33 (in Russian).

Peckmann, J., Goedert, J. L., Thiel, V., Michaelis,W., Reitner, J., 2002. A comprehensive approach to the study of methane-seep deposits from the Lincoln Creek Formation, western Washington State, USA. Sedimentology 49, 855–873.

Planavsky, N.J., Bekker, A., Hofmann, A., Owens, J.D., Lyons, T.W., 2012. Sulfur record of rising and falling marine oxygen and sulfate levels during the Lomagundi event. Proceedings of National Academy of Sciences 109, 18300–18305.

Poleshchuk. A.V., 2011. Sill genesis in the Paleoproterozoic tectonic evolution of the Onega trough, Baltic Shield. Proceedings of the Russian Academy of Sciences, Earth Sciences, v.439, part 1, 939–943.

Puchtel, I.S., Arndt, N.T., Hofmann, A.W., Haase, K.M., Kröner, A., Kulikov, V.S., Kulikova, V.V., Garbe-Schönberg, C.-D., Nemchin, A.A., 1998. Petrology on mafic lavas within the Onega plateau, central Karelia: evidence for 2.0 Ga plume-related continental crustal growth in the Baltic Shield. Contributions to Mineralogy and Petrology 130, 134–153.

Puchtel, I.S., Zhuravlev, D.Z., Ashikhmina, N.A., Kulikov, V.S., Kulikova, V.V., 1992. Sm-Nd age of the Suisarian suite on the Baltic Shield. Transactions of Russian Academy of Sciences 326, 706–711 (in Russian).

Qu, Y., Črne, A. E., Lepland, A., Van Zuilen, M. A., 2012. Methanotrophy in a Paleoproterozoic oil field ecosystem, Zaonega Formation, Karelia, Russia. Geobiology 10, 467–478.

Reuschel M., Melezhik V.A., Whitehouse M.J., Lepland A., Fallick A.E., Strauss H., 2012. Isotopic evidence for a sizeable seawater sulfate reservoir at 2.1Ga. Precambrian Research 192–195, 78–88.

Schidlowski, M., Eichmann, R., Junge, C.E., 1975. Precambrian sedimentary carbonates: carbon and oxygen isotope geochemistry and implications for the terrestrial oxygen budget. Precambrian Research 2, 1–69.

Schlager, W., Reijmer, J.J.G., Droxler, A., 1994. Highstand shedding of carbonate platforms. Journal of Sedimentary Research B64, 270–281.

Schoell, M, 1980. The hydrogen and carbon isotopic composition of methane from natural gases of various origins. Geochimica et Cosmochimica Acta 44, 649–661.

Schoell, M, 1988. Multiple origin of methane in the Earth. Chemical Geology 71, 1–10.

Satzuk, Yu.I., Makarikhin, V.A., Medvedev, P.V., 1988. Jatulian Geology of the Onega-Segozero Watershed. Nauka (Science), Leningrad, 96 pp. (in Russian).

Shatsky, G.V., 1990. Isotope composition of sulphides from the Zazhogino shungite deposit. Lithology and Mineral Resources 1, 20–28 (in Russian).

Stakes, D. S., Orange, D., Paduan, J. B., Salamy, K. A., Maher, N., 1999. Cold-seeps and authigenic carbonate formation in Monterey Bay, California. Marine Geology 159, 93–109.

Tikhomirova, M., Makarikhin, V.V., 1993. Possible reasons for the $\delta^{13}C$ anomaly of Lower Proterozoic sedimentary carbonates. Terra Research 5, 244–248.

Valley, J.W., 1986. Stable isotope geochemistry of metamorphic rocks, in: Valley,J.W., Taylor, H.P., O'Neil, J.R. (Eds.), Stable Isotopes in High Temperature Geological Processes. Reviews in Mineralogy 16, Mineralogical Society of America, Washington D.C., p.445–490

Vinogradova, N.B., 2005. Characteristics of radionuclides in lakebottom sediments in the Transonega region, in: Ieshko, E.P. (Ed.), Environmental Problems Associated with Exploitation of the Srednaja Padma Deposit. Karelian Research Centre, Petrozavodsk, p. 55–58 (in Russian).

Winkler, H.G.F., 1979. Petrogenesis of Metamorphic Rocks. Springer-Verlag, Berlin, 838 pp.

www.catalogmineralov.ru. Ore deposits of Padma.

Yudovich, Y. E. Makarikhin, V. V. Medvedev, P. V., Sukhanov, N. V., 1991. Carbon isotope anomalies in carbonates of the Karelian Complex. Geochemistry International 28, 56–62.

Figures

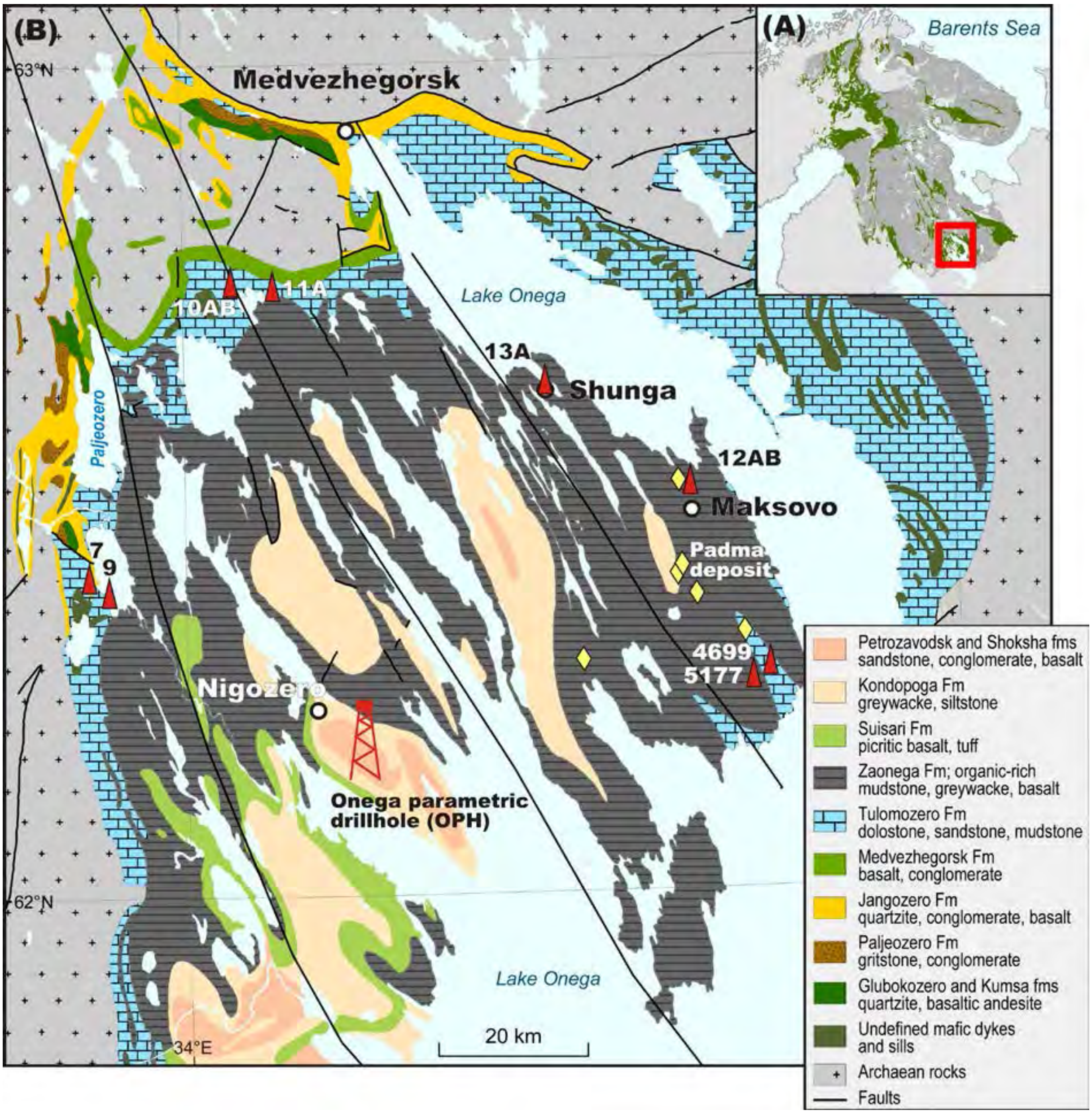

Fig. 1. (A) Geographic location of the study area. (B) Simplified geological map of the Onega palaeobasin with the locations of studied drillholes (red triangles). Geological map is based on Koistinen et al. (2001). Yellow diamonds denote positions of V-U-Mo-Pd deposits (Vinogradova, 2005).

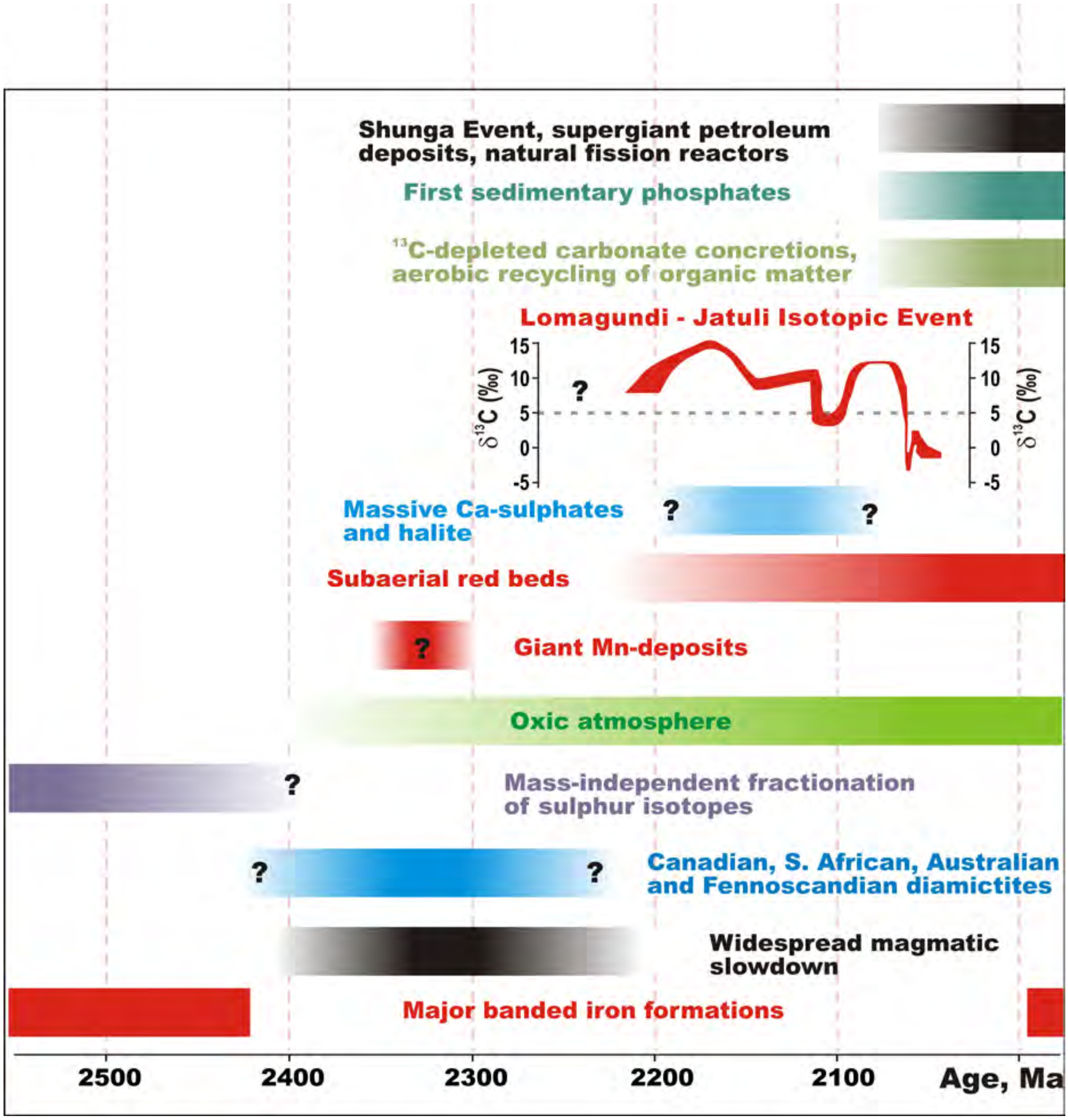

Fig. 2. Major global palaeoenvironmental and tectonic events during the Early Palaeoproterozoic. Modified from Melezhik et al. (2013a).

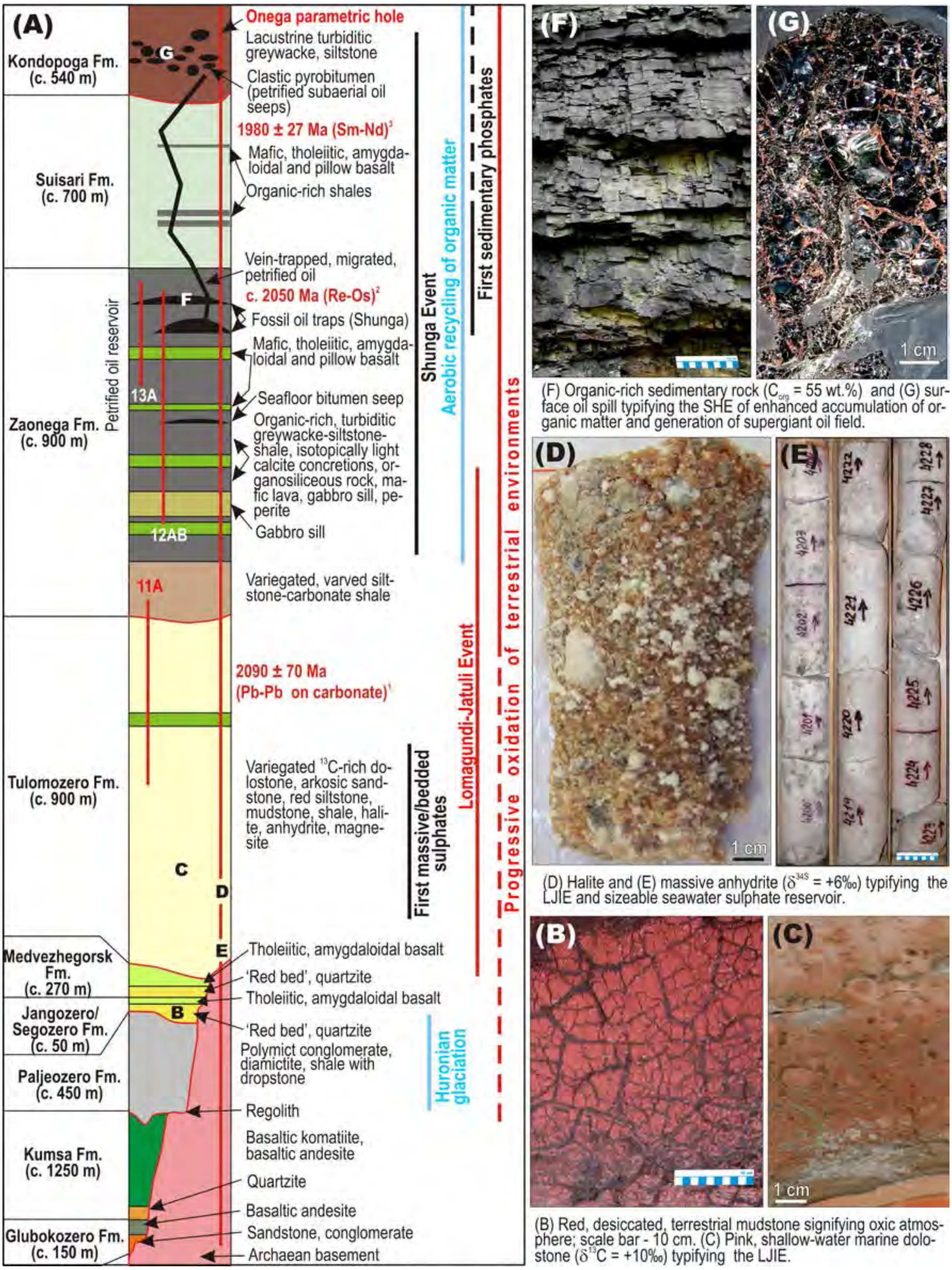

Fig. 3. (A) Lithostratigraphic column of the Onega palaeobasin with positions of FAR-DEEP and Onega parametric drillholes, and projection of global palaeoenvironmental events. Red lines separating formations denote major hiatuses. Superscripts denote radiometric ages from ([1]) Ovchinnikova et al. (2007), ([2]) Hannah et al. (2008) and ([3]) Puchtel et al. (1992, 1998). (B–G) Photos of selected sedimentary rocks from the Onega Palaeoproterozoic succession illustrating some major

global changes in Earth's palaeoenvironments; position of photos denoted in the column by (B–G). Photographs (D) and (E) courtesy of Dmitry Rychanchik.

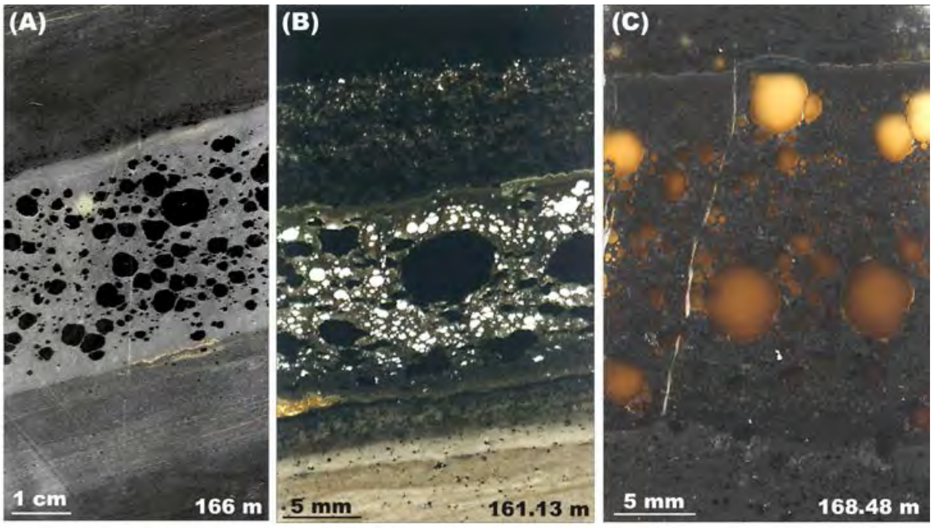

Fig. 4. (A) A scanned slab and (B) thin section showing parallel-laminated mudstone with a greywacke bed containing abundant black, kerogen-rich balls of layered alumino-silicate (illite?). (C) Scanned thin section showing abundant yellow and pale brown illite balls in massive mudstone. (A, B) – Core 12AB, (C) – Core 13A.

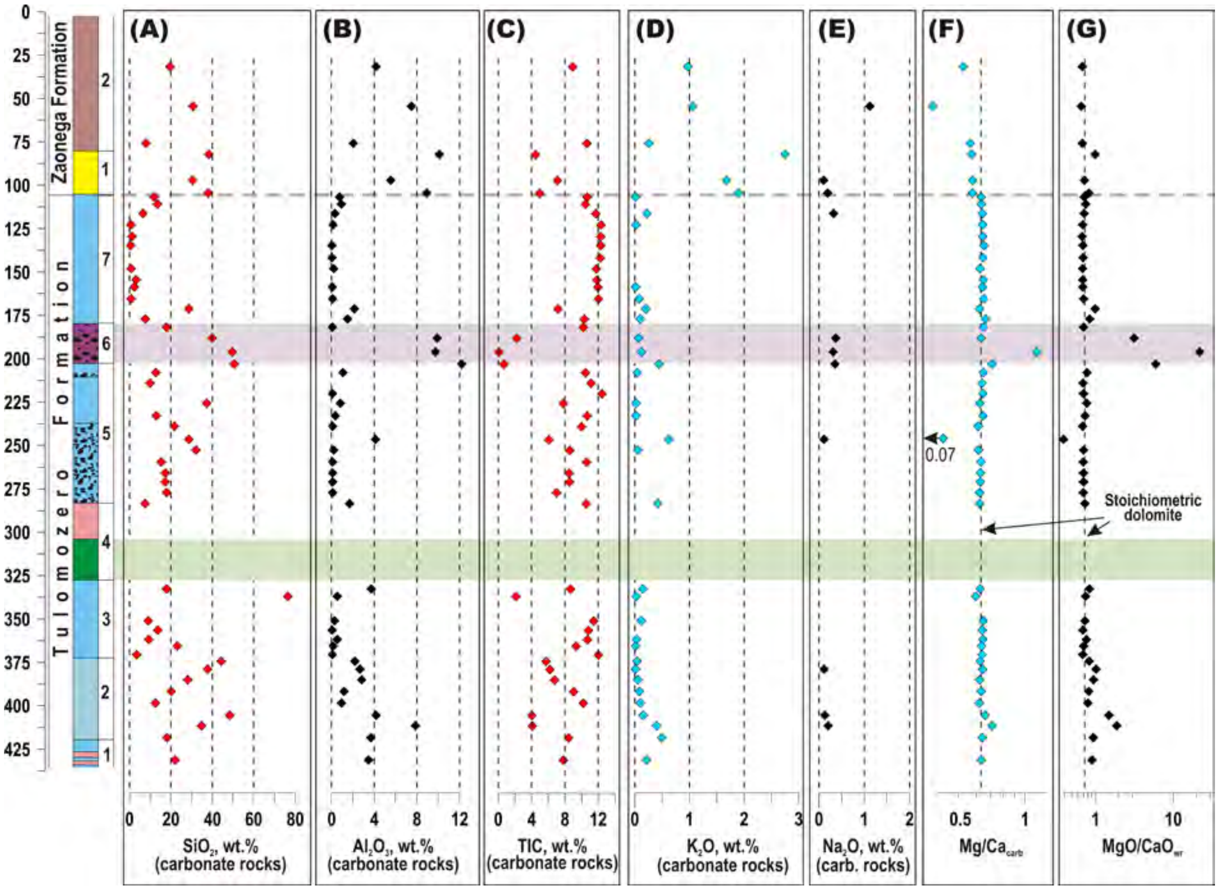
Zaonega Formation
Tulomozero Formation
(A)
(B)
(C)
(D)
(E)
(F)
(G)
SiO2, wt.% (carbonate rocks)
Al2O3, wt.% (carbonate rocks)
TIC, wt.% (carbonate rocks)
K2O, wt.% (carbonate rocks)
Na2O, wt.% (carb. rocks)
Mg/Ca carb
MgO/CaO wr
Stoichiometric dolomite
0.07

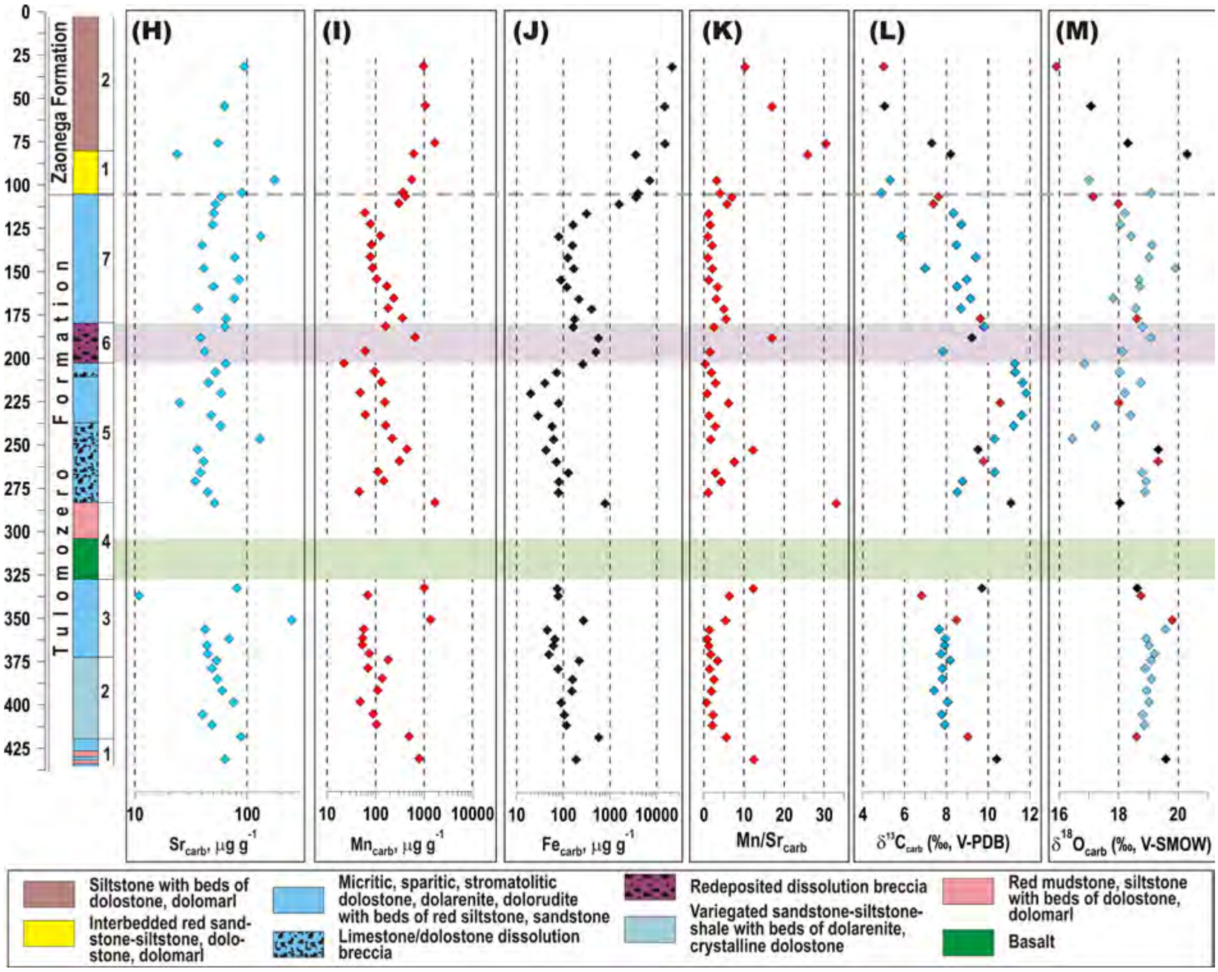

Fig. 5. Geochemical profiles through the TF based on FAR-DEEP Core 11A. Major and trace element data and isotopic composition of carbonate carbon are from FAR-DEEP database (http://far-deep.icdp-online.org). In Panels L and M, blue diamonds: Mn/Sr < 5; red diamonds: 10 ≥ Mn/Sr > 5; black diamonds: Mn/Sr >10.

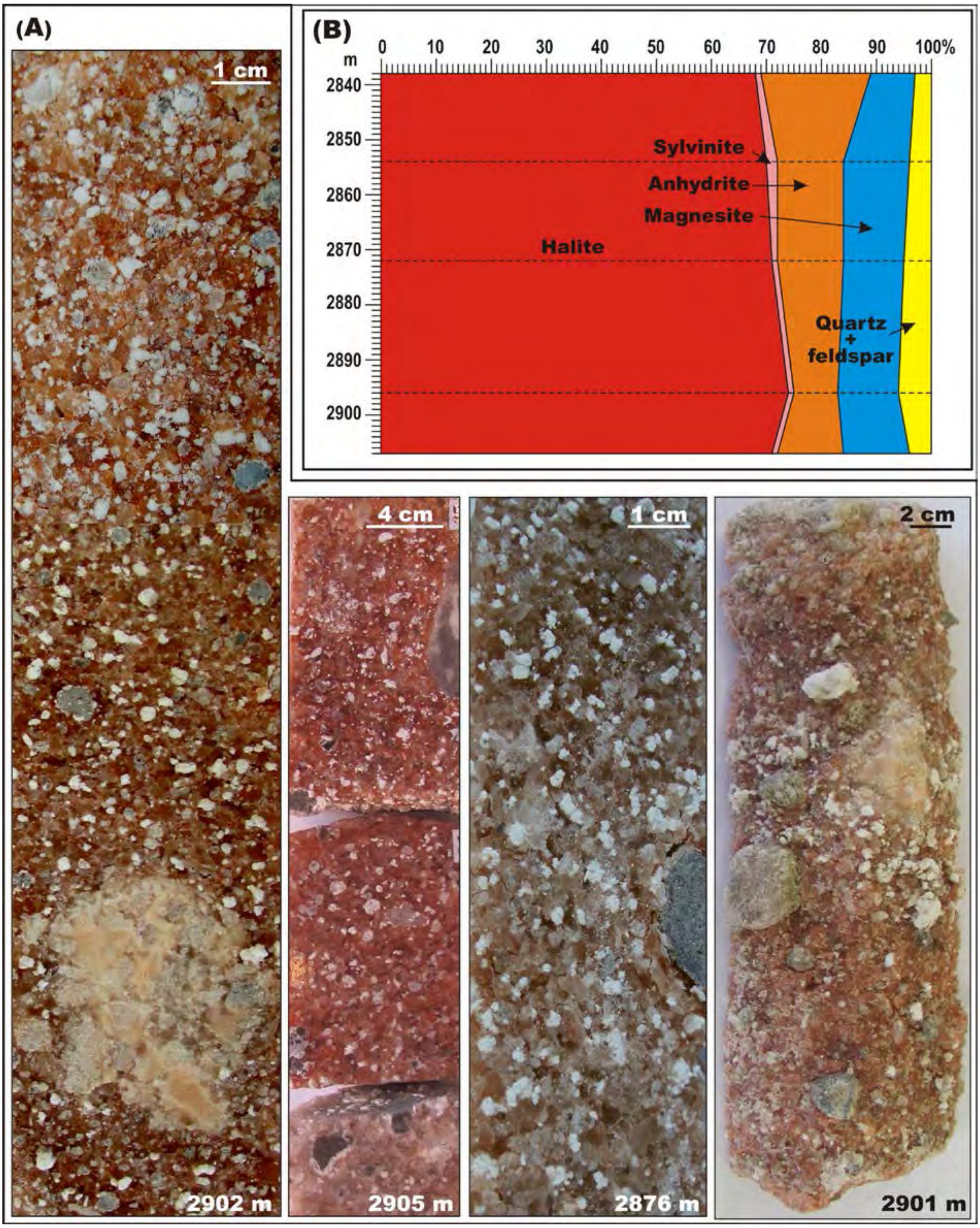

Fig. 6. (A) Sedimentological features of the halite as documented in the Onega Parametric Core. Brown and pink, massive, coarsely-crystalline halite with numerous inclusions of anhydrite (white), magnesite (yellow) and shale (pale grey). Photographs courtesy of Dmitry Rychanchik. (B) Mineralogical composition of the halite bed intersected by the Onega Parametric Drillhole at the base of the TF (based on data from Krupenik et al., 2011a).

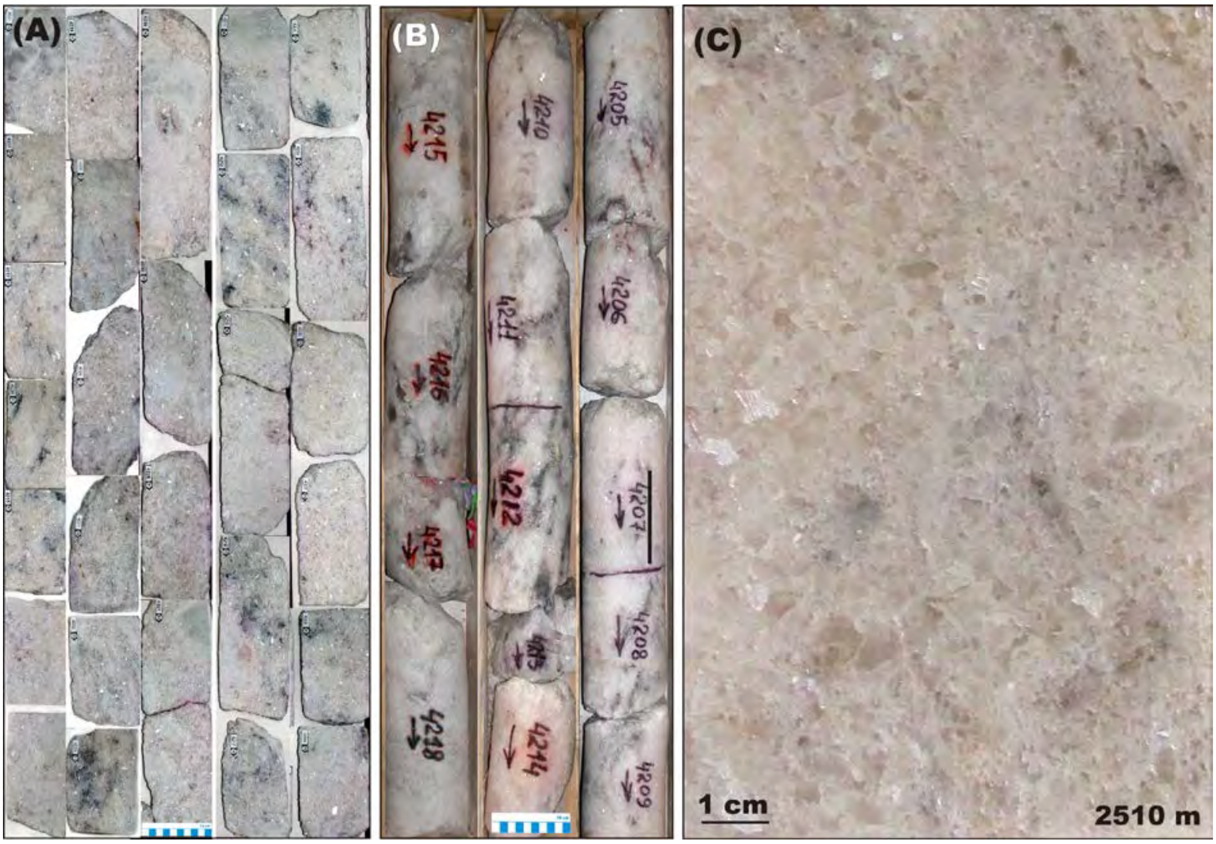

Fig. 7. (A) Selected sawn cores representing 2516–2507 m interval; (B) Selected unsawn cores from 2511–250 m interval; and (C) polished slab, illustrating massive structure of coarse-crystalline anhydrite from the Onega Parametric Core. Photographs courtesy of Dmitry Rychanchik. Scale-bars with cm divisions.


(A)
413.7 m
(B)
396.2 m
(C)
370.6 m
(D)
350.4 m
(E)
275.2 m
(F)
276.7

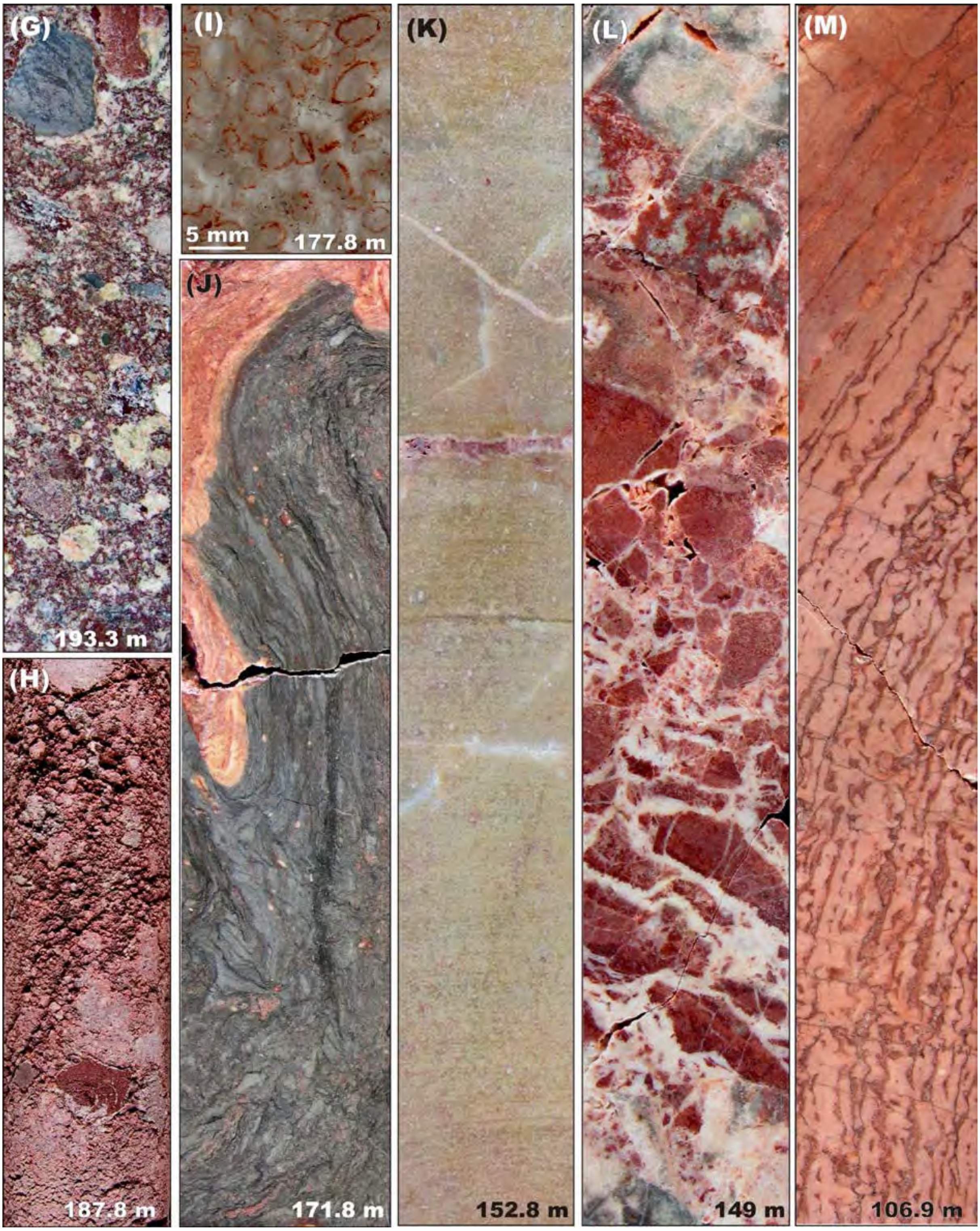

Fig. 8. Photographs illustrating the main sedimentological features of relevant rock types of the TF. Sawn and unsawn FAR-DEEP core diameter is 4 cm here and in all following photographs unless specified otherwise; numbers correspond to drillhole depth in metres. (A) Member 2: flat-laminated, red dolomarl with small rip-ups of black, magnetite-rich mudstone and network of dissolution voids and cracks cemented by white dolospar. (B) Member 2: white-pinkish, fine-grained dolostone with

bedding expressed by sparse laminae, lenses and patches of black, haematite/magnetite-rich mudstone. (C) Member 3: dolarenite-dolorudite with abundant small rip-ups of black, haematite-rich mudstone and dolosparitic fabric caused by dissolution and re-cementation (Melezhik et al., 2013a). (D) Member 3: Recrystallised, bedded dolarenite with haematite spots. (E) Member 5: dissolution-collapse breccias composed of angular, unsorted clasts of black, haematite-rich dolomarl embedded in white, drusy dolomite. (F) Member 5: unsawn core of pale pink/white dolostone and laminated grey and black, haematite-rich mudstone, exhibiting extensive soft-sediment deformation features, desiccation, partial dismembering and cementation by white dolospar; layers marked by red arrow show a possible enterolithic structure. (G) Member 6: redeposited, fragment-supported, dissolution-collapse, polymict, conglomeratic breccia composed of unsorted intraformational clasts of dolostones, dolomarls and magnesite in a clay-talc matrix. (H) Member 6: fragment-supported polymict dissolution-collapse breccias composed of unsorted intraformational clasts of dolostones and dolomarls; note that the cement is partially dissolved. (I) Member 7: photomicrograph in transmitted, non-polarised light showing recrystallised dolomitic ooids or oncoids coated with haematite (red rims). (J) Member 7: soft-sediment deformed grey shale and pink dolomarl. (K) Member 7: pale tan dolarenite with indistinct parallel bedding. (L) Member 7: dissolution-collapse breccia (karst) in dolarenite-dolorudite cemented by white dolospar. (M) Member 7: pink, stromatolitic dolostone passing upward into indistinctly-bedded microsparitic dolostone.

Photographs (A–D), (F) and (K–L) reproduced with kind permission of Springer Science+Business Media from Melezhik, V.A., Prave, A.R., Lepland, A., Romashkin, A.E., Rychanchik D.V., and Hanski E.J., (2013). 6.3.2 Tulomozero Formation: FAR-DEEP Hole 11A, in: Melezhik, V.A., Prave, A.R., Fallick, A.E., Hanski, E.J., Lepland, A., Kump, L.R., Strauss, H. (eds.) Reading the Archive of Earth's Oxygenation. Volume 2: The Core Archive of the Fennoscandian Arctic Russia - Drilling Early Earth Project. Series: Frontiers in Earth Sciences. Springer, Heidelberg, pp. 889–945. Copyright Springer Science+Business Media 2013.

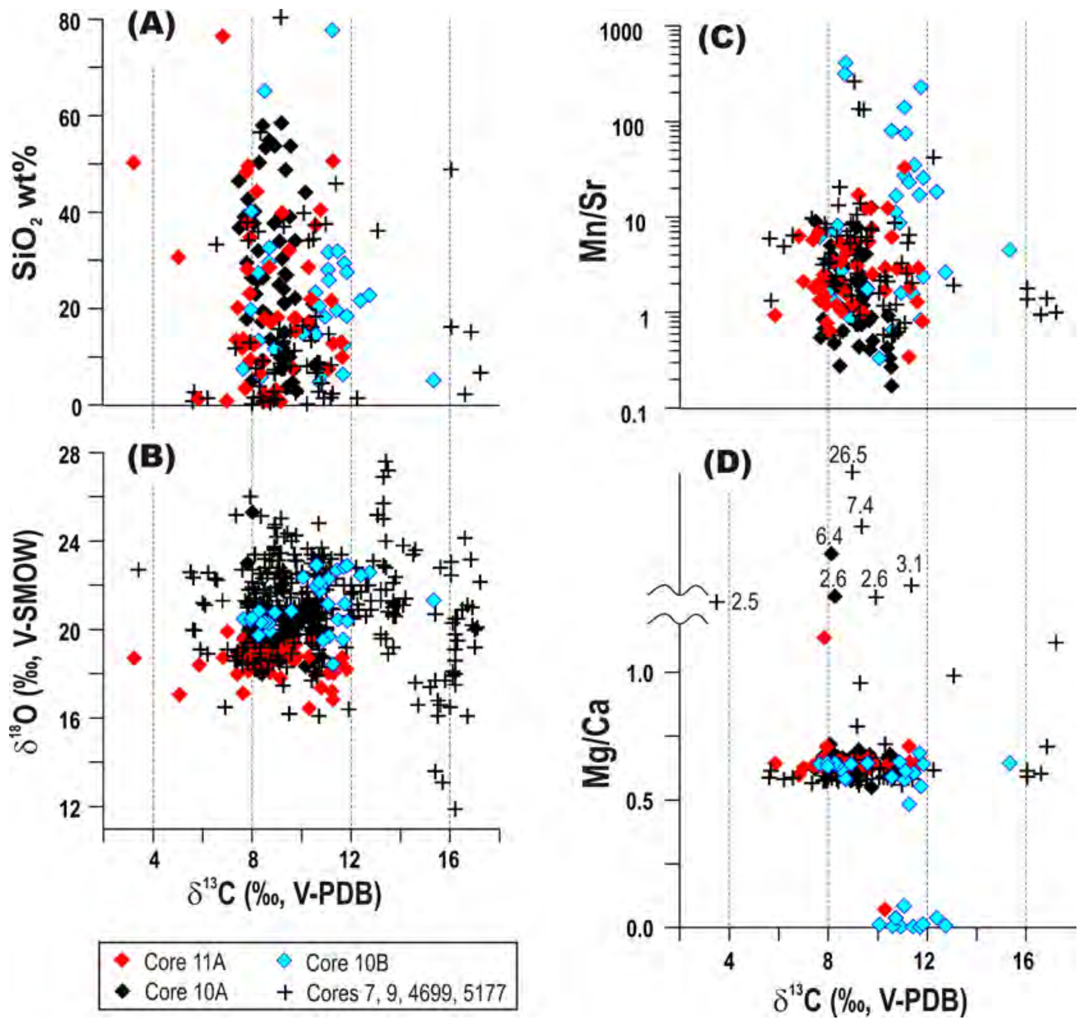

Fig. 9. $\delta^{13}C_{carb}$ plotted against $\delta^{18}O_{carb}$, SiO_2 abundances, and Mn/Sr_{carb} and Mg/Ca_{carb} ratios in the TF carbonate rocks. Data are from FAR-DEEP database (http://far-deep.icdp-online.org; core 10A, 11A), Melezhik et al. (1999a; cores 4699 and 5177) and Brasier et al. (2011; core 10B).

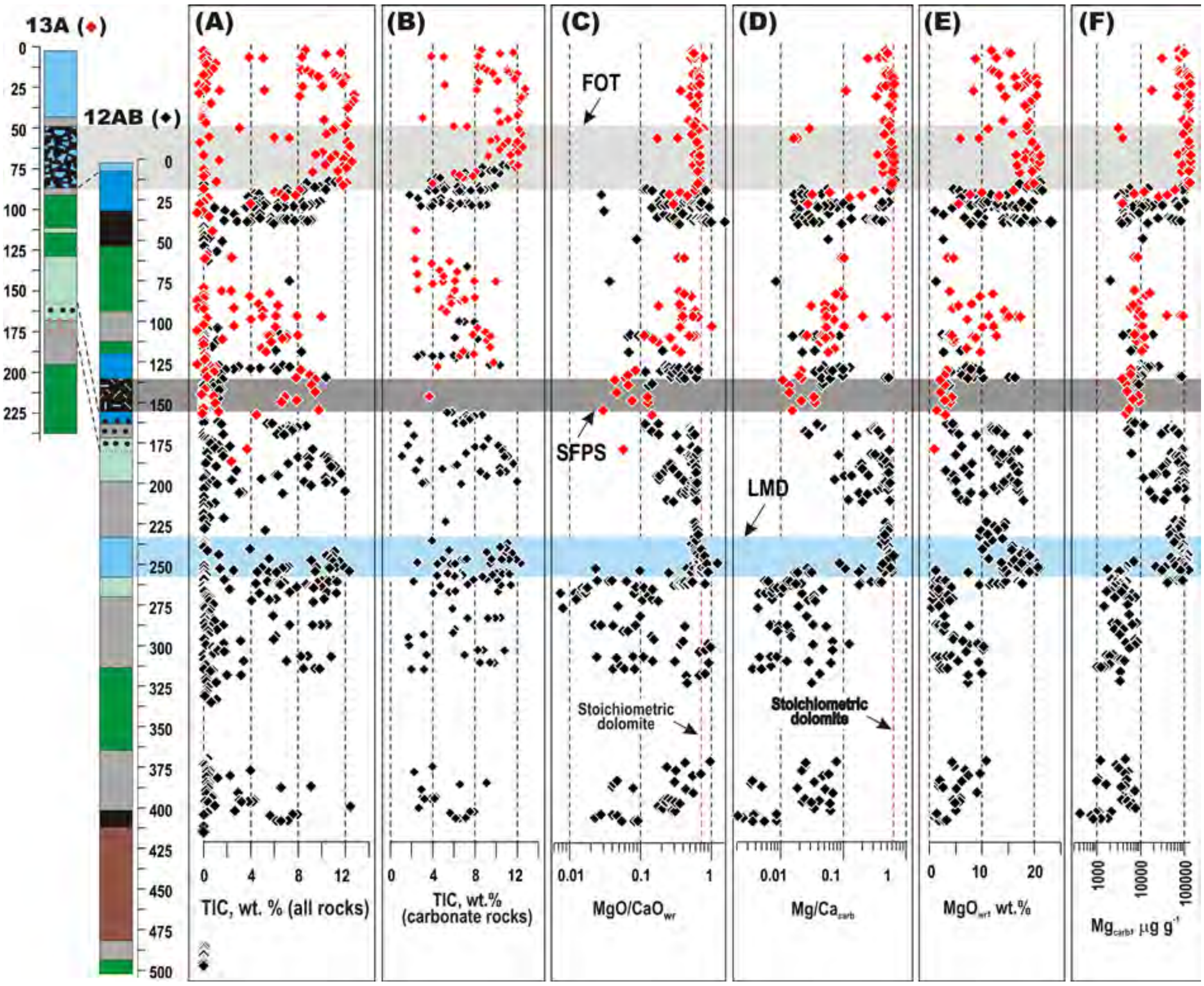
13A (◆)
12AB (◆)
(A)
(B)
(C)
(D)
(E)
(F)
FOT
SFPS
LMD
Stoichiometric dolomite
Stoichiometric dolomite
TIC, wt. % (all rocks)
TIC, wt.% (carbonate rocks)
MgO/CaO$_{wr}$
Mg/Ca$_{carb}$
MgO$_{wr}$, wt.%
Mg$_{carb}$, μg g^{-1}

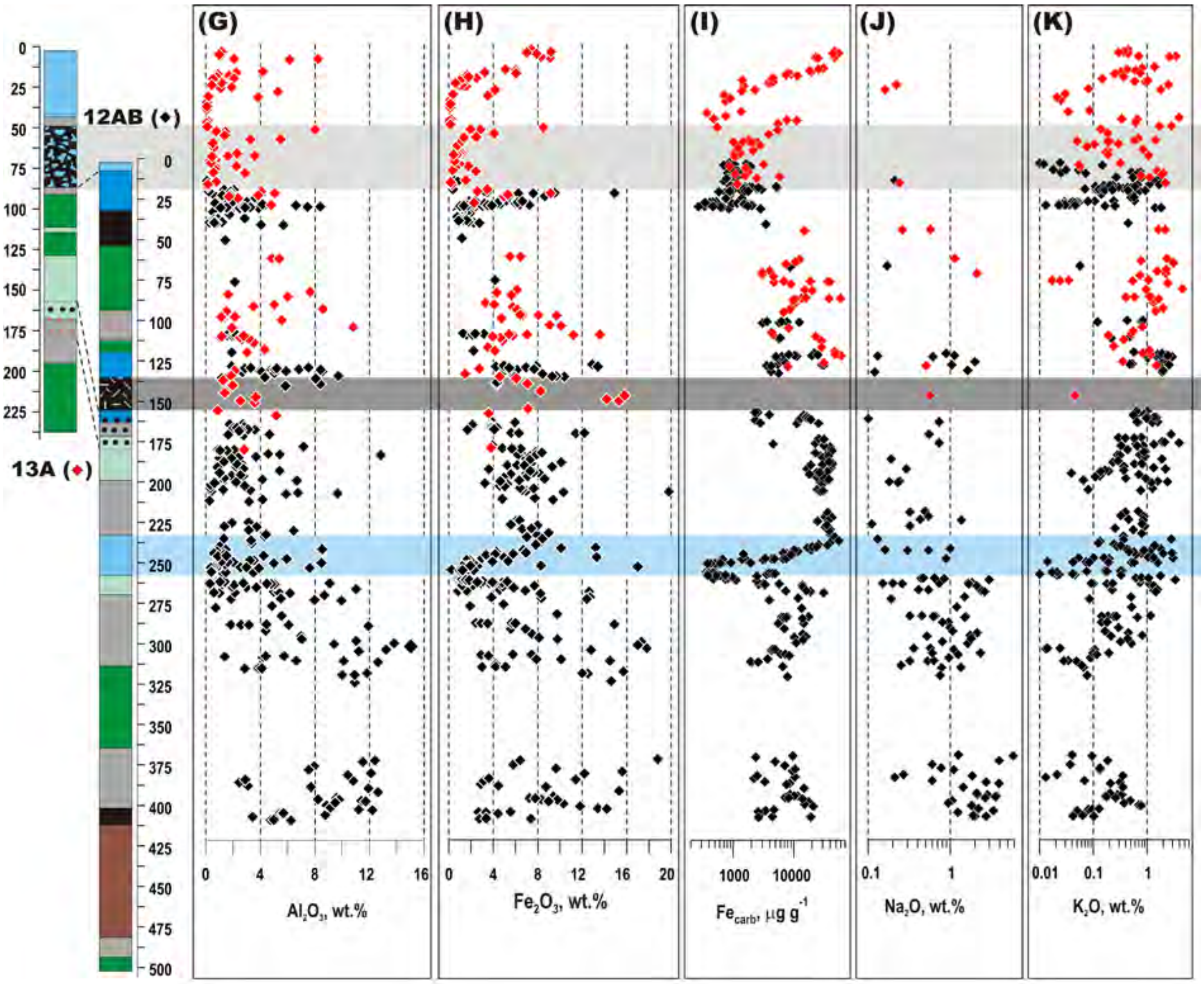
12AB (◆)
13A (◆)
(G)
(H)
(I)
(J)
(K)
Al2O3, wt.%
Fe2O3, wt.%
Fecarb, µg g-1
Na2O, wt.%
K2O, wt.%

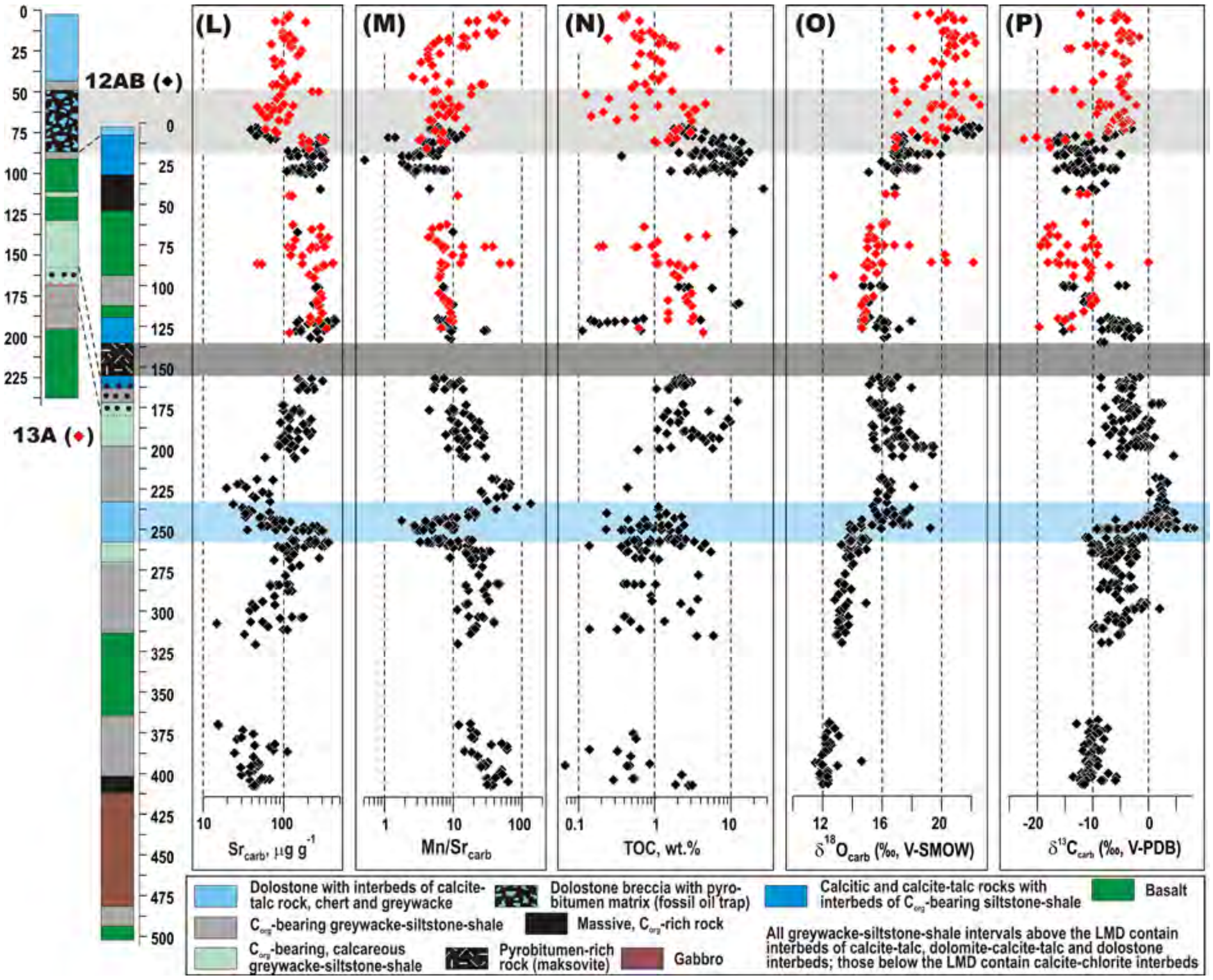

Fig. 10. Geochemical profiles through the ZF based on FAR-DEEP holes 12AB and 13A. Major and trace element data, $\delta^{13}C_{carb}$ and $\delta^{18}O_{carb}$ are from http://far-deep.icdp-online.org (FAR-DEEP), Kump et al. (2011) and Črne et al. (2014). The published data are specified in Appendices A–C. Note that at the depth of the lowermost dolostone bed (LMD) there are significant changes in K_2O and Na_2O abundances, as well as in $\delta^{13}C_{carb}$, Mg/Ca_{carb}, ratios and other geochemical parameters. A cut-off > 1 wt.% total inorganic carbon (TIC) defines the boundary between non-carbonate and carbonate bearing rocks.

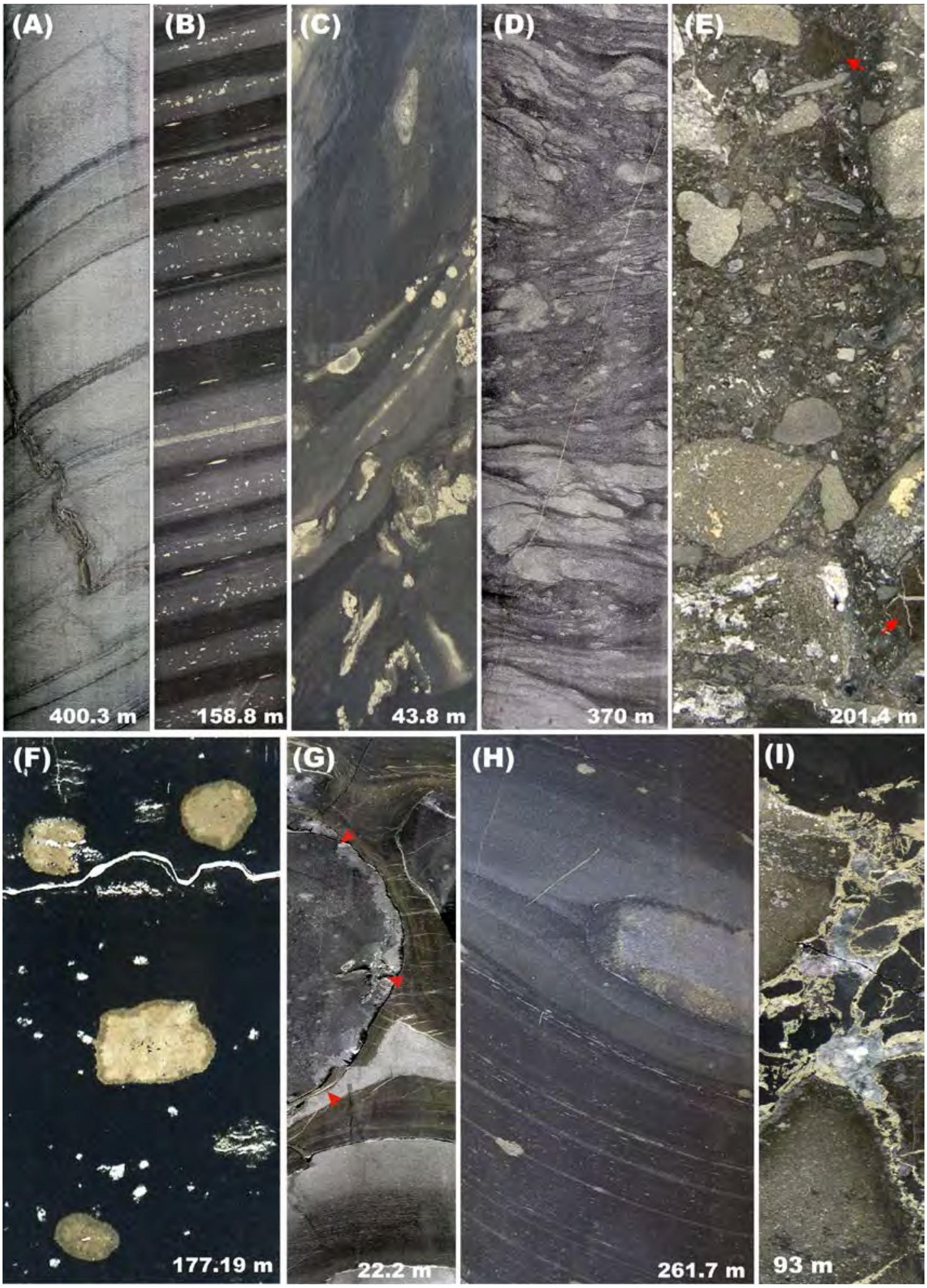

Fig. 11. Main rock types and diagenetic concretions of the ZF. Core diameter is 5 cm. (A) Sandy limestone (pale grey) alternating with thin, dark grey mudstone units intersected by thin vein filled with pyrobitumen and sulphide. (B) Rhythmically interbedded greywacke and mudstone with abundant sulphides (pale yellow). (C) Slumped, sandy limestone with syn-sedimentary deformation, dismembered pyritised layers and sulphide nodules. (D) Slumped bed composed of soft-sediment

deformed and dismembered beds of calcareous greywacke and black mudstone. (E) Explosive breccia containing various unsorted, angular to rounded clasts from a few mm to more than 10 cm in size; clasts are greywacke and sandy limestone (grey), mudstone (black) and pyrobitumen (red arrowed) floating within a mudstone matrix. (F) Zoned, pyrite-pyrrhotite concretion in a black, massive, organic-rich mudstone. (G) A dark grey, chert nodule (red arrowed) in interbedded sandy limestone (bright) and laminated, dark-coloured, C_{org}-rich mudstone. (H) A calcite concretion in laminated greywacke-mudstone. (I) Peperite composed of fragments of mafic lava flow (brownish-grey) and organic rich mud (black) both with sulphidised margins; joints are filled with calcite.

Photographs (A), (D–F), (G) and (H) are from Core 12AB; (B), (C), and (I) from Core 13A. Photographs (A–E) and (G) are reproduced with kind permission of Springer Science+Business Media from Črne, A.E., Melezhik, V.A., Prave, A.R., Lepland, A., Romashkin, A.E., Rychanchik, D.V. Hanski, E.J., Luo, Zh-Yu. (2013). 3.3.3. Zaonega Formation: FAR-DEEP Holes 12A and 12B, and neighbouring quarries, and photograph (I) from 3.3.4. Črne, A.E., Melezhik, V.A., Prave, A.R., Lepland, A., Romashkin, A.E., Rychanchik, D.V. Hanski, E.J., Luo, Zh-Yu. (2013). 3.3.4. Zaonega Formation: FAR-DEEP Hole 13A In: Melezhik, V.A., Prave, A.R., Fallick, A.E., Hanski, E.J., Lepland, A., Kump, L.R., Strauss, H. (eds.) Reading the Archive of Earth's Oxygenation. Volume 2: The Core Archive of the Fennoscandian Arctic Russia - Drilling Early Earth Project. Series: Frontiers in Earth Sciences. Springer, Heidelberg, pp. 946–1007 and 1008–1046, respectively. Copyright Springer Science+Business Media 2013.

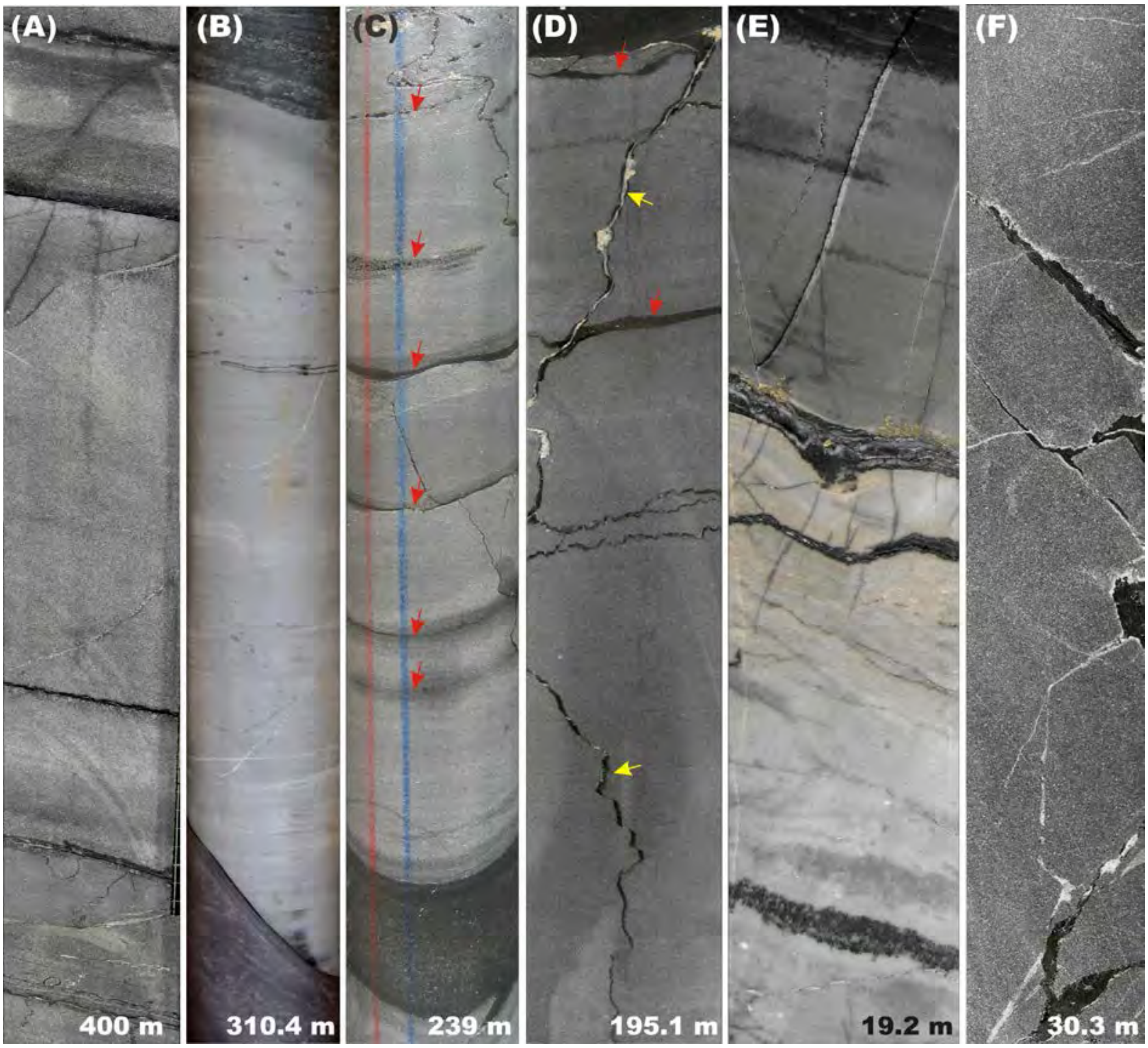

Fig. 12. Carbonate rocks of the ZF. (A) Sandy 'limestone' (pale grey) alternating with thin, black mudstone units. (B) A greywacke-hosted limestone lens composed of redeposited ooids (for details see, Fig. 13E) (C) Beds of grey, massive, sandy dolostone with dark-coloured mudstone drapes. (D) Beds of grey dolostone with mudstone drapes (red arrowed) cross-cut by pyrobitumen veinlets (yellow arrowed). (E) Pale grey dolostone with black, silicified mudstone drapes and mudstone top. (F) Massive dolostone with cracks filled by pyrobitumen (black) and calcite (white).

Photographs (A–D) are from Core 12AB; (E–F) – from Core 13A. Photographs reproduced with kind permission of Springer Science+Business Media from Črne, A.E., Melezhik, V.A., Prave, A.R., Lepland, A., Romashkin, A.E., Rychanchik, D.V. Hanski, E.J., Luo, Zh-Yu. (2013). 3.3.3. Zaonega Formation: FAR-DEEP Holes 12A and 12B, and neighbouring quarries, and. 3.3.4. Zaonega Formation: FAR-DEEP Hole 13A In: Melezhik, V.A., Prave, A.R., Fallick, A.E., Hanski, E.J., Lepland, A., Kump, L.R., Strauss, H. (eds.) Reading the Archive of Earth's Oxygenation. Volume 2: The Core Archive of the Fennoscandian Arctic Russia - Drilling Early Earth Project. Series: Frontiers in Earth Sciences. Springer, Heidelberg, pp. 946–1007 and 1008–1046, respectively. Copyright Springer Science+Business Media 2013.

1613

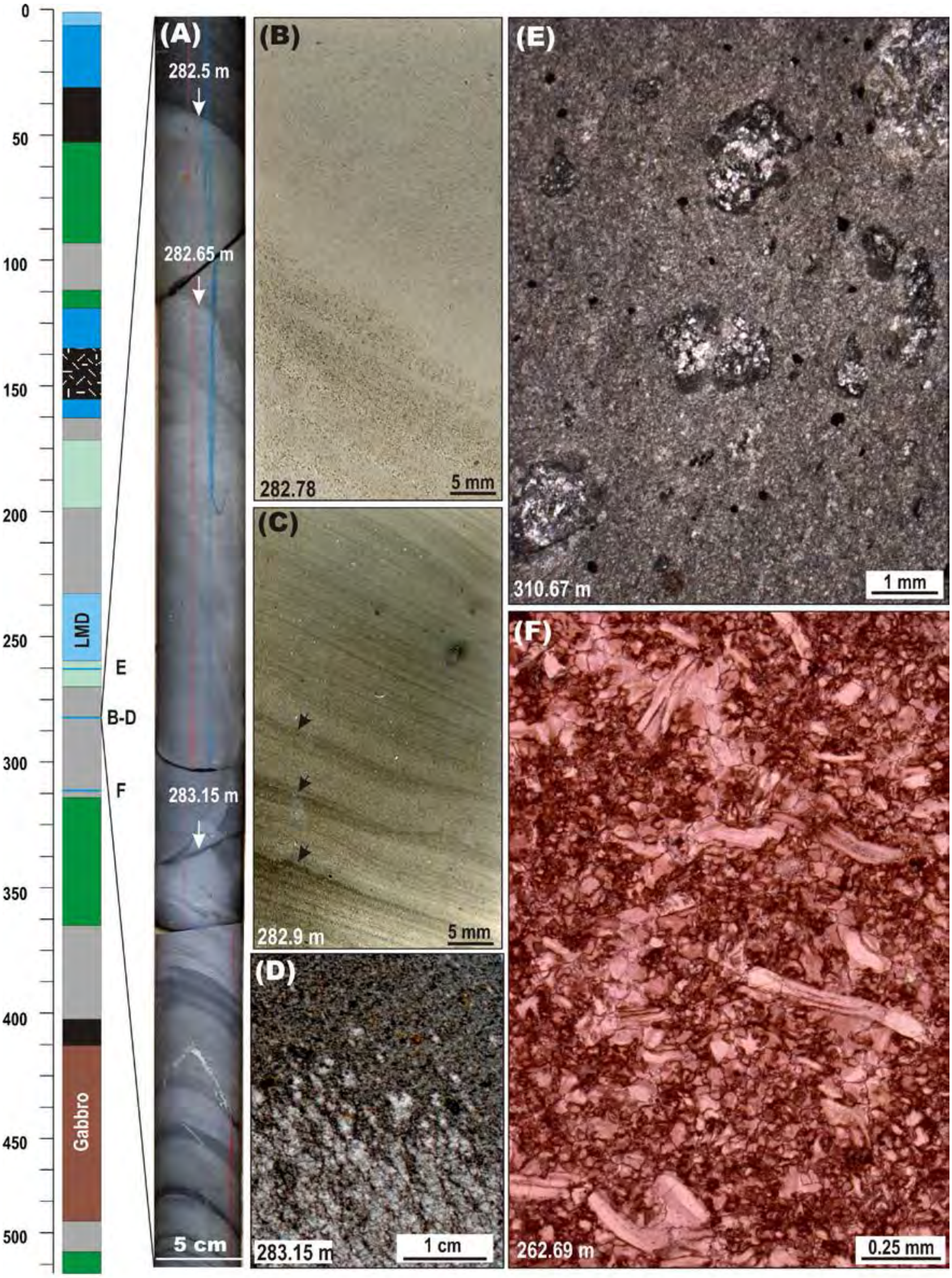

0
50
100
150
200
250
300
350
400
450
500
LMD
Gabbro
E
B-D
F
(A)
282.5 m
282.65 m
283.15 m
5 cm
(B)
282.78
5 mm
(C)
282.9 m
5 mm
(D)
283.15 m
1 cm
(E)
310.67 m
1 mm
(F)
262.69 m
0.25 mm

Fig. 13. Sedimentological and petrographic features of calcitic rocks from Core 12AB below 258 m. (A) Unsawn core illustrating a calcitic bed showing sharp contacts with host greywackes (283.1 and 282.5 m), a faint bedding and an internal erosional surface enhanced by diagenetic recrystallisation (282.65 m). (B) Indistinctly bedded calcitic rock passing into a massive variety. (C) Thinly laminated calcitic rock starting with three thicker cycles each draped with mud-rich layers (arrowed). (D) A probable clastic limestone (calcarenite) showing rapid upward grading. Clasts are recrystallised, and matrix is composed of calcite grains intergrown into a xenomorphic mass which contains biotite and albite. (E) A mass of xenomorphic calcite containing rounded clasts or intraclasts composed of sparry calcite ± quartz. (F) A calcitic rock composed of unsorted, angular, platy fragments of laminated limestone. (B), (C) and (D) - scanned thin sections; (F) - photomicrograph of Alizarin-red-stained thin section in non-polarised, transmitted light.

1626

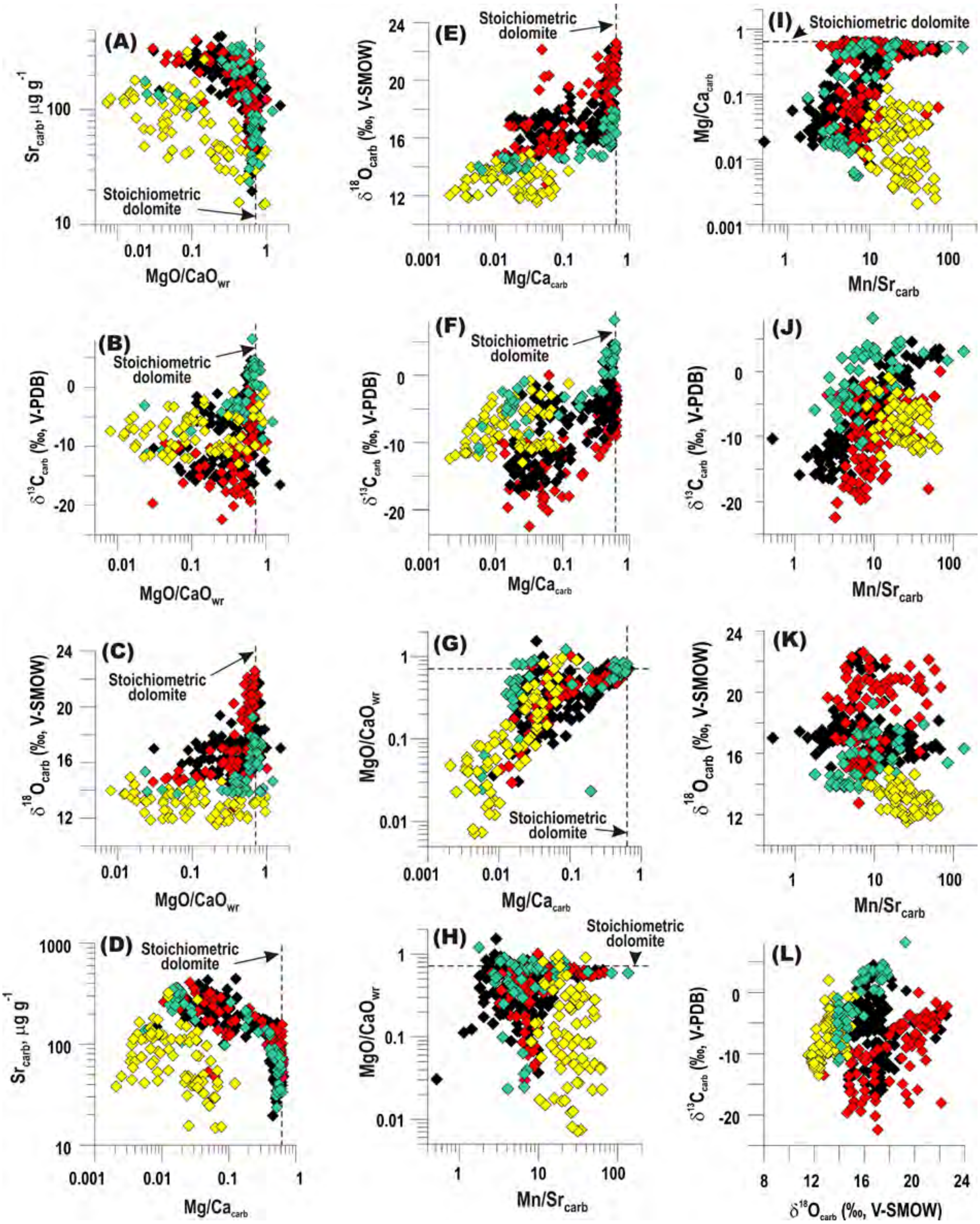
(A)
Stoichiometric dolomite
Sr_{carb}, µg g^{-1}
MgO/CaO$_{wr}$
(B)
Stoichiometric dolomite
$\delta^{13}C_{carb}$ (‰, V-PDB)
MgO/CaO$_{wr}$
(C)
Stoichiometric dolomite
$\delta^{18}O_{carb}$ (‰, V-SMOW)
MgO/CaO$_{wr}$
(D)
Stoichiometric dolomite
Sr_{carb}, µg g^{-1}
Mg/Ca$_{carb}$
(E)
Stoichiometric dolomite
$\delta^{18}O_{carb}$ (‰, V-SMOW)
Mg/Ca$_{carb}$
(F)
Stoichiometric dolomite
$\delta^{13}C_{carb}$ (‰, V-PDB)
Mg/Ca$_{carb}$
(G)
Stoichiometric dolomite
MgO/CaO$_{wr}$
Mg/Ca$_{carb}$
(H)
Stoichiometric dolomite
MgO/CaO$_{wr}$
Mn/Sr$_{carb}$
(I)
Stoichiometric dolomite
Mg/Ca$_{carb}$
Mn/Sr$_{carb}$
(J)
$\delta^{13}C_{carb}$ (‰, V-PDB)
Mn/Sr$_{carb}$
(K)
$\delta^{18}O_{carb}$ (‰, V-SMOW)
Mn/Sr$_{carb}$
(L)
$\delta^{13}C_{carb}$ (‰, V-PDB)
$\delta^{18}O_{carb}$ (‰, V-SMOW)

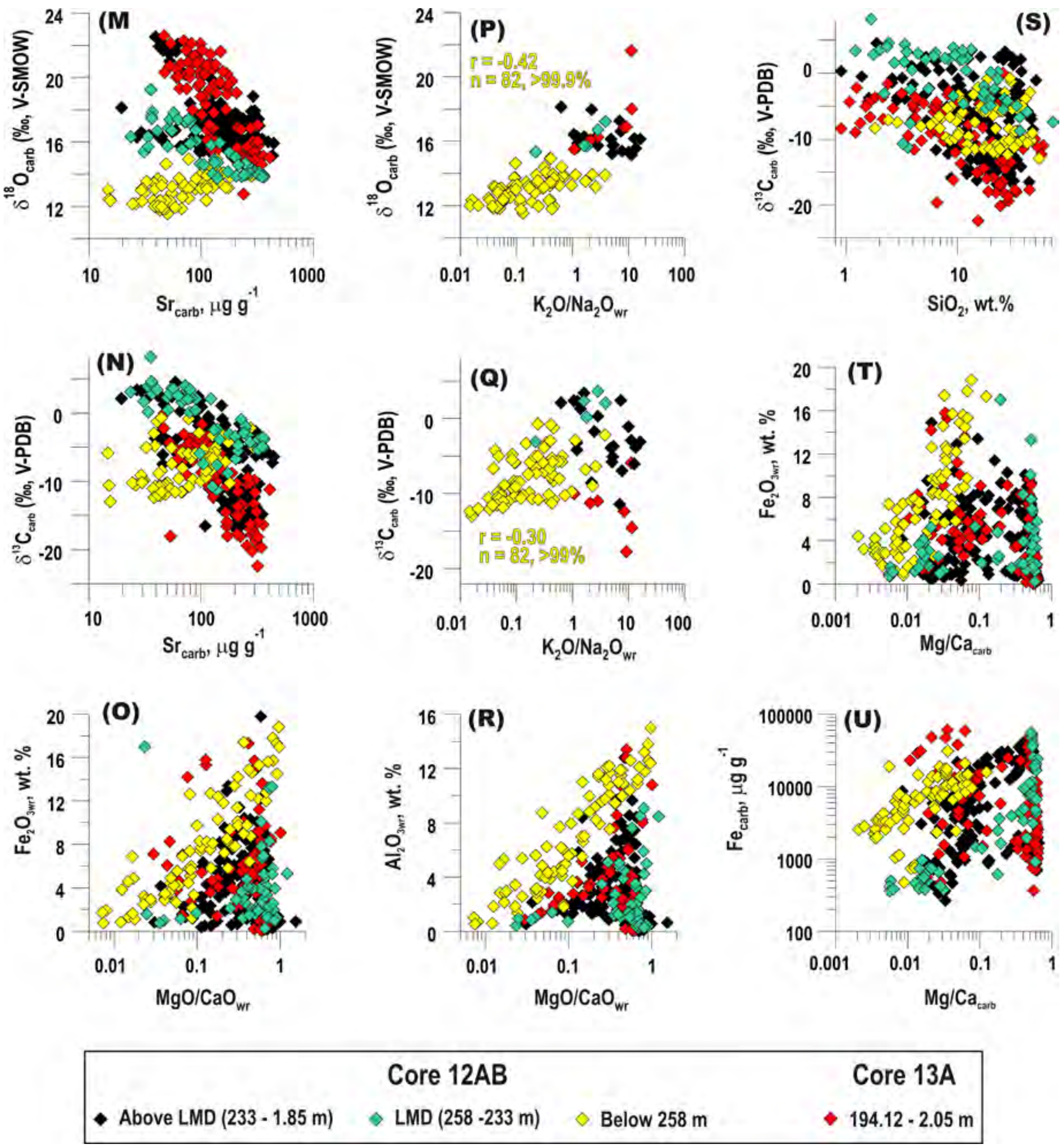

Fig. 14. Various cross-plots illustrating geochemical features and apparent post-depositional geochemical and isotopic trends in the ZF carbonate rocks from different depth intervals. The diagrams are based on data from FAR-DEEP database (http://far-deep.icdp-online.org) and data published by Kump et al. (2011) and Črne et al. (2014). The published data are specified in Appendices A–C.

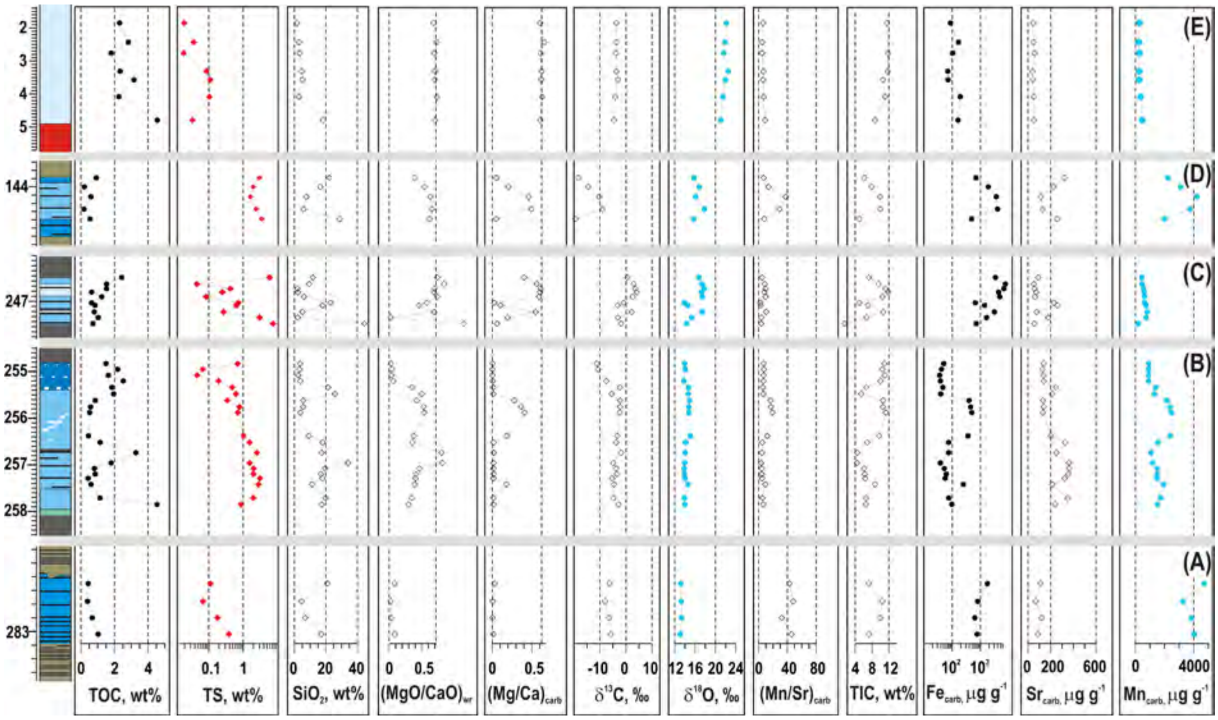

Fig. 15. Major geochemical features of carbonate rocks documented through the stratigraphy in Core 12AB and 13A. (A) A calcitic bed occurring below 258 m (for petrographic and sedimentological characteristics, see Fig. 13). Both MgO/CaO_{wr} and Mg/Ca_{carb} ratios suggest calcitic mineralogy. There are no through-bed chemical and isotopic variations. (B) An example of carbonate rock from the lowermost part of the LMD. This is characterised by a mixed dolomite ± calcite + talc composition (for petrographic and sedimentological characteristics, see Fig. 17) associated with the calcitisation of dolostones through dolomite-quartz reaction. There are through-bed chemical variations. (C) An example of carbonate rock from the middle part of the LMD. This is characterised by mixed dolomite ± calcite + talc composition with the presence of pure dolostone intervals. There are "through-bed" chemical and isotopic variations. (D) An example of chemically and isotopically zoned carbonate bed from the middle part of the LMD. This is characterised by mixed dolomite ± calcite + talc composition with the presence of pure dolostone interval in the core of the bed (for petrographic and sedimentological characteristics, see Fig. 16). (E) An example of pure dolostone from Core 12AB (for petrographic and sedimentological characteristics, see Fig. 20). The dolostone contains a substantial amount of TOC. There are no through-bed chemical and isotopic variations, $\delta^{13}C_{carb}$ stays significantly below zero but a low Mn/Sr_{carb} (5–9) suggests no obvious post-depositional alteration.

The diagrams are based on data from FAR-DEEP database (http://far-deep.icdp-online.org) and data reported in Kump et al. (2011) and Črne et al. (2013). The published data are specified in Appendices A–C.

Legend: dark blue – calcitic rocks; pale blue – calcitised dolostone; light blue – dolostone; green – calcareous greywacke; pale brown – greywacke; dark grey – mudstone; red – chert; dots – graded bedding; stripes – parallel bedding, otherwise – massive.

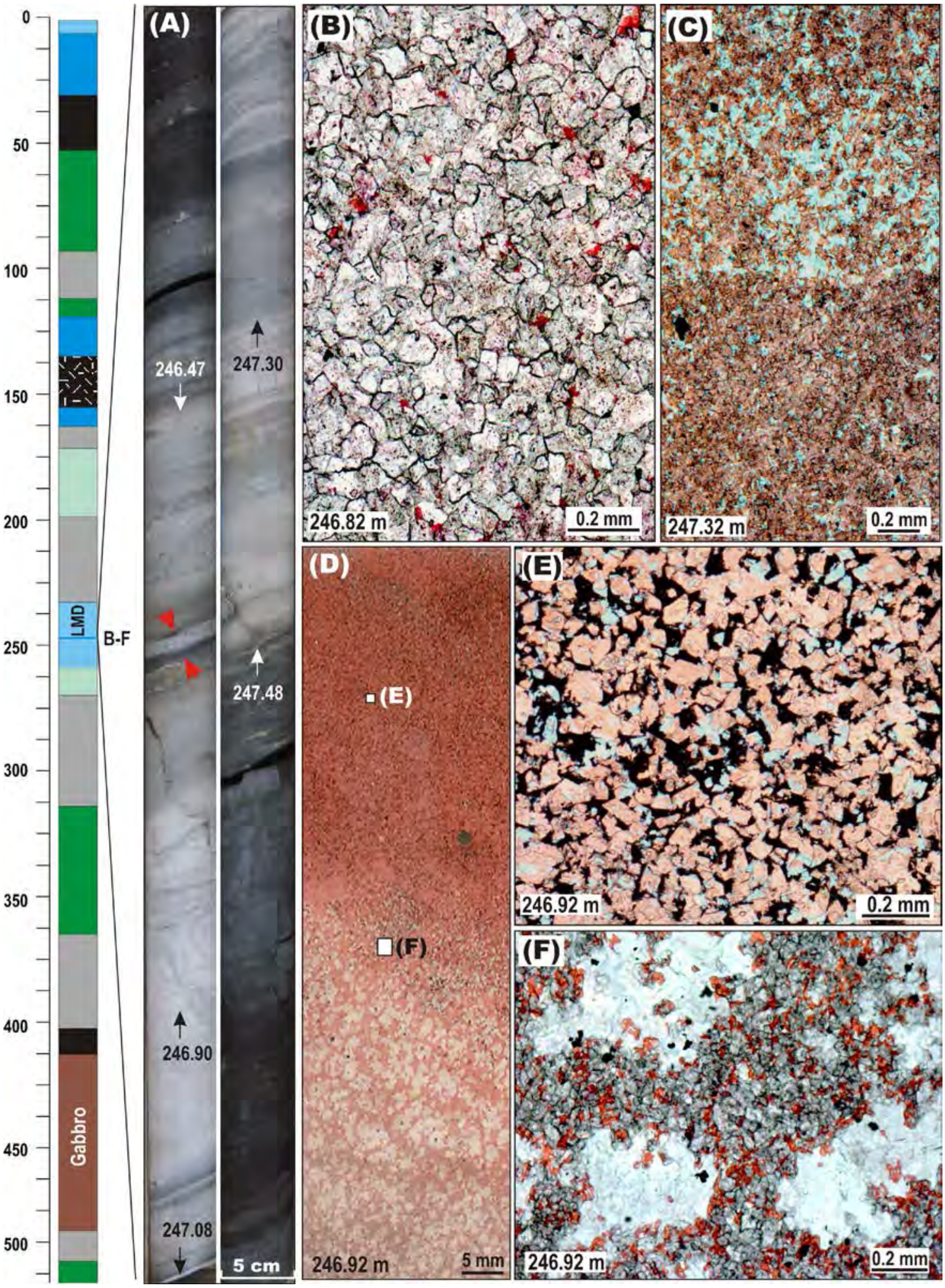

Fig. 16. Sedimentological and petrographic features of carbonate rocks with dolomite + calcite + talc paragenesis from chemically and isotopically zoned carbonate bed representing the middle part of the LMD. (A) Unsawn core illustrating alternating dolostone (247.30–247.08 and 246.90–246.47) and calcite-talc rock. Both, the dolostone and calcite-talc intervals show irregular parallel bedding. The

uppermost dolostone and the lowermost calcite-talc interval have sharp contacts with hosting greywackes. Contacts between dolostone and calcite-talc intervals are either diffuse or well-pronounced. Some dolostone intervals have thin talc-calcite intervals (e.g., red arrowed). (B) Dolostone composed of tightly packed sub-euhedral dolomite crystals partially replaced by calcite (pink), and separated by thin film of organic matter (black). (C) Calcite (pink)-talc (pale blue) rock in sharp contact with overlying interval enriched in talc (white). (D) Calcite (pink)-talc (pale blue) rock gradually passing upward into calcitic rock. (E) Detailed view of the calcitic rock composed of minor talc (white) and euhedral, rhomboidal, dolomite crystals replaced by calcite (pink) embedded into organic-rich matrix (black). (F) Detailed view of calcite-talc rock composed of large porphyroblasts of talc (white), tightly packed, euhedral, rhomboidal, dolomite crystals (pale grey) partially replaced by calcite (pink). (B–F) - photomicrographs of Alizarin-red-stained thin sections in non-polarised, transmitted light.

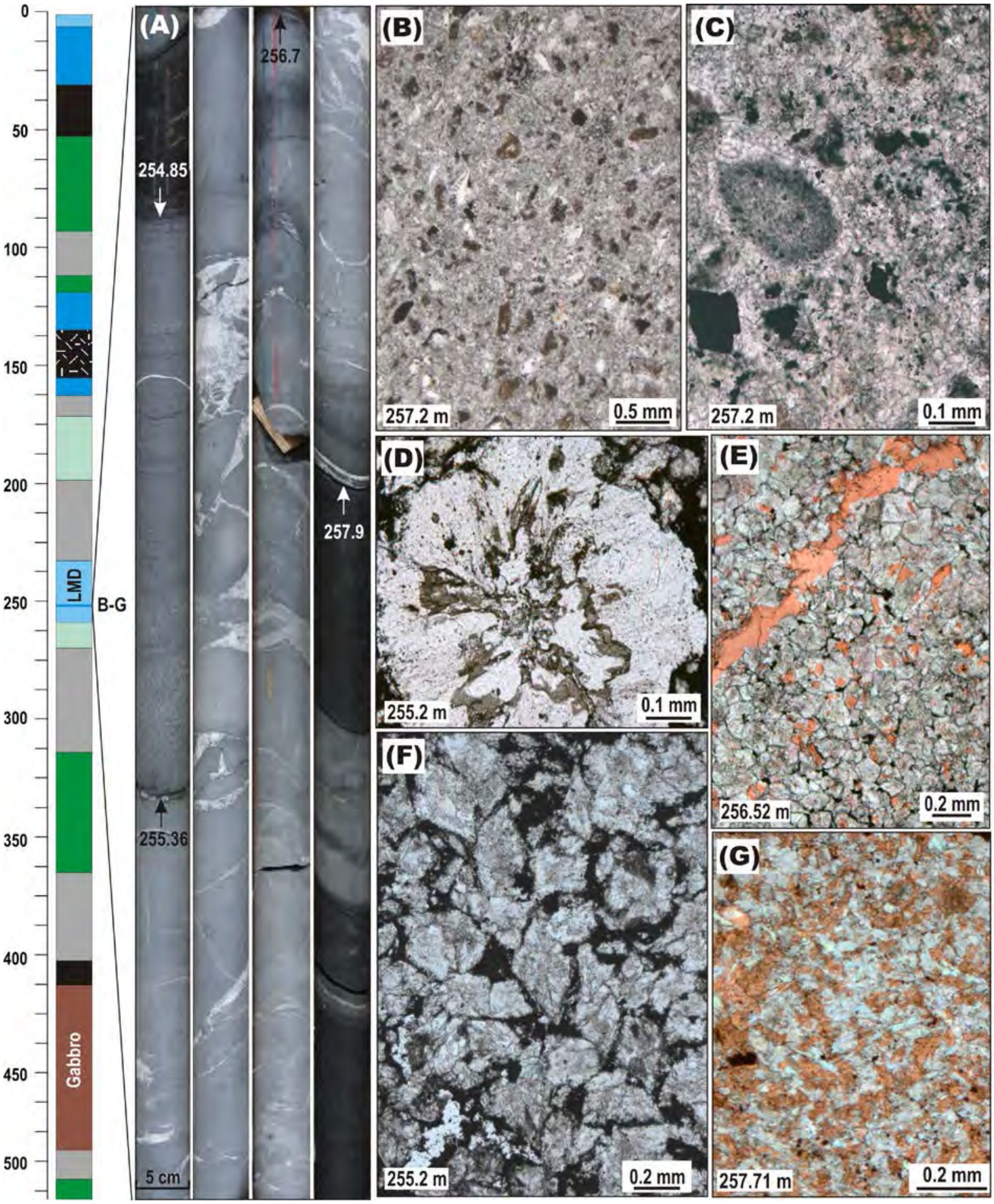

Fig. 17. Sedimentological and petrographic features of carbonate rocks with dolomite + calcite + talc paragenesis representing the middle part of the LMD. (A) Unsawn core illustrating carbonate beds having sharp contact with hosting black, C_{org}-rich greywackes. The beds are composed of calcite and dolomite occurring in variable proportions. The upper bed (255.36 to 254.85 m) shows a granular texture grading upward from c. millimetre size to finer grains, the middle bed (256.7 to 255.36 m) is massive, whereas the lower bed exhibits indistinct layering. The two lower beds contain abundant

cracks filled with white calcite. (B) Clastic carbonate rocks comprising the base of the lower bed. White, grey and brown intraclasts are mainly pervasively calcitised dolomite (MgO/CaO_{wr} = 0.41, Mg/Ca_{carb} = 0.02) with minor fragments of partially sulphidised, organic-rich substance (black). (C) Details of rounded, calcitised intraclasts of micritic dolomite; black mineral is pyrite. (D) Radial structure in possible recrystallised ooid from the base of the upper carbonate bed. (E) Stained (with Alizarin-red) section illustrating partially calcitised (pink) dolomite grains cross-cut by calcite vein (pink). (F) Euhedral crystals of intensely calcitised dolomite embedded in organic-rich matrix. (G) Stained (with Alizarin-red) section of talc (white)-calcite (pink) rock where talc-calcite paragenesis was formed through the dolomite-quartz reaction. (B–G) - photomicrographs of thin sections in non-polarised, transmitted light.

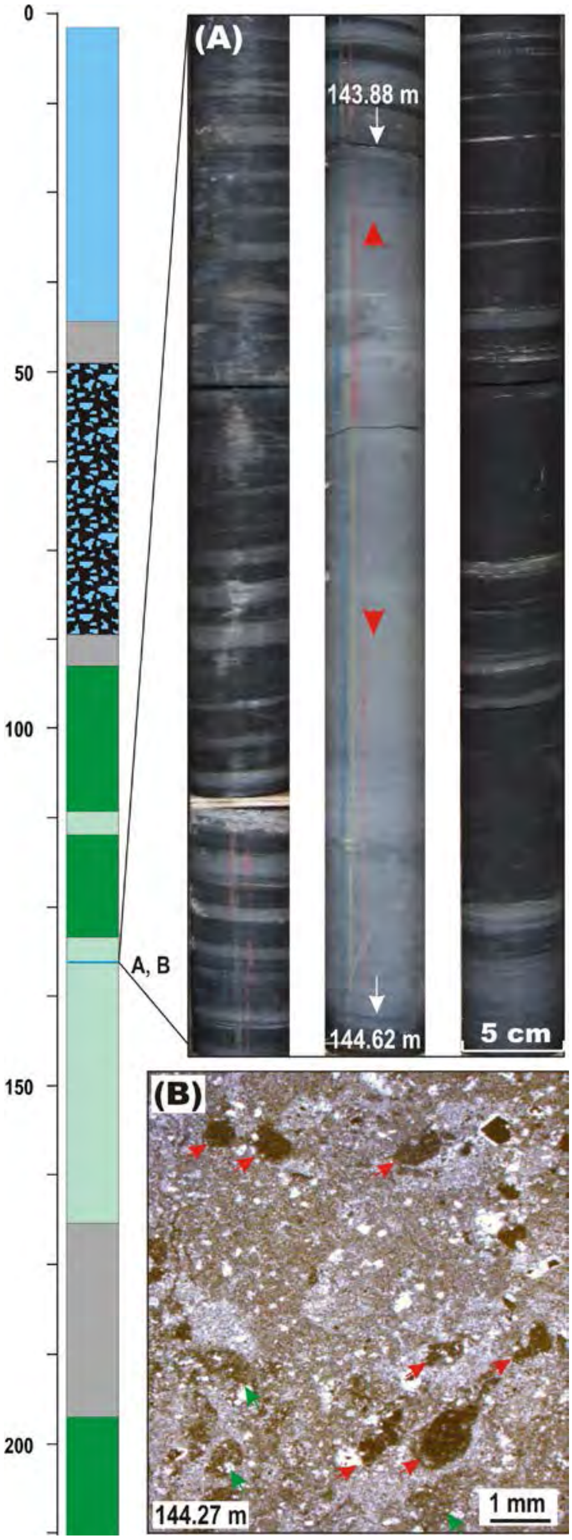

Fig. 18. Sedimentological and petrographic features of carbonate rocks with dolomite + calcite + talc paragenesis from chemically and isotopically zoned carbonate bed representing the middle part of Core 13A. (A) Unsawn core showing a rather massive carbonate bed having sharp contacts (white arrows) with hosting organic-rich, bedded greywacke. The bed has intensely calcitised margins (marked by red arrows) and less calcitised dolomitic core. (B) Calcitised dolostone composed of

rounded intraclasts of micritic (dark grey, red arrows) and microsparitic (grey, green arrows) dolostone embedded in unevenly recrystallised carbonate matrix. Photomicrograph in non-polarised, transmitted light.

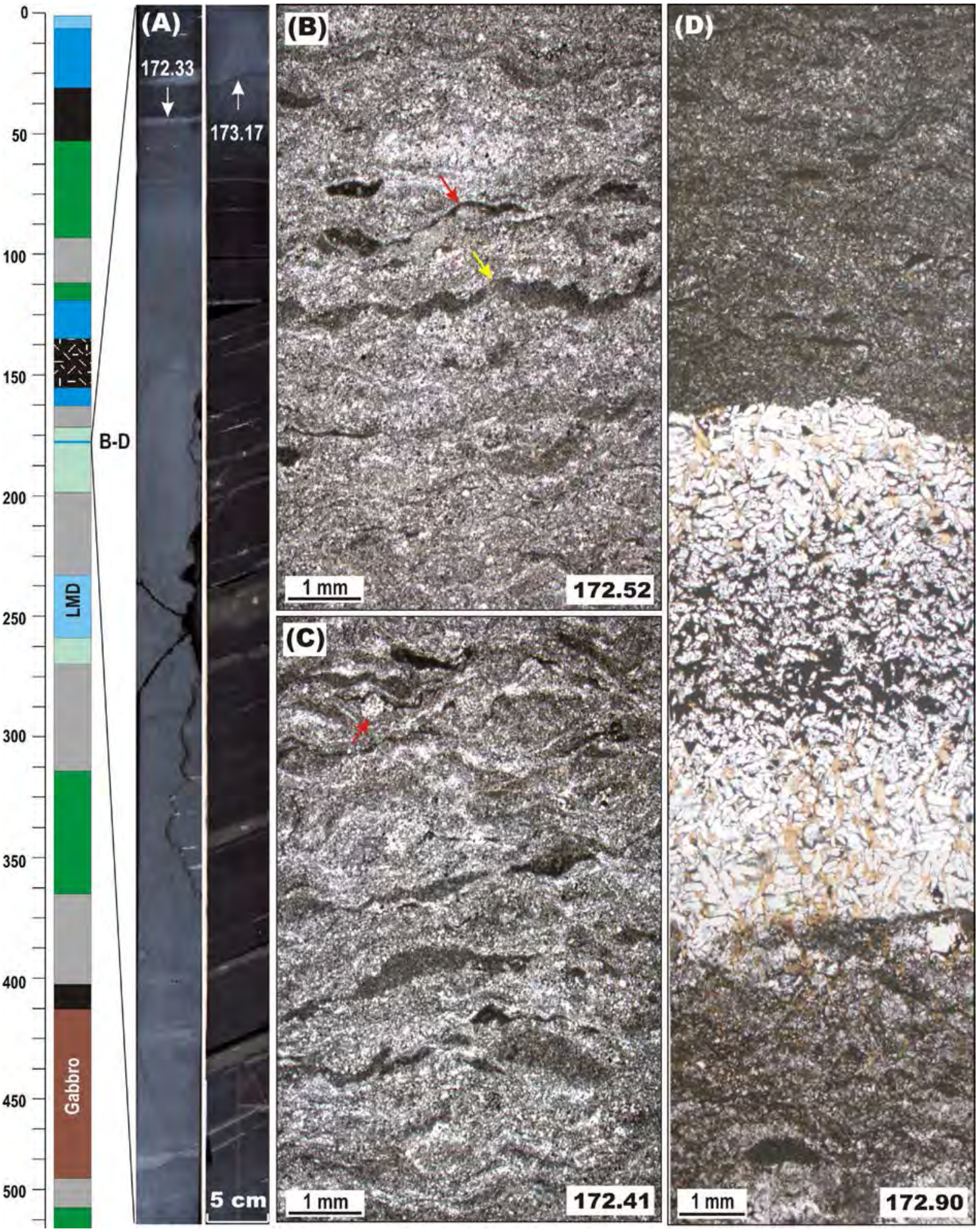

Fig. 19. Sedimentological and petrographic features of partially calcitised dolostone with microbial fabrics. (A) Sawn core of the dolostone bed hosted by organic-rich greywacke. (B) Microbial fabric expressed by wrinkled and buckled laminae of dark grey dolomicrite in a dolospar matrix. Note that some micritic lamina show a large lateral extent (yellow arrow), whereas others do not. Some lamina drape uneven palaeorelief (red arrow). (C) Microbial fabrics are expressed by wrinkled and buckled laminae of dark grey dolomicrite in a dolospar matrix with a clotted microstructure. Note the presence of clast draped by micritic lamina (red arrow). (D) A white dolomite band within dark grey dolostone with microbial fabrics. The white band is composed of large, tightly-packed, randomly-oriented, rod-shaped, dolomite crystals partially replaced by pyrite (black).

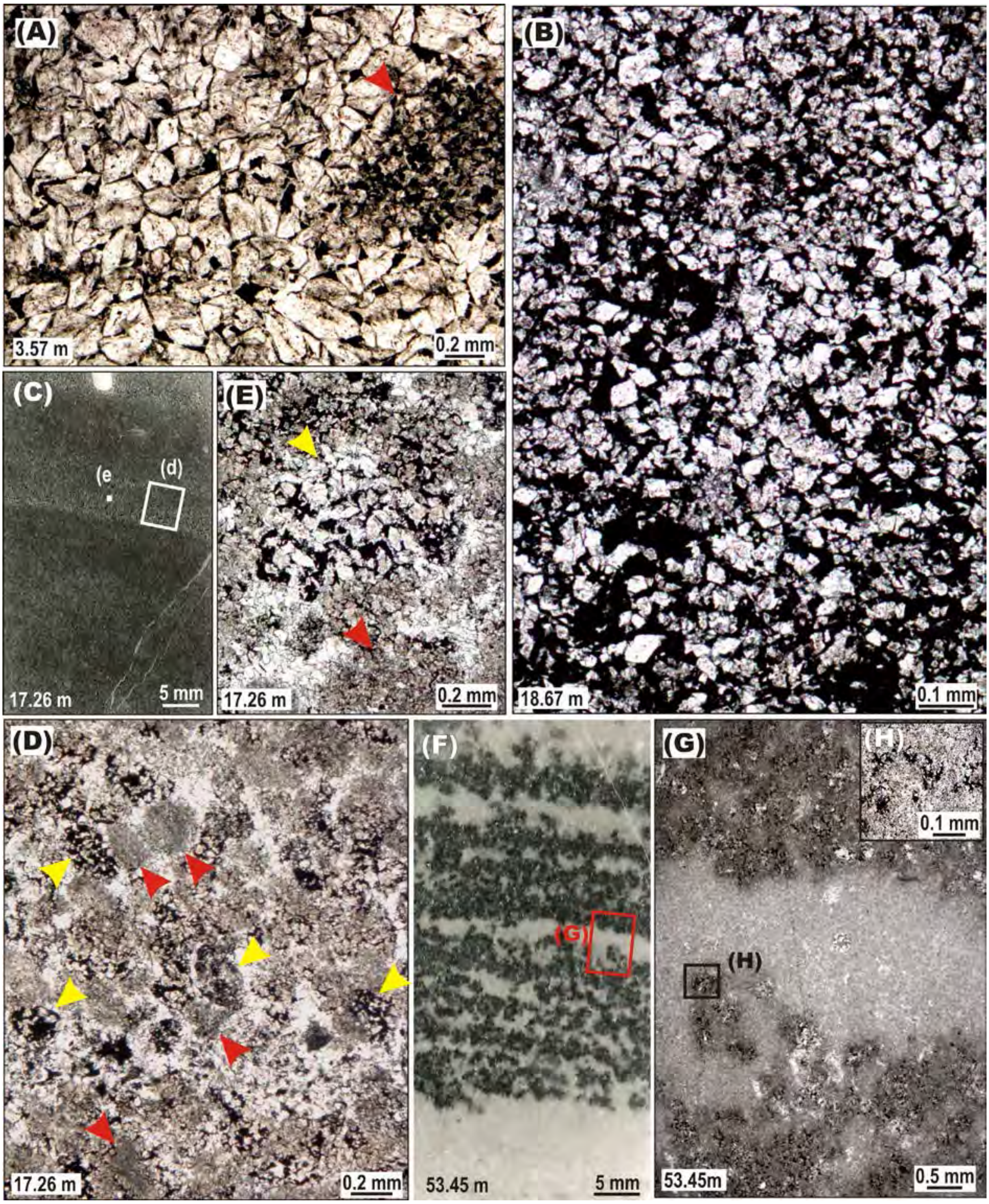

Fig. 20. Sedimentological and petrographic features of pure dolostone from uppermost part of Core 12AB. (A) Massive dolostone composed of tightly-packed euhedral dolomite crystals separated by thin films of organic-rich material. Note rounded particle of fine-grained dolostone enriched in organic matter (red arrowed) which may represent either an intraclast or a relict of a less recrystallised precursor. (B) Organic-rich dolostone composed of euhedral crystals embedded into black, organic-

rich material. (C) Bedded dolostone where the bedding is expressed by an alternation of darker and lighter layers; the base of layers shows clastic microtexture (see D and E). (D and E) Clastic dolostone (dolarenite) where clasts are rounded and composed of either small, euhedral, dolomite crystals (yellow arrowed) embedded into organic rich matrix or microsparitic dolomite (red arrowed); white in (D) is recrystallised dolomite matrix. (F) Bedded dolostone where bedding is expressed by alternation of layers composed of white, microcrystalline dolomite and those containing patches of black, organic-rich material fringed by euhedral dolomite crystals. (G) Detailed view of diffuse, irregular contact between layers of white and grey dolomite. (H) Patches of pyrobitumen (black) in the layer of grey dolomite. (I) A patch of coarse crystalline dolomite with black pyrobitumen in grey, microcrystalline dolomite. (J) Microtexture of the grey dolomite is expressed as tightly packed, small, euhedral, dolomite crystals separated by thin films of organic-rich material. (K) Large rhomboids of dolomite crystals with segregation of pyrobitumen (black). A, B, E, D and G - photomicrographs of Alizarin-red-stained thin sections in non-polarised, transmitted light. C, F and I- scanned thin sections. H, J and K – photomicrographs of thin sections in non-polarised, transmitted light.

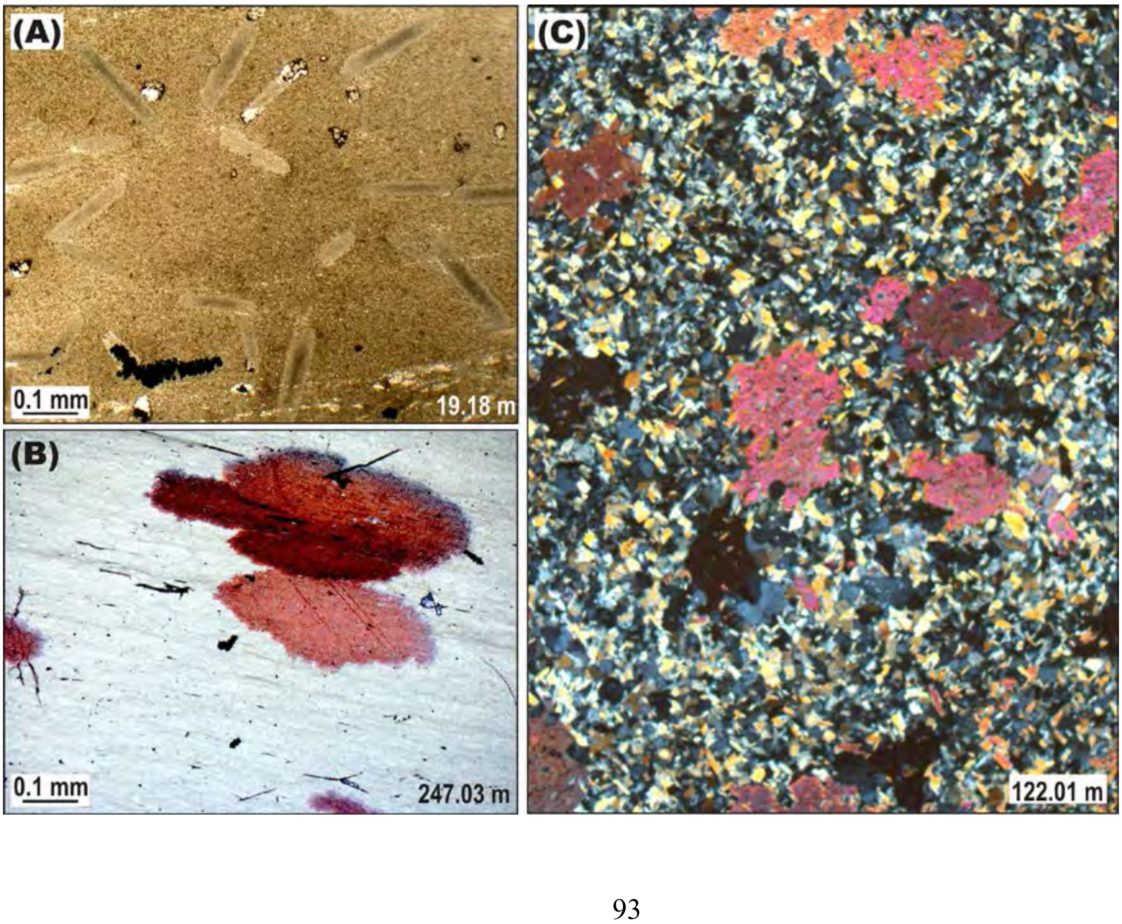

Fig. 21. Post-metamorphic calcite in the ZF. (A) Photomicrograph in non-polarised, transmitted light of replacive, lathlike calcite crystals superimposed on mudstone metamorphic fabrics. (B) Replacive, pancake-like crystals superimposed on mudstone metamorphic fabrics; scanned thin section stained by Alizarin-red. (C) Photomicrograph in polarised, transmitted light of irregular porphyroblasts superimposed on granoblastic/meta-psammitic texture.

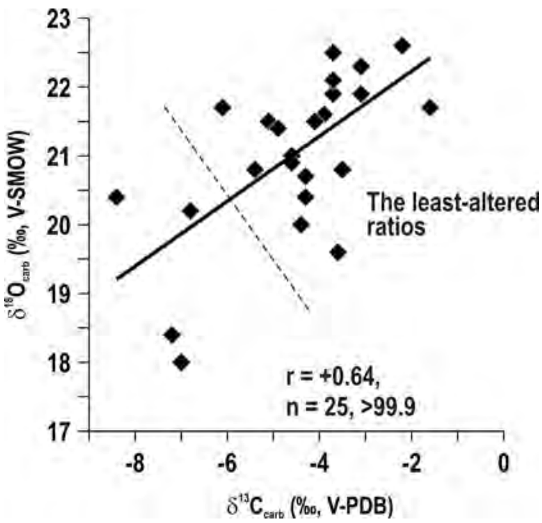

Fig. 22. A $\delta^{13}C_{carb}$-$\delta^{18}O_{carb}$ crossplot for the 25 least-altered dolostone samples (Mn/Sr $\leq$ 10) from the upper part of the ZF. Note a significant positive correlation between these two parameters suggesting an alteration. The dashed line perpendicular to the best-fit line is arbitrarily used here as a further cut-off for screening against possible alteration.

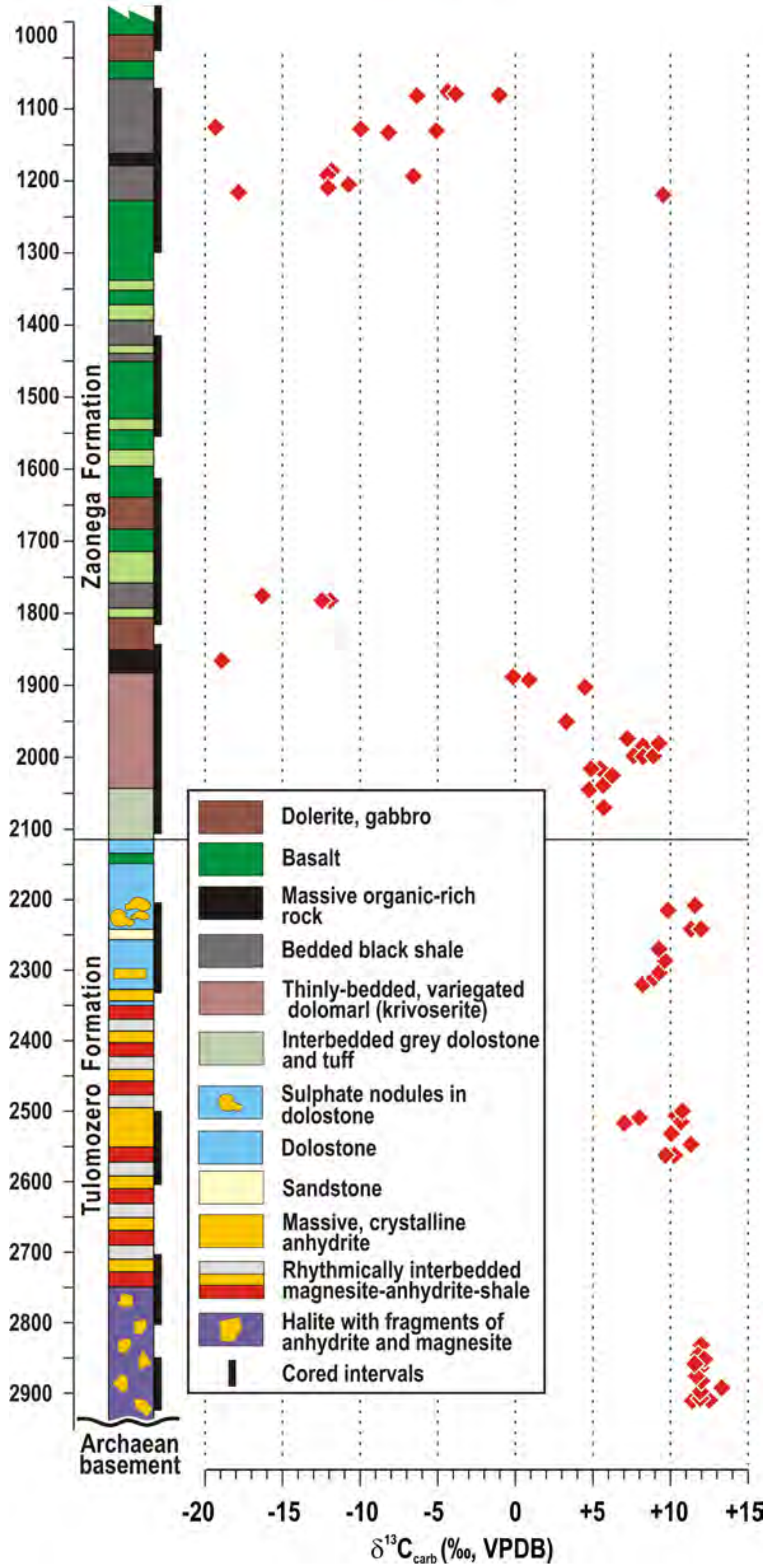

Fig. 23. $\delta^{13}C_{carb}$ profile through the ZF based on OPH core with data from Krupenik et al. (2012b).

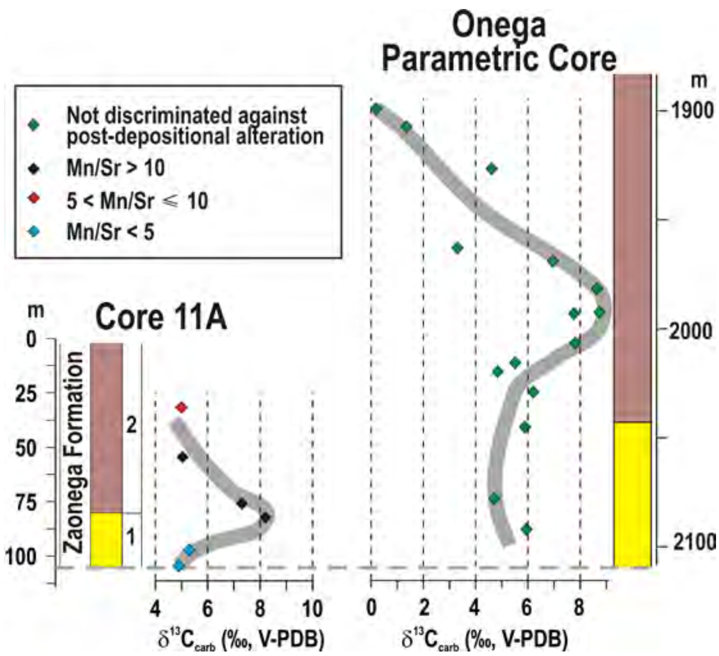

Fig. 24. A positive excursion of $\delta^{13}C_{carb}$ in the lowermost part of the ZF above the contact with the TF (dashed line) as seen in supposedly time-equivalent intervals drilled by Hole 11A (condensed section) and OPH. Note that the published data from OPH (Krupenik et al., 2011b) do not provide trace and major element abundances, hence are not discriminated against post-depositional alteration.

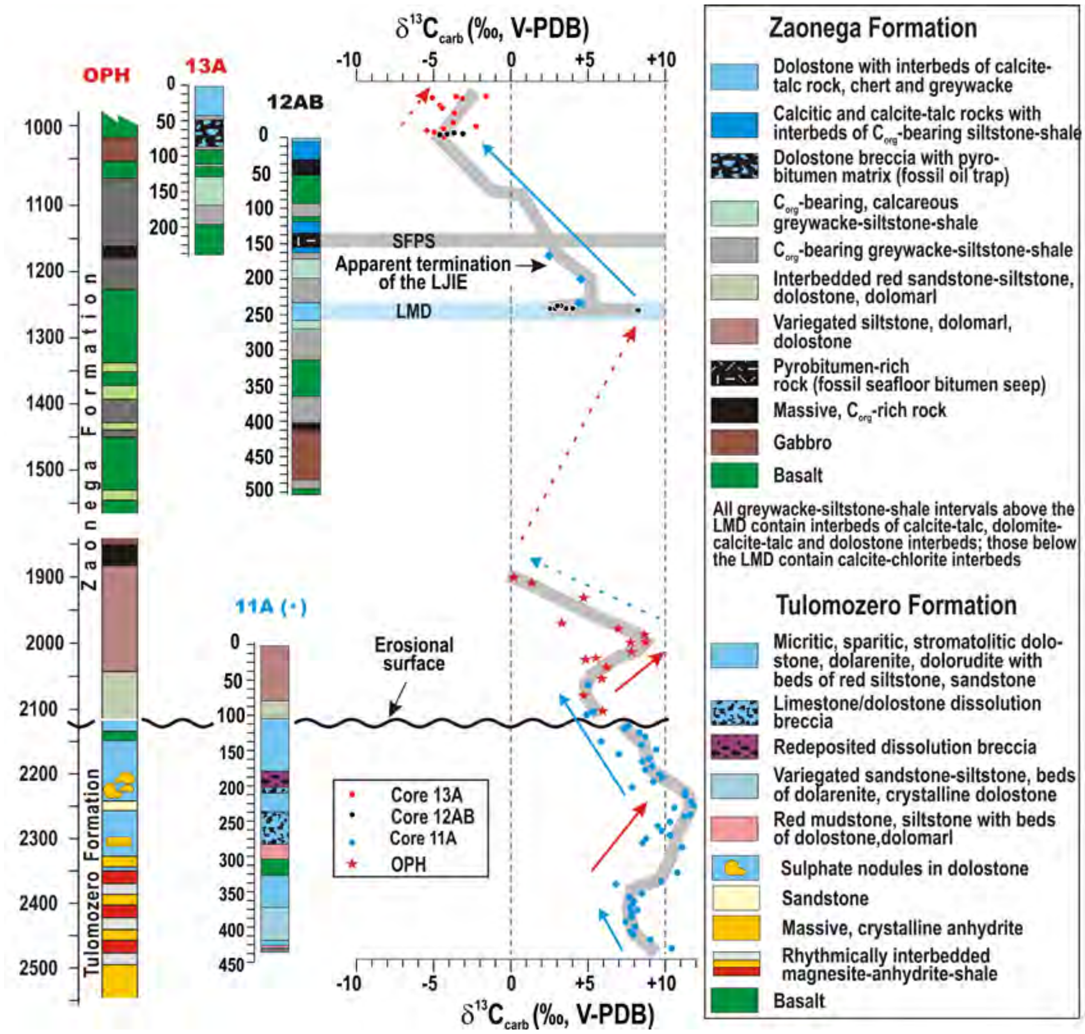

Fig. 25. A stratigraphic profile of the least altered $\delta^{13}C_{carb}$ values obtained from dolomite in Cores 11A, 12AB and 13A. Data from OPH are not discriminated against post-depositional alteration. Blue diamonds represent altered (Mn/Sr > 15–30) but ^{13}C-rich dolostone samples which assist in defining the end of the LJIE. Blue and red arrow-head lines denote observed (solid lines) and inferred (dashed lines) negative and positive shifts through the late stage and the termination of the LJIE.

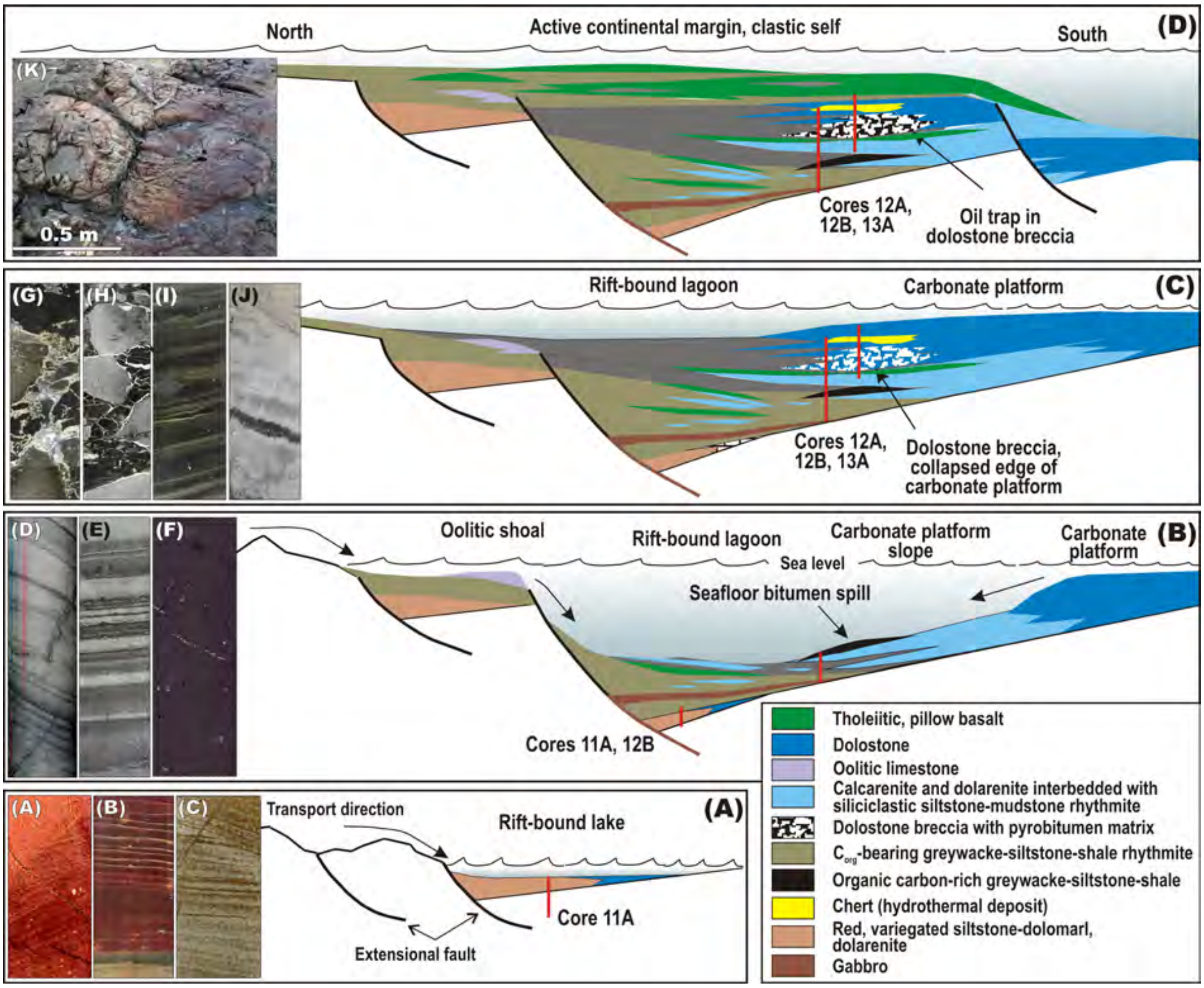

Fig. 26. A model illustrating evolving depositional settings of the ZF and depositional environments of carbonates. Red bars indicate approximate positions of FAR-DEEP holes with respect to evolving depositional environments. Note that the carbonate deposition began in a rift-bound lacustrine system (Panel A). The main stage of the carbonate deposition has been gradually switched from shedding (Panel B) to *in situ* accumulation (Panel C) due to progradation of an inferred carbonate platform. *In situ* brecciation of dolostones (Panel C) might have been caused by either collapse of the edge of a carbonate platform or due to seismic activity induced by extraterrestrial impact (Huber et al., 2014). Panel D illustrates the phase of drowned carbonate platform followed by its burial beneath a thick pile of sub-aqueously extruded basalts.

Rock images based on FAR-DEEP core; core diameter is 5 cm unless specified otherwise. (A) Cross-bedded sandstone whose primary grey-green colour was overprinted by secondary oxidation; Core 11A, depth 102.5 m. (B) Variegated, rhythmically bedded, lacustrine greywacke; Core 11A, depth 91.5 m. (C) Bedded dolomarl overlain by cross-bedded greywacke; scanned, 2-cm-wide, thin section, Core 11A, depth 54.39m. (D) Impure calcitic rock (pale grey) alternating with thin, dark grey mudstone units; Core 12B, depth 400 m. (E) Interbedded greywacke, black, C_{org}-rich mudstone and calcareous greywacke commonly associated with mafic lava flows; Core 12B, depth 375.6 m. (F) Massive, pyrobitumen-rich rock (seafloor spill) containing soft-sediment deformed fragments of pyrobitumen and partially disintegrated, non-lithified siltstone-sandstone clasts; Core 12B, depth 151 m. (G) Peperite composed of dismembered mafic lava flow and black mudstone; Core 13A, depth 93 m. (H) *In situ* brecciated massive dolostone cemented by pyrobitumen (fossil oil trap); Core 13A, depth 71.1 m. (I) Dark-coloured, laminated, C_{org}-rich mudstone with a small, lensoidal, chert nodule in the middle; Core 12A, depth 22.5 m. (J) Indistinctly bedded dolostone with dark grey, silicified interval; Core 13A, depth 19.2 m. (K) Photograph of pillow lava flow overlying the ZF.